

Spring 1-1-2015

Control of Transitional and Turbulent Flows Using Direct Numerical Simulation

Alec Kucala

University of Colorado Boulder, amk227@gmail.com

Follow this and additional works at: https://scholar.colorado.edu/asen_gradetds

 Part of the [Aerodynamics and Fluid Mechanics Commons](#)

Recommended Citation

Kucala, Alec, "Control of Transitional and Turbulent Flows Using Direct Numerical Simulation" (2015). *Aerospace Engineering Sciences Graduate Theses & Dissertations*. 107.

https://scholar.colorado.edu/asen_gradetds/107

This Dissertation is brought to you for free and open access by Aerospace Engineering Sciences at CU Scholar. It has been accepted for inclusion in Aerospace Engineering Sciences Graduate Theses & Dissertations by an authorized administrator of CU Scholar. For more information, please contact cuscholaradmin@colorado.edu.

**Control of Transitional and Turbulent Flows Using Direct
Numerical Simulation**

by

Alec Kucala

B.S. Northern Arizona University, 2010

A thesis submitted to the
Faculty of the Graduate School of the
University of Colorado in partial fulfillment
of the requirements for the degree of
Doctor of Philosophy
Department of Aerospace Engineering Sciences
2015

This thesis entitled:
Control of Transitional and Turbulent Flows Using Direct Numerical Simulation
written by Alec Kucala
has been approved for the Department of Aerospace Engineering Sciences

Professor Sedat Biringen (Chair)

Professor Mahmoud Hussein (Co-Chair)

Date _____

The final copy of this thesis has been examined by the signatories, and we find that both the content and the form meet acceptable presentation standards of scholarly work in the above mentioned discipline.

Kucala, Alec (Ph.D., Aerospace Engineering Sciences)

Control of Transitional and Turbulent Flows Using Direct Numerical Simulation

Thesis directed by Professor Sedat Biringen (Chair)

Efficient methods of drag reduction in wall-bounded shear flows remains an important, yet elusive problem in fluid mechanics. There are two potential avenues for drag reduction. One involves the delay of laminar-to-turbulent transition in the boundary layer, where in general the skin friction drag is lower for laminar flows. The other involves reducing the skin friction in a fully-developed turbulent flow, where finding an efficient method of transition delay remains a challenging problem. Steady/unsteady disturbances in the freestream such as sound or vorticity are introduced into the boundary layer through receptive processes and are catalysts for transition, whereby these disturbances provide the initial conditions of disturbance amplitude, frequency and phase for the breakdown of laminar flow. In low disturbance environments (such as cruise-flight conditions), the 2D Tollmien-Schlichting (TS) wave may amplify in the boundary layer and cause the flow to transition. Attempts have been made for laminar flow control using suction/blowing slots, wall heating and cooling, Lorentz forcing, passive compliant surfaces, or prescribed wall movement among others.

In the present computational study, we first utilize a suction/blowing slot to delay transition in a channel flow with three-dimensional instabilities, where the phase and amplitude of the slot is tuned in a specific way such that a substantial reduction in the amplitude of the primary TS wave is achieved. Problems involving transition delay in channel flows using passive *phononic subsurfaces* are then presented, where the elastodynamic response of the subsurface is precisely tuned to control the phase relationship between the pressure and velocity at the fluid/structure interface in such a way to attenuate the growth of perturbation energy in the fluid. To do this, the three-dimensional, time dependent, non-linear Navier-Stokes equation is coupled to a linear elastodynamics model using direct numerical simulation. We demonstrate the effectiveness of the

concept of a phononic subsurface to control primary (TS) instability in channel flows, flows with multiple excitation frequencies, and flows containing high-amplitude, weakly non-linear secondary instabilities.

Bursting events responsible for the production of a majority of the turbulent kinetic energy in turbulent flows are detected in both periodic and spatial turbulent channel flows using a second quadrant technique. Flow visualization is also carried out utilizing the method of Lagrangian Coherent Structures (LCS) to identify the flow structures associated with the production of turbulent kinetic energy. Measurements of the bursting period, time between bursts, and the convection velocity of the structures associated with the bursts are made, whereby excellent correlation is found between the LCS visualizations and burst detection techniques employed in this study. From this, an estimation of the bursting frequency is made which can be utilized in the design of a phononic subsurface to alter this bursting mechanism in such a way to lower the production of turbulent energy in wall-bounded flows, thus potentially re-laminarizing the flow field near the wall and reducing skin friction.

Acknowledgements

First, I would like to thank my advisor, Professor Sedat Biringen for providing his constant support of my graduate studies in the five years I have worked under him. His vast experience in a wide variety of disciplines related to fluid dynamics allowed us to explore countless avenues for solving the difficult problems that lie within this thesis. Without his support and guidance, this work would not have been completed. I would like to thank my co-advisor Professor Mahmoud Hussein as his expert knowledge in the field of phononics made this work possible. In addition, I would like to thank Dr. Osama Bilal for his collaboration on this project.

Finally, I would like to thank my loving wife, Mallory, who dropped everything to move here to Colorado with me in pursuit of my doctorate. Without her emotional support, I probably would not have made it all the way through the program. In addition, my dog, aptly named Newton, has been a constant source of happiness for me, as he was always happy to see me no matter what the circumstances. Also, I would like to thank the countless, wonderful people I have met while in this program for giving me something else to do but work!

Contents

Chapter

| | | |
|----------|--|----|
| 1 | Introduction and Motivation | 1 |
| 1.1 | Transition in Wall-Bounded Flow | 3 |
| 1.1.1 | Receptivity Mechanisms | 3 |
| 1.1.2 | Primary and Secondary Instability | 5 |
| 1.1.3 | Active Laminar Flow Control | 7 |
| 1.1.4 | Compliant Coatings for Laminar Flow Control | 8 |
| 1.2 | Turbulent Drag | 13 |
| 1.2.1 | Coherent Turbulent Structures | 13 |
| 1.2.2 | Active and Passive Control Strategies in Turbulent Flows | 14 |
| 1.2.3 | Turbulent Drag Reduction Using Compliant Surfaces | 16 |
| 1.3 | Phononic Crystals | 17 |
| 1.4 | Thesis Outline | 20 |
| 2 | Governing Equations | 22 |
| 2.1 | Fluid Domain | 22 |
| 2.1.1 | Equations of Motion | 22 |
| 2.1.2 | Spatial Simulation of Channel Flows | 23 |
| 2.1.3 | Turbulent Channel Flows | 24 |
| 2.2 | Equations for Phononic Crystals | 26 |

| | | |
|----------|---|-----------|
| 2.2.1 | Problem 1: Phononic subsurface unit-cell dispersion model | 26 |
| 2.2.2 | Problem 2: Phononic subsurface 10-unit-cell structural dynamics model . . . | 26 |
| 2.2.3 | Problems 3 and 4: Phononic subsurface 10-unit-cell wave propagation model | 27 |
| 2.3 | Fluid/Phononic Structure Interaction | 27 |
| 3 | Numerical Methods | 29 |
| 3.1 | Fluid Domain | 29 |
| 3.1.1 | Time Integration Scheme | 29 |
| 3.1.2 | Solve for Fractional Velocity and Temperature | 30 |
| 3.1.3 | Solve for Pseudo-Pressure/Updating Velocity | 31 |
| 3.1.4 | Spatial Differences | 32 |
| 3.1.5 | Parallel Architecture | 32 |
| 3.1.6 | Buffer Domain Technique | 36 |
| 3.1.7 | Pressure Correction | 37 |
| 3.1.8 | Validation | 37 |
| 3.2 | Numerical Methods for Phononic Structures | 38 |
| 4 | Control of Channel Flows in Transition | 41 |
| 4.1 | Spatial Simulation of Channel Flow Instability and Control | 43 |
| 4.1.1 | Introduction | 43 |
| 4.1.2 | Numerical Method | 45 |
| 4.1.3 | Modal Evolution of Secondary Instability | 48 |
| 4.1.4 | Flow visualization using Lagrangian Coherent Structures | 52 |
| 4.1.5 | Active Control of Transition | 57 |
| 4.1.6 | Conclusions | 63 |
| 4.1.7 | Acknowledgements | 64 |
| 4.2 | Control of Primary Instability Using a Phononic Subsurface | 65 |
| 4.2.1 | Introduction | 65 |

| | | |
|----------|--|------------|
| 4.2.2 | Methodology | 66 |
| 4.2.3 | Effect of the Subsurface on TS Waves | 70 |
| 4.2.4 | Phononic Subsurface Energetics | 77 |
| 4.2.5 | Summary and Conclusions | 80 |
| 4.2.6 | Acknowledgements | 81 |
| 4.3 | Phononic Subsurfaces for Multi-Frequency Instability Control | 82 |
| 4.3.1 | Introduction | 82 |
| 4.3.2 | Methodology | 83 |
| 4.3.3 | Case Descriptions | 83 |
| 4.3.4 | Results and Discussion | 88 |
| 4.3.5 | Summary and Conclusions | 97 |
| 4.4 | Control of K-type Instability Using Phononic Subsurfaces | 99 |
| 4.4.1 | Introduction | 99 |
| 4.4.2 | Case Descriptions and Subsurface Design | 100 |
| 4.4.3 | Results | 103 |
| 4.4.4 | Summary and Conclusions | 108 |
| 5 | Bursting Frequency in a Turbulent Channel Flow | 110 |
| 5.1 | Introduction | 110 |
| 5.2 | Case Descriptions | 112 |
| 5.2.1 | Periodic Channel | 112 |
| 5.2.2 | Spatial Channel | 117 |
| 5.3 | Results and Discussion | 119 |
| 5.3.1 | Identification of Bursts in the Periodic Channel | 120 |
| 5.3.2 | Identification of Bursts in the Spatial Channel | 122 |
| 5.3.3 | Visualization of turbulent flow structures using LCS | 125 |
| 5.4 | Summary and Conclusions | 131 |

| | | |
|----------|--|------------|
| 6 | Conclusions and Recommendations | 133 |
| 6.1 | Overview | 133 |
| 6.2 | Contributions | 135 |
| 6.3 | Recommendations | 136 |
| | Bibliography | 139 |

Tables

Table

| | | |
|-----|---|-----|
| 4.1 | Computational parameters for $Re = 10,000$, $\omega_r = 0.22$ | 48 |
| 4.2 | Summary of control cases for $Re = 10,000$ | 62 |
| 4.3 | Summary of $(\Delta K_f)_{\max}$, $\Delta\omega^*$ and $\frac{\psi(\omega_{TS})_{\eta(0)}}{\psi(\omega_{Truncation})_{\eta(0)}}$ for cases B-D | 79 |
| 4.4 | Selected unstable frequencies for $Re = 7,500$ | 83 |
| 4.5 | Case summary | 87 |
| 4.6 | Maximum modal energy differences $\Delta E_{\%}^*$ for various cases | 91 |
| 4.7 | Summary of maximum kinetic energy reductions $\Delta K_{f\%}$ for all cases | 95 |
| 4.8 | Computational parameters for K-type instability | 100 |
| 5.1 | Case summary | 112 |

Figures

Figure

| | | |
|------|--|----|
| 1.1 | Skin friction drag for laminar and turbulent flows (Gad-el Hak et al., 1998) | 2 |
| 1.2 | The paths of receptivity (Saric et al., 2002) | 4 |
| 1.3 | Typical stability curve for a Blasius boundary layer (Schlichting, 1968) | 6 |
| 1.4 | Effect of suction/blowing on the streamwise growth of u' velocity (Danabasoglu et al., 1991). | 9 |
| 1.5 | Compliant surface based and volume based models (Gad-el Hak, 2002) | 10 |
| 1.6 | Classification of fluid/solid waves (Gad-el Hak, 2002) | 12 |
| 1.7 | Characteristic u' velocity streaks in an $(x - z)$ plane of near-wall turbulence ($y/\delta = 0.08$). High speed and low speed fluid is denoted by red and blue contours, respectively (Hsieh, Biringen, Kucala, and Waggy, 2014). | 14 |
| 1.8 | The phononic spectrum (Maldovan, 2013) | 18 |
| 1.9 | Typical dispersion curves for a 1D phononic crystal (Hussein, Hulbert, and Scott, 2007). Solid lines represent pass bands (real wavenumber) and dashed lines represent stop bands (imaginary wavenumber) | 18 |
| 1.10 | Optimized phononic crystals to maximize band gaps adapted from Bilal and Hussein (2011). Images on the left represent the phononic crystal unit cell, with their respective dispersion curves on the right. | 19 |
| 2.1 | CSS: the conventional serial staggered procedure (Farhat and Lesoinne, 2000) | 28 |

| | | |
|-----|---|----|
| 3.1 | Strong scaling for doubly-periodic code: $Re = 1,000$, $512 \times 512 \times 256$, neutrally stratified Ekman Layer. Timing averaged over 200 iterations; startup effects are ignored. Dashed line, theoretical strong scaling; solid line / circles, DNS results. | 33 |
| 3.2 | Strong scaling for streamwise-spatial code: $Re = 10,000$, $450 \times 16 \times 65$, Channel flow in transition. Timing averaged over 200 iterations; startup effects are ignored. Dashed line, theoretical strong scaling; solid line / circles, DNS results. | 34 |
| 3.3 | Computational Effort for Case B: $Re = 1000$, $512 \times 512 \times 256$, unstably stratified. Results averaged over $300 \leq N_{procs} \leq 9600$ | 34 |
| 3.4 | Example solution of pseudo-pressure (ϕ) using GMRES algorithm for the periodic code. Solid line, DNS results; dashed line, $\log_{10}(r_i/r_{i-1}) = -2$. Residual normalized by initial residual | 35 |
| 3.5 | Spatial evolution of the (1,0) (solid line) and (1,1) (dashed line) modes for the two-dimensional and three-dimensional disturbances, respectively. \circ : two-dimensional linear theory, \square : three-dimensional linear theory. | 38 |
| 4.1 | Flow geometry and coordinate system for present channel-flow simulation. | 46 |
| 4.2 | Spectrum of vertically averaged kinetic energy at $x = 55.80$ for case (a) L-A, (b) H-A; \circ : $\omega = 0.5$ (subharmonic), \diamond : $\omega = 1$ (fundamental). | 49 |
| 4.3 | Streamwise evolution of vertically averaged kinetic energy for specific modes for (a) case L-A, \circ : (1,0), \diamond : (0.5,1), \times : (0.5,2.5), \square : (1,1), $+$: (1,2.5) | 50 |
| 4.4 | Growth rate σ of the subharmonic mode as a function of the spanwise wavenumber β measured at the end of the channel | 50 |
| 4.5 | 2D forward FTLE fields in the critical layer $y \approx 1.88$ for the H-A case at (a) $T = 225.3$ (b) $T = 270.6$ for an integration time of $\tau = 0.357$ | 54 |
| 4.6 | 2D forward FTLE fields at $z \approx 3.1$ for the H-A case at (a) $T = 248.1$ (b) $T = 253.8$ (c) $T = 262.4$ (d) $T = 272.4$ for an integration time of $\tau = 0.357$ | 55 |

- 4.7 3D forward FTLE fields in the y - z plane at $T = 272.4$ for the H-A case at (a) $x \approx 47.3$ (b) $x \approx 50.6$ (c) $x \approx 53.85$ (d) $x \approx 57.1$ for an integration time of $\tau = 0.357$ 56
- 4.8 Streamwise evolution of integrated kinetic energy for specific modes for (a) case L-A, $\circ : (1, 0)$, $\diamond : (0.5, 1)$, $\times : (0.5, 2.5)$, $\square : (1, 1)$, $+$: $(1, 2.5)$, (b) case H-A, $\circ : (1, 0)$, $\diamond : (0.5, 1.5)$, $\times : (0.5, 4)$, $\square : (1, 1.5)$, $+$: $(1, 4)$. Solid lines represent fundamental modes while dashed lines represent subharmonic modes. 57
- 4.9 Wall-normal control signal measured at the suction/blowing slot and the wall pressure signal measured at $x = 18.77$ over two full TS periods for (a) L-A case, (b) H-A case; solid line: wall pressure signal, dashed line: suction/blowing control signal. . . 59
- 4.10 $\langle \overline{u'v'} \rangle$ distributions for (a) Case L-A and (b) Case H-A; solid line: no control, dashed line: with control. 60
- 4.11 Case L-A streamwise evolution of (a) $\langle u'_{RMS} \rangle$ (b) $\langle v'_{RMS} \rangle$; solid line: no control, dashed line: with control. 61
- 4.12 Case H-A streamwise evolution of (a) $\langle u'_{RMS} \rangle$ (b) $\langle v'_{RMS} \rangle$; solid line: no control, dashed line: with control. 61
- 4.13 (a) Schematic of plane flow channel with phononic subsurface covering a segment in the range $x_s \leq x \leq x_e$, where $x_s = 2.926 \times 10^{-3}$ m and $x_e = 3.602 \times 10^{-3}$ m. For comparison, replacement with a rigid wall or other materials are also considered. (b) Dispersion curves for the 1D phononic crystal from which the subsurface is composed [Brillouin zone (Brillouin, 1946) illustrated in inset]. (c) Steady-state vibration response of phononic crystal top surface. (d) Time-averaged phase between force and displacement at the phononic crystal top surface. (e) Performance metric combining amplitude and relative phase between the force and the displacement at the phononic crystal top surface. Results from the coupled fluid-structure simulations are represented by red dots. In the coupled simulations, the phononic crystal top surface serves as the fluid-structure interface. 69

- 4.14 Time history of the kinetic energy of the disturbance field within the bottom half of the channel for (a) Case B ($\omega_{\text{TS}} = 1690$ Hz in a stop band) and (b) Case A ($\omega_{\text{TS}} = 1600$ Hz in a pass band). (c) Relative phase between flow vertical velocity at $(x, y, z) = ([x_s + x_e]/2, 0.0108\delta, z)$ when a phononic subsurface is installed compared to all-rigid walls (Rigid). Each velocity quantity is normalized with respect to its maximum value. 72
- 4.15 Streamwise spatial distribution of the time-averaged kinetic energy of the disturbance field within the bottom half of the channel for (a) Case B ($\omega_{\text{TS}} = 1690$ Hz in a stop band) and (b) Case A ($\omega_{\text{TS}} = 1600$ Hz in a pass band). The plotted quantity represents the spatial intensity of the flow instability. 73
- 4.16 Decomposition of the perturbation energy flux in the fluid based on terms in Eq. 4.16. 74
- 4.17 Perturbation energy production rate in the fluid for (a) Case B ($\omega_{\text{TS}} = 1690$ Hz in a stop band) and (b) Case A ($\omega_{\text{TS}} = 1600$ Hz in a pass band). 76
- 4.18 Maximum displacement $\eta(0)_{\text{max}}$ for Case B relative to the maximum allowable surface roughness k on the wall-normal (y) grid. Circles represent the discrete grid points in y 76
- 4.19 Average quantities of the total elastodynamic energy in the phononic subsurface for Case B ($\omega_{\text{TS}} = 1690$ Hz in a stop band) and Case A ($\omega_{\text{TS}} = 1600$ Hz in a pass band). The space-averaged total energy, $\{\Psi(\omega^*; s, t)\}$, is shown in (a) for Case B and in (b) for Case A. The time-averaged total energy, $\langle\Psi(\omega^*; s, t)\rangle$, is shown in (c) for Case B and in (d) for Case A. Information on how these average quantities are computed is provided in Appendix A. The energy inside the phononic subsurface displays a beat frequency of approximately 7 Hz. The unit cells are marked by vertical lines. 77
- 4.20 The effect of damping on flow energy T_f and power spectra of interface wall displacements $\psi_{\eta(0)}$ of Case B for (a) Undamped case ($q = 0$) and (b) Damped case ($q = 6 \times 10^{-8}$) 79

- 4.21 Predicted and actual performance metric (left ordinate) and actual change in flow disturbance kinetic energy (right ordinate) for Cases A-D. Grey region covers band gap of phononic-subsurface unit cell. Schematics above the chart refer to the computational domain considered for obtaining each quantity. A performance summary is provided in the inset. 81
- 4.22 Phononic subsurface design A; (a) Dispersion curves for the 1D phononic crystal from which the subsurface is composed (material arrangements of the 1D periodic lattice is detailed on the inset). (b) Steady-state vibration response of phononic crystal top surface. (c) Time-averaged phase between force and displacement at the phononic crystal top surface. (d) Performance metric combining amplitude and relative phase between the force and the displacement at the phononic crystal top surface. Legend for dots is as follows: Red - 1487 Hz; Blue - 1690 Hz; Magenta - 1892 Hz 85
- 4.23 Phononic subsurface design B; (a) Dispersion curves for the 1D phononic crystal from which the subsurface is composed ((material arrangements of the 1D periodic lattice is detailed on the inset). (b) Steady-state vibration response of phononic crystal top surface. (c) Time-averaged phase between force and displacement at the phononic crystal top surface. (d) Performance metric combining amplitude and relative phase between the force and the displacement at the phononic crystal top surface. Legend for dots is as follows: Red - 1487 Hz; Blue - 1690 Hz; Magenta - 1892 Hz 86
- 4.24 Vertically averaged kinetic energy spectra in the fluid for (a) Case A; (b) Case B. Dashed lines represent a rigid wall case where solid lines represent the control case. Vertically dashed lines indicate the upstream and downstream boundaries of the phononic subsurface. 89
- 4.25 Vertically averaged kinetic energy spectra in the fluid for multiple subsurfaces (a) Case A-A; (b) Case B-B; (c) Case A-B. Dashed lines represent a rigid wall case where solid lines represent the control case. Vertically dashed lines indicate the upstream and downstream boundaries of the phononic subsurface. 90

| | |
|--|-----|
| 4.26 Spectra of phononic subsurface displacement at fluid/structure interface $\eta(0)$ for (a) Design A; (b) Design B. | 92 |
| 4.27 Time averaged perturbation kinetic energy in the fluid. Dashed lines indicate control using two phononic subsurfaces. Vertically dashed lines indicate the upstream and downstream boundaries of the phononic subsurface. | 94 |
| 4.28 Instantaneous contours of streamwise perturbation velocity \hat{u} in the half-channel for (a) Rigid wall; (b) Case A-A; (c) Case B-B; (d) Case A-B. Gray strip indicates the control area. | 96 |
| 4.29 Phononic subsurface design to control 3D disturbances; (a) Dispersion curves for the 1D phononic crystal from which the subsurface is composed (material arrangements of the 1D periodic lattice is detailed on the inset). (b) Steady-state vibration response of phononic crystal top surface. (c) Time-averaged phase between force and displacement at the phononic crystal top surface. (d) Performance metric combining amplitude and relative phase between the force and the displacement at the phononic crystal top surface. Red dot indicates location of primary mode (1690,0); Magenta dot indicates location of first harmonic (3380,0) | 102 |
| 4.30 Surface of $S_f^{*c} - S_f^{*nc}$ as a function of time t^* and spanwise position z^* | 104 |
| 4.31 Mean perturbation kinetic energy in the fluid K_f^* as a function of streamwise position x^* . Dashed vertical lines indicate upstream and downstream boundaries of the subsurface surface | 105 |
| 4.32 Rigid wall and control case comparisons of (a) Volume integrated PKE T^*f ; (b) Perturbation velocity correlations $\hat{u}^* \cdot \hat{v}^*$ at $x = 22.4\delta$, $y = 0.177\delta$, $z = 1.396\delta$ | 106 |
| 4.33 Streamwise evolution of modal energy E^* for (a) Primary TS mode (1690,0); (b) Harmonic of TS mode (3380,0); (c) Fundamental K-type mode (1690,1). | 108 |
| 5.1 Mean velocity U^+ in wall-units for Case P; the black dashed line represents the log law given in Eqs. 5.2-5.3. | 113 |

| | | |
|------|--|-----|
| 5.2 | Root-mean-squared distributions of u_{rms}^+ , v_{rms}^+ , w_{rms}^+ across the channel. | 114 |
| 5.3 | Shear stress distributions $\overline{u'v'}$ and total shear τ across the channel | 115 |
| 5.4 | Energy spectra of Case P for the streamwise E_{uu} , wall-normal E_{vv} , and spanwise E_{ww} velocity components at $y^+ = 21.2$; (a) Streamwise spectra, (b) Spanwise spectra | 116 |
| 5.5 | Crossflow plane of u at $x^* = 2\pi\delta$ and time $t^* = 2064 \delta/U_{cl}$ | 118 |
| 5.6 | Comparison of root-mean-squared distributions (normalized by u_τ) between Case P (solid lines) and Case S (dashed lines). | 119 |
| 5.7 | Comparison of shear stress distributions $\overline{u'v'}$ and total shear τ across the channel between Case P (solid lines) and Case S (dashed lines). | 120 |
| 5.8 | Energy spectra of Case S for the streamwise E_{uu} , wall-normal E_{vv} , and spanwise E_{ww} velocity components at $x^+ = 628$ and $y^+ = 21.2$ | 121 |
| 5.9 | Instantaneous burst plane for Case P at $t = 1864$ and $y^+ \approx 15$; black segments represent a bursting event satisfying Eq. 5.5. | 122 |
| 5.10 | Instantaneous burst plane for Case P at $t = 1864$ and $y^+ \approx 20$; black segments represent a bursting event satisfying Eq. 5.5. | 123 |
| 5.11 | Bursting period T_b^+ and time between bursts T_{bw}^+ as a function of detection location | 124 |
| 5.12 | Energy spectra of Case S for the streamwise E_{uu} , wall-normal E_{vv} , and spanwise E_{ww} velocity components at $x^+ = 628$ and $y^+ = 21.2$ superimposed with the range of bursting frequency T_b^+ reported in figure 5.11. | 126 |
| 5.13 | Time-sequence of instantaneous forward FTLE contours in the (x^+, y^+) plane at $z^+ = 311$ (a) $t^+ = 8000$; (b) $t^+ = 8010$; (c) $t^+ = 8020$; (d) $t^+ = 8030$ | 128 |
| 5.14 | Demonstration of LCS and bursting detection technique in the (x^+, y^+) plane at $z^+ = 311$ and $t^+ = 8000$ (a) forward FTLE contours; (b) second quadrant technique. | 129 |
| 5.15 | Forward FTLEs at $t^+ = 8000$ for (a) (x^+, z^+) plane at $y^+ = 21.2$; (b) (z^+, y^+) plane at $x^+ = 618$ | 130 |

Chapter 1

Introduction and Motivation

Control of transition and turbulence in wall-bounded flows (boundary layers and channel flows) remains an important problem in fluid mechanics. In general, boundary layer control includes any mechanism or process through which the boundary layer of fluid flow is caused to behave differently than it normally would were the flow developing naturally along a smooth straight surface (Gad-el Hak, Pollard, and Bonnet, 1998). Control goals may vary and include transition delay, separation postponement, lift increase, skin-friction reduction, pressure drag reduction, turbulence augmentation, heat transfer enhancement, or noise suppression (Gad-el Hak et al., 1998). The focus here is to lower the skin friction, and in turn the overall drag on a surface. The potential benefits of realizing efficient flow control systems range from saving billions of dollars in fuel cost for land, air, and sea vehicles to achieving more economically and environmentally competitive industrial processes involving fluid flows (Gad-el Hak and Tsai, 2006). Generally, drag reduction can be achieved in two ways:

- (1) Deny or delay the flow from transitioning and to remain laminar, where mean velocity gradients are generally lower.
- (2) Once turbulent, alter the flow in such a way to decrease the time-averaged mean velocity gradient, and therefore skin-friction.

Obviously these represent two distinct scenarios. In the first scenario, knowledge of the transition mechanisms taking place within the boundary layer is required in order to attempt to

deny or delay the flow from transitioning. Maintaining a laminar boundary layer would be most ideal and would have the most significant impact in terms of overall drag reduction (see figure 1.1). However, the transition picture is quite complicated and the path to transition is heavily dependent on the external catalysts responsible for introducing instabilities into the boundary layer, also known as receptivity (Reshotko, 1976, 1987), and the flow may bypass all of these transition scenarios if the freestream turbulence levels are large enough (Andersson, Berggren, and Henningson, 1999; Watmuff, Pook, Sayadi, and Wu, 2010).

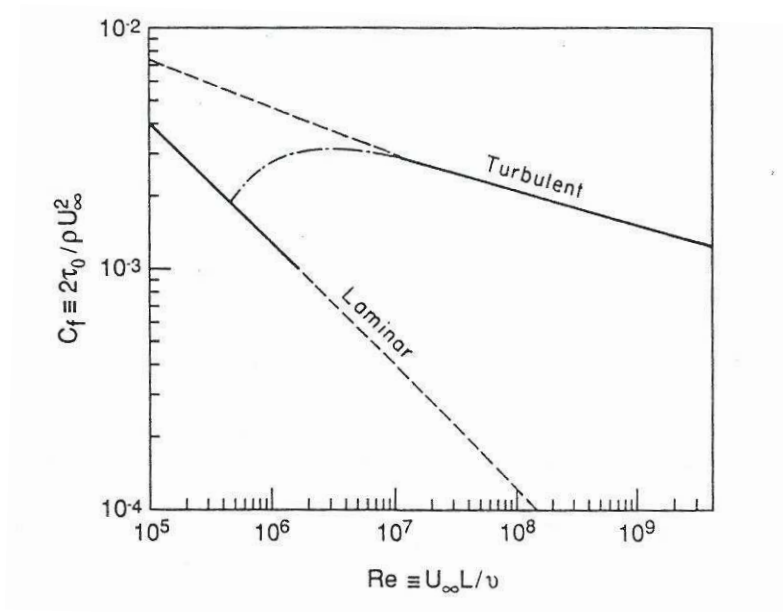


Figure 1.1: Skin friction drag for laminar and turbulent flows (Gad-el Hak et al., 1998)

While delaying laminar to turbulence transition would be ideal, it is generally accepted that for high Reynolds numbers ($Re > 4 \times 10^7$), transition to turbulence cannot be delayed with any known practical method without incurring a penalty that exceeds the saving (Gad-el Hak et al., 1998). Therefore, for high Reynolds number flows (say a commercial aircraft traveling at 300 m/s), the task is then to reduce the skin-friction in a turbulent boundary layer. Many methods exist in the literature to reduce the turbulent skin-friction, through active (Choi, Moin, and Kim, 1994; Du and Karniadakis, 2000; Bewley, Moin, and Teman, 2001; Chang, Collis, and Ramakrishnan, 2002)

and passive (Walsh and Lindemann, 1984; Lee and Jang, 2005) control strategies.

Control of both transition and turbulence is of vital importance, and remains an elusive problem in fluid mechanics. The benefits of drag reduction are obvious, however the methods employed need to both be efficient and effective. Unfortunately, many active control methods require an excessive amount of power which contributes to a loss in the efficiency of the control method. Passive control strategies require no power, and therefore operate with maximum efficiency, provided that they either successfully delay transition or reduce the turbulent skin friction. The use of compliant coatings (Kramer, 1960; Choi, Yang, Clayton, Glover, Atlar, Semenov, and Kulik, 1997; Davies and Carpenter, 1997; Xu, Rempfer, and Lumley, 2003) has been largely unsuccessful in this endeavor.

1.1 Transition in Wall-Bounded Flow

1.1.1 Receptivity Mechanisms

The transition from laminar to turbulent flow in wall-bounded shear layers is a vitally important topic in the field of fluid mechanics, especially in the context of flow control and drag reduction. Currently, no mathematical model exists that can accurately predict the point of transition on a flat plate, as there are a variety of influences such as freestream turbulence, surface roughness, sound waves, and entrainment (non-parallel effects). Steady/unsteady disturbances in the freestream such as sound or vorticity are the catalysts for transition and their influence on the basic state of the boundary layer is called receptivity (Morkovin, 1969). These disturbances provide the initial conditions of disturbance amplitude, frequency and phase for the breakdown of laminar flow (Saric, Reed, and Kerschen, 2002).

Figure 1.2 provides a simplified roadmap of the paths from receptivity to transition. When the amplitude of the freestream disturbances is weak, the nonlinear terms in the boundary layer disturbance equations can be neglected and the growth/decay of the disturbances can be predicted using the linear theory (White, 1974). These weakly growing/decaying disturbances are two-dimensional in nature and are described as Tollmien-Schlichting (TS) waves. As the amplitude of the two-

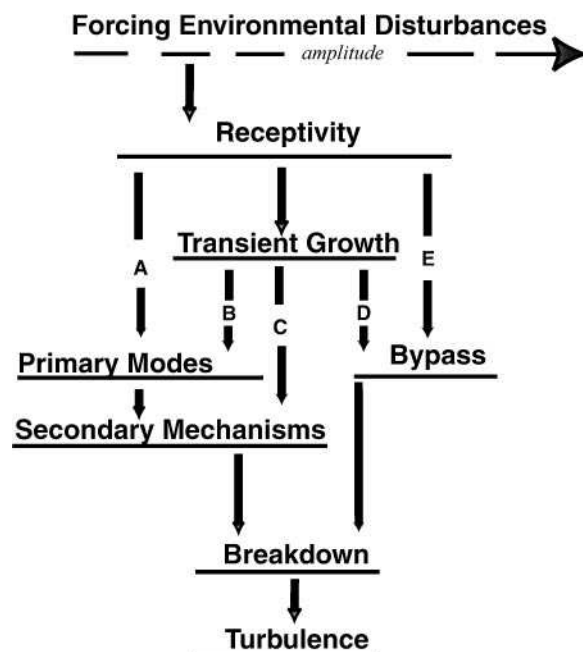


Figure 1.2: The paths of receptivity (Saric et al., 2002)

dimensional TS mode increases exponentially, nonlinear interactions begin to occur at some finite amplitude, which spurs the growth of the three-dimensional modes, known as secondary instability. In this stage of transition, disturbance growth is very rapid and breakdown to turbulence occurs in quick succession.

In general, receptivity concerns the generation of instability waves rather than their evolution. Boundary layers are convectively unstable, therefore an unsteady disturbance is required to generate instability waves, and may either be naturally occurring (freestream turbulence) or artificially forced (suction/blowing slot or vibrating ribbon) (Saric et al., 2002). In forced receptivity (Klebanoff et al., 1962; Kucala and Biringen, 2014), the input disturbance contains energy at the appropriate frequency-wavelength combination to directly excite an instability wave, and therefore streamwise gradients of the mean flow do not play an essential role (Kachanov, 2000).

For natural receptivity, two freestream forcing mechanisms exist, acoustical (irrotational) and vortical (rotational). These two mechanisms are distinguished by the phase speed of the

disturbances relative to the freestream. The acoustical disturbances travel at a phase speed equal to the speed of sound of the fluid, where the vortical disturbances travel at a phase speed relative to the freestream. The vortical parts of the freestream disturbances contribute to the three-dimensional aspects of the breakdown process (Kendall, 1998), where the acoustical freestream disturbances contribute to the initial amplitude of the TS waves (Kosorygin, H., and Saric, 1995).

1.1.2 Primary and Secondary Instability

The most understood path of transition is that of primary instability, which involves the growth of a two-dimensional, convective wave known as the Tollmien-Schlichting (TS) wave and is the primarily amplified wave when freestream disturbances are low, which is common in cruise flight conditions. These waves have characteristically low growth rates (in time or space) and are observed mostly in low disturbance environments (Klebanoff et al., 1962; Nishioka et al., 1975). The prediction of these linear instability waves can be made by splitting the flow field variables into a base flow (\mathbf{u}_b) and a fluctuating component ($\hat{\mathbf{u}}$) such that

$$\mathbf{u} = \mathbf{u}_b + \hat{\mathbf{u}} \quad (1.1)$$

Using this definition of velocity, and inserting it into Eq. 2.2 and assuming $\hat{\mathbf{u}} \ll \mathbf{1}$, we obtained a linearized version of the Navier-Stokes equations, also known as the Orr-Sommerfeld equation (White, 1974)

$$(u_b - c)(\hat{v}'' - \alpha^2 \hat{v}) - u_b'' \hat{v} + \frac{i}{\alpha Re}(\hat{v}'''' - 2\alpha^2 \hat{v}'' + \alpha^4 \hat{v}) = 0 \quad (1.2)$$

where ($'$) represents differentiation in the wall-normal direction, u_b represents the base flow, and Re is the Reynolds number. In addition, the complex wave-speed, $c = -\omega_r/\alpha$ and α represents the complex wavenumber and $i = \sqrt{-1}$. For spatially growing waves ($\alpha_i < 0$), as the waves propagate downstream, their amplitude increases linearly (on a logarithmic scale). By assuming a wave solution on \hat{v}

$$\hat{v}(x, y, t) = v(y)e^{i\alpha(x-ct)} \quad (1.3)$$

and homogenous boundary conditions on the wall $\hat{v}(x, y = 0, t) = \hat{v}'(x, y = 0, t) = 0$ and the far-field (for boundary layers) $\hat{v}(x, y \rightarrow \infty, t) = \hat{v}'(x, y \rightarrow \infty, t) = 0$ Eq. 1.2 can be solved as an eigenvalue problem, and stability curves may be generated as a function of Reynolds number, shown in figure 1.3.

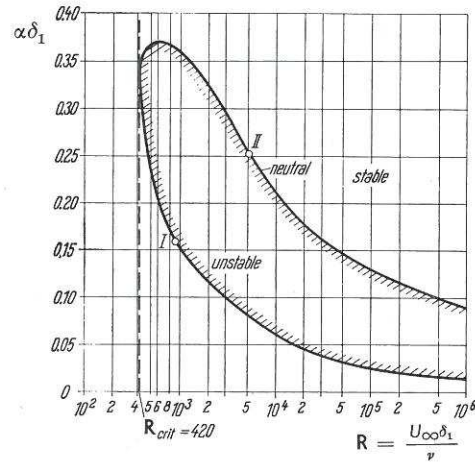


Figure 1.3: Typical stability curve for a Blasius boundary layer (Schlichting, 1968)

As these two dimensional waves propagate downstream and amplify, the amplitude becomes finite and nonlinear effects begin to occur and the disturbances become three-dimensional (Herbert, 1988). The three dimensionality manifests itself in the form of Λ vortices, and can either be staggered (H-type) or aligned (K-type) depending on the initial amplitude of the two-dimensional wave, although the exact scenarios for K-type or H-type development is still contested in the literature (Kim and Moser, 1989; Singer et al., 1989; Kucala and Biringen, 2014). At this stage, rapid growth in the three-dimensional modes occurs over relatively short distances, hairpin vortices begin to develop and finally breakdown to turbulence occurs (Klebanoff, Tidstrom, and Sargent, 1962).

Other paths of transition include inviscid instabilities, which occur due to an inflection in the mean velocity profile (White, 1974), bypass transition, Taylor-Gortler vortices owing to surface curvature effects (DiPrima and Swinney, 1985), and cross-flow instabilities occurring in three-dimensional velocity profiles (Saric, Reed, and White, 2003; Hosseini, Hanifi, and Henningson,

2013), among others. Obviously the scope of transition is quite broad in the context of viscous flows, and becomes even broader when we consider the external forcing and receptivity mechanisms responsible for introducing instabilities into boundary layers.

1.1.3 Active Laminar Flow Control

Over the years, there have been a number of attempts to maintain a laminar boundary layer. The most popular of which, demonstrated early in the boundary layer theory by Prandtl (1904), in which he used the method of constant suction on a cylinder in order to keep the flow attached preventing separation and maintaining laminar flow. By withdrawing small amounts of fluid from the near-wall region of the boundary layer, a change in the curvature of the velocity profile at the wall can dramatically alter the stability characteristics of the boundary layer. This also has an effect to inhibit the growth of the boundary layer, such that the Reynolds number based on thickness may never be reached (see figure 1.3) (Gad-el Hak et al., 1998). The drag coefficient in laminar flows over a flat plate, in general, is about an order of magnitude less than that of a turbulent flow.

This method of flow control has been used extensively, where the successful flight of the X-21 was achieved using a constant suction porous surface at the leading edge on a swept wing, where transition was delayed up to a chord Reynolds number of 4.7×10^7 (Gad-el Hak et al., 1998). However, this method has a few caveats. Generally, this method uses a lot of power, and in some cases the power input required to drive the suction actuators is actually higher than the power saved due to drag reduction, thereby mitigating the efficiency of this method. In addition, obstructions such as insects in flight or ocean particulates in marine applications can clog the porous suction slots/holes, leading to losses in efficiency.

As opposed to changing the stability properties of the flow via mean velocity profile modulation, such as in the case of constant suction, other active control strategies aim to mitigate the growth of an already unstable wave via wave cancellation. If the frequency, orientation, and phase angle of the dominant element of the spectrum of growing linear disturbances in the flow is detected,

a control system may be used to effect the desired wave cancellation or suppression of a detected disturbance (Gad-el Hak et al., 1998). Many studies concerning wave cancellation using active control have been carried out in the literature, where the use of a suction/blowing slot (Biringen, 1984; Danabasoglu et al., 1991; Erdmann et al., 2011; Kucala and Biringen, 2014), surface heating and cooling (Liepmann and Nosenchuck, 1982), plate vibration (Gedney, 1983), and even Lorentz forcing (Albrecht, Aetzkes, Grundmann, Mutschke, and Gerbeth, 2008) can all be used to alter or cancel the unstable modes, thereby delaying transition.

The use of suction/blowing slots have been used to delay both primary and secondary instability in spatially evolving channel flows (Danabasoglu et al., 1991; Kucala and Biringen, 2014) whereby the length, phase, and amplitude of the suction/blowing slot all have to be carefully tuned in order to obtain the desired effect of primary wave cancellation. Figure 1.4 demonstrates the ability of a suction/blowing slot to mitigate the the growth of the primary instability, where the amplitude of the unstable wave is greatly reduced. However, as the wave propagates downstream of the suction/blowing slot, linear growth begins again, owing to the fact that the mean velocity profile has not been modified, and the unstable wave will again grow albeit with a much smaller initial amplitude. Realizing active control strategies for wave cancellation purposes in a real application is not straightforward, however, and would require an extensive array of disturbance detectors and generators as well as prohibitively complicated control systems to cancel both primary and other residual disturbance spectra prevalent in a real flow (Reshotko, 1987).

1.1.4 Compliant Coatings for Laminar Flow Control

Active control strategies require complicated control schemes as well as power input to drive the actuators responsible for injecting and sucking fluid through the porous slot (or the analogous wall-motion) in order to alter the unstable waves present in the boundary layer. Often, this power input is high and thus negates the power saved due to drag reduction. Passive control strategies, instead, allow the stress field present in the fluid to generate the wall motion when the modulus of elasticity of the wall is sufficiently low. Theoretical studies of boundary-layer stability in the

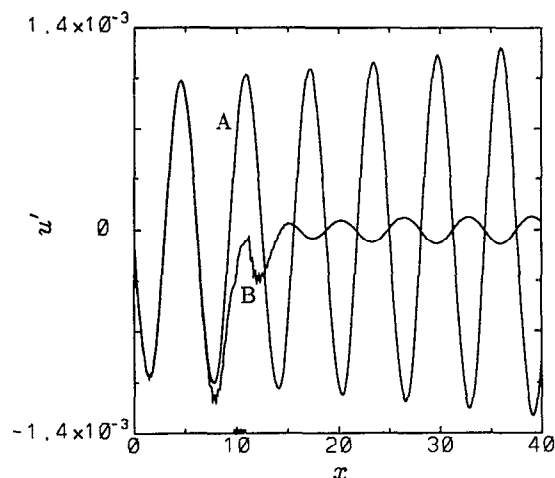


Figure 1.4: Effect of suction/blowing on the streamwise growth of u' velocity (Danabasoglu et al., 1991).

presence of a flexible wall started in the early 1960s (Benjamin, 1960, 1963; Landahl, 1962), inspired by the early work of Kramer (1960, 1962), where he demonstrated turbulent drag reduction when replacing a portion of a rigid wall with a flexible membrane modeled after dolphin skin. However, subsequent experiments were unable to confirm Kramer's findings and, for a time, compliant coatings for flow control purposes were practically abandoned. However, in the 1980's, the work of Carpenter and Garrad (1985, 1986) and subsequent experiments (Lucey and Carpenter, 1995) was able to show that, at least in principle, compliant coatings can be used to inhibit the growth of unstable TS waves, and effectively increases the minimum critical Reynolds number for primary instability.

The theory of compliant coatings for laminar flow control was developed by coupling the linearized Navier-Stokes (Orr-Sommerfeld) equations with an appropriate structural model, ensuring continuity of stress/pressure and velocity at the interface boundary. Many types of compliant surfaces exist, therefore there are many equations to describe their motions. Illustrations of the various models used in the literature is found in figure 1.5. The most popular model, a surface based Kramer type surface-based model, has been used extensively in the literature (Landahl, 1962;

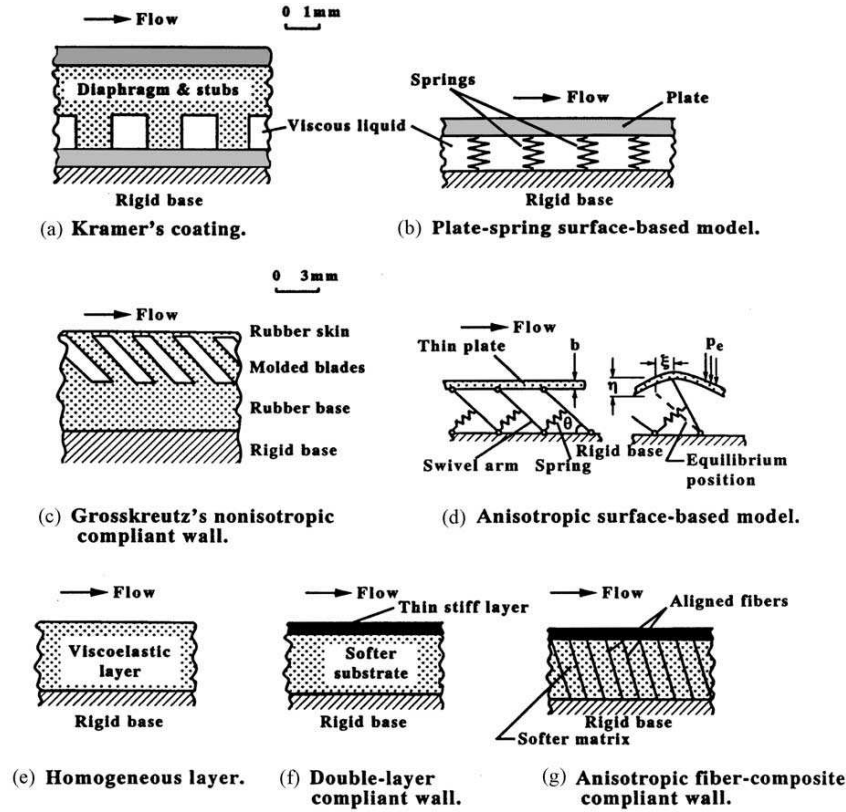


Figure 1.5: Compliant surface based and volume based models (Gad-el Hak, 2002)

Carpenter and Garrad, 1985; Davies and Carpenter, 1997). These models are known as surface based models, where the structural displacement is orthogonal to the direction of wave propagation, an example of which is shown in Eq. 1.4.

$$\frac{\partial^2 \eta}{\partial t^2} = \frac{T_l}{m} \frac{\partial^2 \eta}{\partial x^2} - D \frac{\partial \eta}{\partial t} - \frac{\mathcal{F}}{m} \frac{\partial^4 \eta}{\partial x^4} - \frac{k}{m} \eta + F \quad (1.4)$$

where $\eta(x, t)$ is the wall-normal displacement of the surface from its equilibrium state as a function of the streamwise position (x) and time (t), T_l is the longitudinal tension, m is the mass per unit area, D is the damping coefficient, k is the spring constant, and F is the external forcing term (Gad-el Hak, 2002).

Coupling of this structure with one or both walls of fluid equations is obtained through the

use of a wall-admittance term (Landahl, 1962; Carpenter and Garrad, 1985)

$$Y_0 = Y_1 = -\frac{\text{normal wall velocity}}{\text{wall pressure}} \quad (1.5)$$

where Y_0 and Y_1 are the admittances of the boundary layer fluid and the flexible surface, and expressions for these terms can be derived from the equations of motion for the fluid and solid, respectively. This matching of admittance terms acts to couple the stresses and velocities between the fluid and solid domains, giving a homogenous boundary condition at the interface and therefore an eigenvalue problem can be solved for the coupled fluid/structure domain (Carpenter and Garrad, 1985, 1986).

In the literature, there are three classification schemes for the fluid/structure waves (Landahl, 1962; Benjamin, 1963; Carpenter and Garrad, 1985). Class **A** waves are stabilized by the irreversible energy transfer from the fluid to the wall but are destabilized by dissipation in the wall. Also, the eigenfunctions for these waves have a maximum within the fluid domain. TS waves are class **A** waves. Class **B** waves, alternatively, are stabilized by dissipation in the wall and are destabilized by the transfer of energy from the fluid to the wall. Due to the fact that these waves occur at the fluid/solid interface (for surface-based models), the maxima of their disturbance eigenfunctions are also located there. Class **B** waves are generally wall-based modes and are often termed flow-induced surface instabilities (FISI) by Carpenter and Garrad (1986) and can lead to instability in the fluid/solid system. Essentially, class **B** waves are amplified when the flow supplies sufficient energy to counterbalance the coating's internal dissipation (Gad-el Hak, 2002). Both class **A** and **B** waves are convective instabilities.

Class **C** waves are an inviscid instability mechanism, and is a conservative mechanism in the fluid/solid system. Class **C** waves are classified in two ways (see figure 1.6). The first is through a coalescence with the traveling TS wave, whereby the convective velocity of this wave is large enough (due to high freestream velocities) to turn originally upstream traveling waves in the solid downstream, forming a powerful new instability termed the transitional mode by Sen and Arora (1988). The second classification is related, except now the group velocity of the traveling wave is

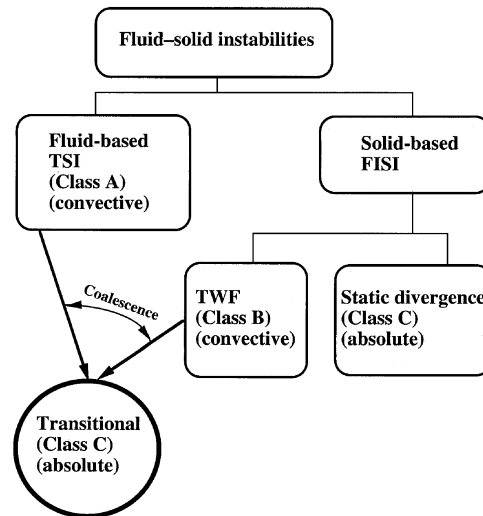


Figure 1.6: Classification of fluid/solid waves (Gad-el Hak, 2002)

near zero and is referred to as an absolute instability. That is, at all points on the wall the wall displacement is growing in time. This is often referred to as static divergence.

The one issue in using compliant surfaces for laminar flow control, despite successful numerical (Davies and Carpenter, 1997) and physical (Lucey and Carpenter, 1995) experiments is the amplification of the class **B** and class **C** waves when only a damping of the TS waves (class **A**) is desired. More importantly, there is a lack of consistent conclusive evidence for the success of compliant coatings in stabilizing TS waves. Class **(C)** waves are the most dangerous, and are unavoidable at high freestream speeds found in a typical airfoil in cruise-flight. In addition, the use of these compliant surfaces was deemed limited to applications in marine environments due to the excessive flexibility of the panels required for applications in air (Carpenter, Lucey, and Davies, 2001). This conclusion severely limits the applicability of compliant surfaces for flow control in aeronautical applications.

1.2 Turbulent Drag

Drag on a surface is usually classified in two ways; skin friction and pressure drag. The former includes the tangential shear stress, where the mean velocity gradient at the wall is responsible for this component of drag. Skin friction drag is much higher for turbulent flows than for laminar flows, owing to the steeper mean flow gradients near the wall. Pressure drag is a function of flow separation, displacement effects of the boundary layer, and drag induced by lift on a finite body. In marine applications, about 90% of the total drag is due to skin friction (Gad-el Hak et al., 1998). The present focus is on both the mechanisms of skin friction drag in turbulent flows, and strategies to reduce the skin friction drag using active and passive control strategies.

1.2.1 Coherent Turbulent Structures

In general, there are three types of quasi-periodic eddies: the large, outer structures that scale on the outer flow variables (Kovaszny, Kibens, and Blackwelder, 1970); intermediate Falco eddies (Falco, 1974), and near-wall eddies where almost all of the production of turbulence kinetic energy takes place. It is in this near-wall region that is of importance, where the interaction between high and low speed fluid through spanwise coherent streamwise vortices (Blackwelder, 1978; Kim, 2011) produces almost all of the turbulent kinetic energy. These streamwise vortices, in general, have a spanwise wavelength $\lambda_z \approx 100\nu/u_\tau$ where ν is the kinematic viscosity and $u_\tau = \sqrt{\tau_w/\rho}$ is the friction velocity.

In fully developed turbulent wall-bounded flows, turbulence generation follows a very intricate scenario that consists of a sequence of “ejection” and “sweep” events (Kim, Moin, and Moser, 1987) during which slow moving fluid in the wall region is ejected towards the outer regions of the flow, and high velocity fluid from the outer region is swept towards the wall to replace the ejected fluid. These events are periodic, and are characterized by the “bursting frequency” which is largely independent of the Reynolds number when the characteristic quantities are non-dimensionalized by the inner viscous scales (Blackwelder and Haritonidis, 1983). It is generally accepted that the near

wall region consists of alternating high and low speed streaks formed as a result of the modulations of the streamwise (u) velocity in the spanwise (z) direction (Marusic and Hutchins, 2005). The streaky structures are shown in figure 1.7.

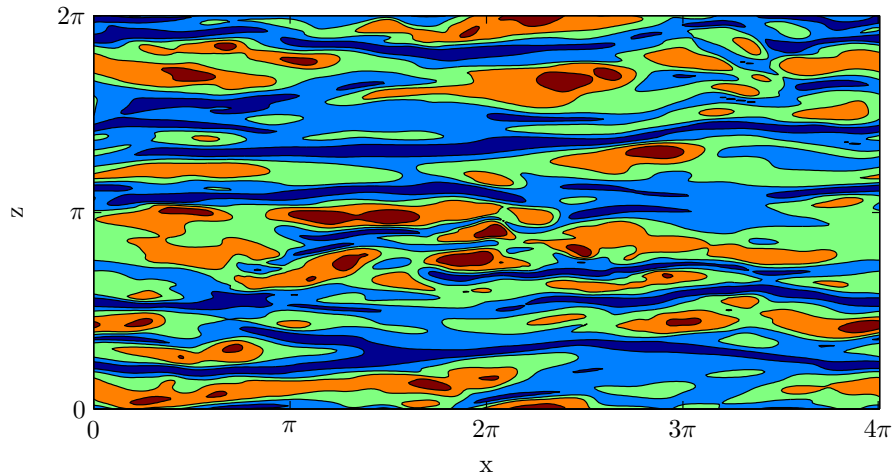


Figure 1.7: Characteristic u' velocity streaks in an $(x-z)$ plane of near-wall turbulence ($y/\delta = 0.08$). High speed and low speed fluid is denoted by red and blue contours, respectively (Hsieh, Biringen, Kucala, and Waggy, 2014).

It is these bursting and sweep events that occur in the near-wall region that produce a majority of the skin-friction drag in turbulent flows. To reduce this skin friction drag, one must somehow disrupt this sequence of events in a beneficial way. A number of passive and active control strategies have been explored in the literature, the most popular being riblets (García-Mayoral and Jiménez, 2011), which are surface protrusions on the surface of airfoils that extend in the streamwise direction. Other less practical methods involve the use of actuating walls, spanwise Lorentz forcing mechanisms, constant injection of fluid, and compliant Kramer-type surfaces (Choi et al., 1997) to attempt to reduce the turbulent skin friction drag.

1.2.2 Active and Passive Control Strategies in Turbulent Flows

Drag reduction in turbulent flows remains an important problem. The potential benefits of realizing efficient flow control systems range from saving billions of dollars in fuel cost for land, air, and sea vehicles to achieve more economically and environmentally competitive industrial processes

involving fluid flows (Gad-el Hak and Tsai, 2006). A number of methods for drag reduction in turbulent flows have been proposed. The simplest method involves directly altering the mean-velocity gradient at the wall through fluid injection, surface heating in air, surface cooling in water, or producing an adverse pressure gradient. However, these are rather power expensive, and often lead to separation (Gad-el Hak et al., 1998) negating the otherwise beneficial effect of relaminarization.

Numerical experiments have shown that spanwise oscillating motion in the turbulent boundary layer can potentially lead to significant decreases in turbulent drag (Jung, Mangiavacchi, and Akhavan, 1992; Laadhari, Skandaji, and Morel, 1994; Choi, Xu, and Sung, 2002) , when the period of oscillation $T^+ = 100$, which is a time scale normalized with respect to inner units. Besides an oscillating wall, other examples where a spanwise oscillation can occur is through a Lorentz force in an electrically conducting fluid (Berger, Kim, Lee, and Lim, 2000; Karniadakis and Choi, 2003). The suppression of turbulence occurs in these cases due to the decrease in the number and intensity of turbulent bursts, where continuous shifting of the longitudinal vortices to different positions relative to the wall-velocity streaks weakens the intensity of the streaks through injecting high-speed fluid into low-speed streaks and low-speed fluid into high-speed regions (Onorato et al., 2006). However, the applicability of actually inducing spanwise oscillations into the turbulent boundary layer has yet to be demonstrated.

The computational work of Choi, Moin, and Kim (1994) and Chang, Collis, and Ramakrishnan (2002) employed opposition control in fully turbulent periodic channel flows, obtaining approximately 20% reduction in turbulent drag. Opposition control samples the wall-normal velocity at some sensing plane above the wall and prescribes an opposing wall-normal velocity through a suction/blowing slot located on the wall (or equivalent wall motion). This method is shown to be effective in suppressing turbulence and reducing turbulent drag (Xu, Deng, Huang, and Cui, 2013). However, the sensing plane would require the use of hot-wire anemometers or some other equivalent system to measure the unsteady perturbations of wall-normal velocity, and a complicated control system of actuators to appropriately assign the correct phase and amplitude of the wall-motion or

suction/blowing surfaces.

One of the more popular proposed passive drag reduction strategies for turbulent boundary layers is to use riblets, which are small surface protrusions aligned with the direction of the mean flow. Riblets of very different geometries have been tested in wind tunnels, demonstrating drag reductions on the order of 10% over flat plates (Walsh and Lindemann, 1984; Viswanath, 2002; Lee and Jang, 2005; García-Mayoral and Jiménez, 2011). The spanwise spacing of riblets is a key component to their effectiveness, where Walsh and Lindemann (1984) found that the optimum spanwise spacing of the riblets should be about $15\nu/u_\tau$. The riblets are also sensitive to orientation angle with respect to the freestream, and at a yaw angle $> 30^\circ$ the drag reduction benefits of riblets is nearly zero (Gad-el Hak et al., 1998). Other passive control strategies include the use of hydrophobic surfaces (Aljallis, Sarshar, Datla, Sikka, Jones, and Choi, 2013) and compliant coatings (Kramer, 1960; Choi, Yang, Clayton, Glover, Atlar, Semenov, and Kulik, 1997; Xu, Rempfer, and Lumley, 2003).

1.2.3 Turbulent Drag Reduction Using Compliant Surfaces

The early experiments of Kramer (1960, 1962), where he replaced a section of a flat-rigid plate with a compliant surface modeled after dolphin skin, showed that the use of a compliant surface can reduce the skin friction in a turbulent boundary layer. However, early attempts to replicate his results failed and the idea was abandoned for a time. It was not until the 1980s when Carpenter and Garrad (1985, 1986) demonstrated theoretically that the onset of transition, mainly through the modulation of TS waves, could be delayed using Kramer-type compliant coatings.

Xu et al. (2003) have demonstrated that compliant materials with realistic properties fail in the presence of high amplitude, nonlinear wave interactions when simulations are continued on long time scales. They have also shown that phase relations between surface wall-normal velocity and the pressure exerted on the wall have a profound and deterministic effect on the effectiveness of the compliant surface. However, it appears that for their design, the correlation between wall-pressure pressure and velocity (a.k.a work rate) was 180° out of phase, and that only when they artificially

reverse the sign of the flow induced pressure on a soft-compliant wall were they able to obtain meaningful skin friction drag.

As elucidated in the experimental study of turbulent control using compliant surfaces by Choi et al. (1997), there are two main requisites for the proper selection of a compliant coating for turbulence control. One is that the dynamic surface roughness of compliant coatings must be small enough, below the value to be considered hydrodynamically smooth. That is, the surface deformation of the compliant surface must remain small. Secondly, the natural frequency of the compliant coatings must be chosen in such a way to interact with the pressure forces to reduce the drag in the boundary layer. It appears that for optimal drag control, the natural frequency needs to fall in the range between the periods of the sweep and ejection events, and that this surface movement may weaken the strength of upwash during ejection events. Obviously, using passive materials to generate surface waves that have a beneficial effect on turbulent drag reduction remains an elusive goal. The spring-backed Kramer surfaces (and other such surfaces) have proven rather ineffective and are susceptible to a number of convective and absolute instabilities, sometimes leading to an increase in turbulent drag (Choi et al., 1997).

1.3 Phononic Crystals

A phonon is a quantized particle or vibrational mode representing mechanical motion and is responsible for the transmission of sound and heat. The field of phononics research contains a wide range of operating frequencies, shown in figure 1.8. Understanding and controlling the phononic properties of materials provides opportunities to insulate buildings from seismic motion, prevent propagation of vibrational waves in structures, convert heat into electricity, and acoustically or thermally cloak objects.

The development of phononic crystals for the control of vibrational waves is based on the idea that a structure composed of a periodic arrangement of scatterers can affect quite strongly the propagation of these waves through a material or structure (Deymier, 2013; Hussein, Leamy, and Ruzzene, 2014). The attenuation or propagation of specific frequencies of such vibrational

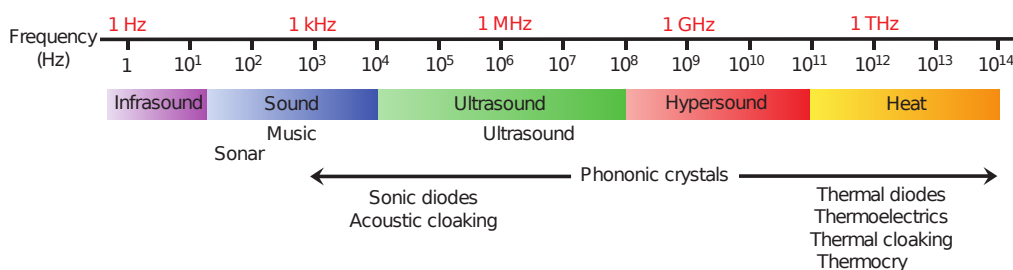


Figure 1.8: The phononic spectrum (Maldovan, 2013)

waves occurs due to destructive or constructive interfaces of the transmitted waves as they pass through a periodic arrangement of materials (Martinezsala, Sancho, Sanchez, Gómez, Llinares, and Meseguer, 1995; Hussein, Hulbert, and Scott, 2006b). The term “stop band” has been used extensively in the literature to describe attenuating waves at specific frequency ranges. In contrast, propagating waves at specific frequency ranges are referred to as “pass bands”. A typical dispersion curve of a 1D phononic crystal is shown in figure 1.9, where the stop band (attenuated waves) corresponds to imaginary wavenumbers and the pass band contains waves with frequencies that have real wavenumber (propagating waves).

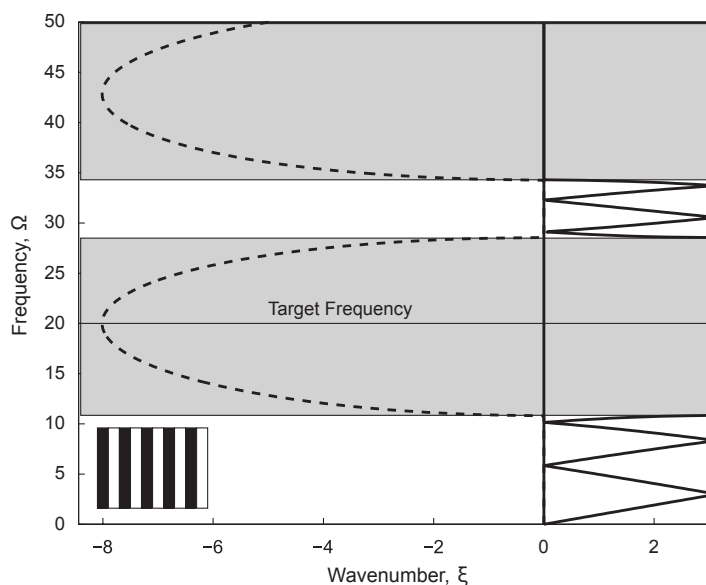


Figure 1.9: Typical dispersion curves for a 1D phononic crystal (Hussein, Hulbert, and Scott, 2007). Solid lines represent pass bands (real wavenumber) and dashed lines represent stop bands (imaginary wavenumber)

These dispersion curves can be generated for a number of periodic structures, where the coefficient of elasticity, mass, and volume fraction of the periodic materials can all be used to design a structure that exhibits stop bands and pass bands at desired frequencies. It is also useful to maximize these band gaps, such that a wide range of otherwise propagating frequencies can be attenuated. Using genetic algorithms, it is possible to optimize band gaps in both 1D (Hussein, Hamza, Hulbert, Scott, and Saitou, 2006a) and 2D (Bilal and Hussein, 2011) phononic crystals. An illustration of these optimized phononic structures and their respective dispersion curves can be found in figure 1.10. The general idea of most phononics research is to exploit the stop band by

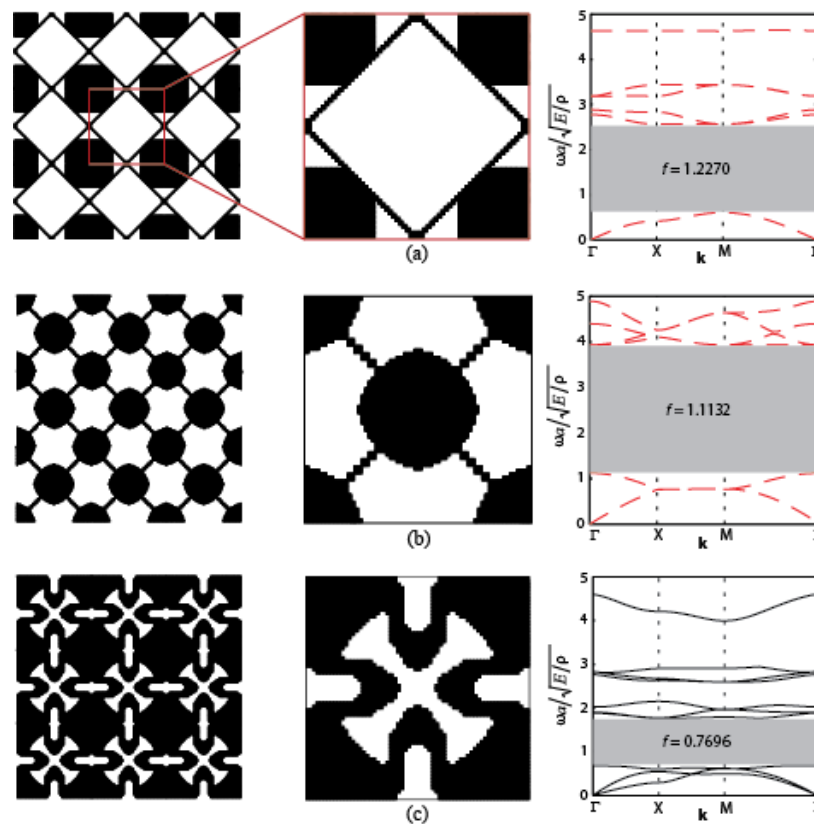


Figure 1.10: Optimized phononic crystals to maximize band gaps adapted from Bilal and Hussein (2011). Images on the left represent the phononic crystal unit cell, with their respective dispersion curves on the right.

designing periodic materials such that certain undesirable frequencies are not allowed to propagate in the medium. For instance, one could design a structure from a phononic crystal such that it does

not allow a range of excitation frequencies to propagate, whereas in the a homogenous structure these excitations would be allowed to propagate. A novel application of this concept could be through the use of phononic crystals to control wave property characteristics in a fluid. The applicability of phononics for this purpose is a new and exciting course of research, where different types of disturbances in a fluid system can be manipulated through a favorable interaction between the fluid/structure interface, dictated by the properties of the phononic structure.

1.4 Thesis Outline

The outline of this thesis is as follows:

- Chapter 2 - Provides an overview of the governing equations used in this work for both the fluid and the phononic crystals is presented. For the fluid this includes the non-dimensionalization of the Navier-Stokes equation as well as the methods used to simulate both periodic and spatially evolving turbulent channel flows. For phononic crystals, the equations of motion governing wave propagation through periodic media is presented, including the generation of dispersion curves and frequency response functions.
- Chapter 3 - This chapter develops the numerical methods of inverting both the fluid and phononic crystal equations, including the method of fluid/structure coupling. For the fluid, we present a semi-implicit fractional time-stepping method massively parallelized using PETSc, including code validation and performance evaluation. For the phononic crystals, the Newmark method is presented which inverts the equations of motion provided in Chapter 2.
- Chapter 4 - This chapter is split into two parts. First, we elucidate the complex secondary transition mechanisms in plane Poiseuille flow whereby two-dimensional TS waves are superimposed with a wide range of three-dimensional modes. By tracking the downstream evolution of the disturbances through spectral analysis and flow visualization, the path of secondary instability in a natural transition environment is determined. In addition, an

efficient active control strategy using a suction/blowing slot is employed which successfully delays transition for this flow. Secondly, the concept of a *phononic subsurface* to realize a passive flow control strategy is presented to reduce the total perturbation energy in a channel undergoing primary (TS wave) transition, transition where multiple unstable waves are excited, and transition in the presence of high-amplitude, weakly nonlinear three-dimensional disturbances.

- Chapter 5 - Bursting events responsible for the production of turbulent kinetic energy in a turbulent channel flow are identified, where both flow visualization and burst detection techniques are employed to detect the frequency of bursting events as well as the structure of turbulence in both periodic and spatially evolving turbulent channel flows. Using this frequency information, a phononic subsurface may then be designed in such a way to possibly disrupt the burst events, thereby destroying the turbulent energy production and thus lowering the skin-friction in a turbulent channel flow.

Chapter 2

Governing Equations

2.1 Fluid Domain

2.1.1 Equations of Motion

The equations that govern the motion of an incompressible, Newtonian fluid is given by

$$\frac{\partial u_i^*}{\partial x_i^*} = 0 \quad (2.1)$$

$$\frac{\partial u_i^*}{\partial t^*} + u_j^* \frac{\partial u_i^*}{\partial x_j^*} = -\frac{1}{\rho_f^*} \frac{\partial p^*}{\partial x_i^*} + \nu^* \frac{\partial^2 u_i^*}{\partial x_j^* \partial x_j^*} \quad (2.2)$$

where Eq. 2.1 represents the conservation of mass for an incompressible flow, and Eq. 2.2 are the equations that govern the conservation of momentum in a fluid. In these equations, $()^*$ represents a dimensional quantity. These equations together are most commonly referred to as the Navier-Stokes equations. Here, u_i^* represents a component of the three-dimensional velocity vector $\mathbf{u}^* = \langle \mathbf{u}^*, \mathbf{v}^*, \mathbf{w}^* \rangle$, t^* represents time, ρ_f^* is the density of the fluid, p^* represents the pressure, and ν^* represents the kinematic velocity.

When the flow field variables are non-dimensionalized by some characteristic velocity U_∞^* and length scale l^* ,

$$u_i = \frac{u_i^*}{U_\infty^*}, \quad x_i = \frac{x_i^*}{l^*}, \quad p = \frac{p^*}{\rho_f^* U_\infty^{*2}}, \quad t = t^* \frac{U_\infty^*}{l} \quad (2.3)$$

respectively Eq. 2.2 becomes

$$\frac{\partial u_i}{\partial t} + \frac{\partial u_j u_i}{\partial x_j} = -\frac{\partial p}{\partial x_i} + \frac{1}{Re} \frac{\partial^2 u_i}{\partial x_j \partial x_j} \quad (2.4)$$

where $Re = U_\infty^* l^* / \nu^*$. In addition, we have combined Eqs. 2.1 and 2.2 such that Eq. 2.4 is now in conservative form, which now implicitly satisfies the conservation of mass.

2.1.2 Spatial Simulation of Channel Flows

For channel flows, the characteristic velocity and length scales are U_c^* and δ^* which are the laminar center-line velocity and channel half-height, respectively. This forms a Reynolds number $Re_c = U_c^* \delta^* / \nu^*$. Using this definition of Reynolds number, and using the solution for the mean pressure gradient

$$\frac{dP}{dx} = -\frac{2}{Re_c} \quad (2.5)$$

Equation 2.4 becomes

$$\frac{\partial u_i}{\partial t} + \frac{\partial u_j u_i}{\partial x_j} = \delta_{i1} \frac{2}{Re_c} - \frac{\partial p}{\partial x_i} + \frac{1}{Re} \frac{\partial u_i}{\partial x_j x_j} \quad (2.6)$$

In order to invert the equations of motion given by Eq. 2.6, it is necessary to apply boundary conditions in the streamwise (x), spanwise (z) and wall-normal (y) equations. For all cases presented, the spanwise (z) boundary conditions are periodic. In the wall-normal (y) direction, the flow is assumed rigid at the walls such that

$$\mathbf{u}(x, y = 0, 2, z, t) = 0 \quad (2.7)$$

unless otherwise stated, where the wall-normal domain spans from $0 \rightarrow 2h$, having a total length of two channel half-heights h . For instance, for a porous suction/blowing slot (or moving wall), the boundary condition on the wall-normal component of the velocity vector v can be replaced as

$$\mathbf{u}(x_s \leq x \leq x_e, y = 0, 2, z) = \langle 0, A_c \cos(\omega t + \phi), 0 \rangle \quad (2.8)$$

where A_c is the amplitude of the control wave, ω is a non-dimensional circular frequency, and ϕ is a wave angle. Of course, any boundary condition may be applied at the walls, provided a suitable function is provided for \mathbf{u} .

For flows that evolve spatially in the streamwise direction, non-periodic boundary conditions must be supplied. At the inflow ($x = 0$), the boundary condition on the flow velocity vector \mathbf{u}

reads

$$\mathbf{u}(x = 0, y, z, t) = \langle (1 - (1 - y)^2), 0, 0 \rangle + \mathbf{u}' \quad (2.9)$$

which is the laminar flow solution for plane-channel flow plus a perturbation. The perturbation velocity \mathbf{u}' , in general is a free parameter. For instance, in a transitional flow, \mathbf{u}' is prescribed as an unstable oscillating eigenfunction from the solution of the Orr-Sommerfeld equation (Eq. 1.3). This may also be prescribed as a random fluctuating field, depending on the case being studied. The treatment of the outflow boundary is detailed in Section 3.1.6.

2.1.3 Turbulent Channel Flows

In order to investigate the bursting phenomenon in Chapter 5, we must simulate turbulence in a channel flow influenced by a mean pressure gradient. The equation of motion follow the Navier-Stokes equation for channel flows (Eq. 2.6) where no-slip boundary conditions are applied at the bottom ($y = 0$) and top walls ($y = 2$) and periodic boundary conditions are placed in the spanwise (z) direction. For a periodic turbulent channel flow, we assume that the streamwise direction is infinite and therefore we apply periodic boundary conditions in that direction. The details of such a simulation are presented in section 2.1.3.1. In spatial turbulent channel flow, no assumptions are made in the streamwise direction and therefore inflow and outflow boundary conditions are applied, the details of these simulations is presented in chapter 5.

2.1.3.1 Periodic Turbulence

In periodic turbulence, the boundary conditions in the streamwise direction are assumed to be periodic. In the periodic turbulent problem, we define the pressure gradient as a function of the Reynolds number

$$Re_c = U_c Re_{cl} \quad (2.10)$$

where

$$Re_{cl} = \frac{U_{cl}^* \delta^*}{\nu^*} \quad (2.11)$$

is the Reynolds number based on the laminar centerline velocity U_{cl}^* and U_c is the mean centerline velocity nondimensionalized by the laminar centerline velocity U_{cl}^* . For a laminar flow, $U_c = 1$ and $Re_c = Re_{cl}$ and Eq. 2.5 is recovered.

Introduction of a random field of disturbances at all points in the flow field will be used to "trip" the flow field into transition as it introduces a wide spectrum of three dimensional modes into the originally one-dimensional flow field. Because there are no inflow conditions in this periodic model, it is important that the mass flux remains constant in the channel. Since the flow field variables are nondimensionalized by U_{cl}^* , U_c will decrease as the flow becomes turbulent. To maintain constant mass flux, the mean streamwise pressure gradient must increase by a factor U_c and does so through Eqs. 2.5 and 2.10.

2.1.3.2 Spatial Turbulence

In spatial turbulence, boundary conditions are present at both the inflow and outflow boundaries and represent a more "realistic" turbulent scenario that may encountered in an actual experimental setup. This is useful when directly comparing experimental data with computational data. Challenges to this method stem from the difficulty in providing an adequate inflow boundary condition and initial condition to the flow field to correctly simulate turbulence. One method would be to provide a laminar inflow solution and perturb it with two-dimensional and three-dimensional modes including high-amplitude random disturbances to force the flow field to transition. However, this is quite costly in terms of resolution as the flow field will require a large streamwise distance to transition into fully-developed turbulent flow and is to be avoided.

Here, we follow the method developed by Chung and Sung (1997) in which crossflow planes from an auxiliary periodic channel flow simulation are used as inflow boundary conditions for the spatial model. These crossflow planes are sampled at a fairly high rate and for a fairly long time such that both the small and large time scales are adequately represented and is verified through observation of the energy spectra and Reynolds stress distributions. Verification of the flow fields are made on a case-by-case basis and will be discussed in detail in Chapter 5. It is important that

both the grid spacings and Reynolds numbers between the periodic and spatial simulations are identical.

2.2 Equations for Phononic Crystals

In describing the solid domain, all variables should be considered in their dimensional form. The governing equation of motion for longitudinal wave propagation in a 1D heterogeneous linear elastic solid is

$$\rho_s \ddot{\eta} = (E\eta_{,s})_{,s} + f, \quad (2.12)$$

where $\eta = \eta(s, t)$, $f = f(s, t)$, $\rho_s = \rho(s)$ and $E = E(s)$ denote longitudinal displacement, external force, solid density and elastic modulus, respectively. The position coordinate and time are denoted by s and t , respectively. The operation $(\cdot)_{,s}$ denotes differentiation with respect to position, while a superposed dot denotes differentiation with respect to time. Four distinct computational problems are solved concerning the solid (phononic crystal) domain.

2.2.1 Problem 1: Phononic subsurface unit-cell dispersion model

To obtain the band structure for a given phononic subsurface unit-cell configuration, we set $f = 0$ in Eq. (2.12) and assume a Bloch solution in the form $\eta(s, t; \kappa) = \tilde{\eta}(s; \kappa)e^{i(\kappa s - \omega t)}$, where $\tilde{\eta}$ is the Bloch displacement function, κ is the wavenumber, ω is the frequency, and $i = \sqrt{-1}$, and apply the periodic boundary conditions, $\tilde{\eta}(s + L_{UC}, \kappa) = \tilde{\eta}(s, \kappa)$, where L_{UC} is the unit-cell length.

2.2.2 Problem 2: Phononic subsurface 10-unit-cell structural dynamics model

In Problem 2, a boundary value problem following Eq. (2.12) is set up for a finite phononic subsurface structure composed of n_c repeated unit cells of the type considered in Problem 1. The boundary conditions chosen are $\eta_{,s}(0, t) = 0$ and $\eta(l, t) = 0$ for the top and bottom boundaries, respectively, where $l = n_c L_{UC}$. A harmonic forcing function is applied only at the top end, i.e., $f(0, t) = \bar{f}(0)e^{i\omega^* t}$ and $f(s, t) = 0$ for $s > 0$, where ω^* is the excitation frequency and \bar{f} is the forcing amplitude. The harmonic displacement response is given by $\eta(s, t) = \bar{\eta}(s)e^{i\omega^* t}$, where $\bar{\eta}(s)$ is the

response amplitude. Upon incorporation of the boundary conditions and the excitation function, and after substitution of the response function into Eq. (2.12), we obtain a frequency response function that describes the steady-state forced response of the structure. In this work, we select $n_c = 10$.

2.2.3 Problems 3 and 4: Phononic subsurface 10-unit-cell wave propagation model

In the third and fourth problems, we re-examine Problem 2 but now as an initial boundary value problem whereby no assumptions are made on the temporal dependency of the displacement field. In Problem 3, we consider the initial conditions $\eta(s, 0) = 0$ and apply a harmonic force $f(0, t) = \bar{f}\sin(\omega^*t)$ for the time interval $0 \leq t \leq t_T$, where t_T is the total simulation time. As in Problem 2, we set $f(s, t) = 0$ for $s > 0$. In Problem 4, we consider the same initial conditions and do not apply any external forcing (the forcing is induced by the interacting flow).

2.3 Fluid/Phononic Structure Interaction

To couple the fluid and solid systems, it is required that the stresses and velocities match at the interface (Förster, Wall, and Ramm, 2006), that is

$$\mathbf{h}^s(t) + \mathbf{h}^f(t) = 0 \text{ on } \Gamma \quad (2.13)$$

$$\mathbf{u}^f(t) - \dot{\mathbf{u}}^s(t) = 0 \text{ on } \Gamma \quad (2.14)$$

where $\mathbf{h} = \boldsymbol{\sigma} \cdot \mathbf{n}$ is the traction vector on either field, \mathbf{n} is the unit normal vector on the solid/fluid interface Γ , and $\boldsymbol{\sigma}$ is the stress tensor for either the fluid or solid. In addition, $\mathbf{u}^f(t)$ and $\dot{\mathbf{u}}^s$ represent the fluid and structure velocities, respectively.

Because the fluid and structure equations are inverted separately (in Problem 4), a conventional serial staggered (CSS) procedure is used to couple the interface between the fluid and phononic surface. A schematic of the CSS procedure is found in figure 2.1 where, in this particular figure as defined by Farhat and Lesoinne (2000), \mathbf{U} represents the structure state-vector $[\mathbf{u} \ \dot{\mathbf{u}}]^T$ and

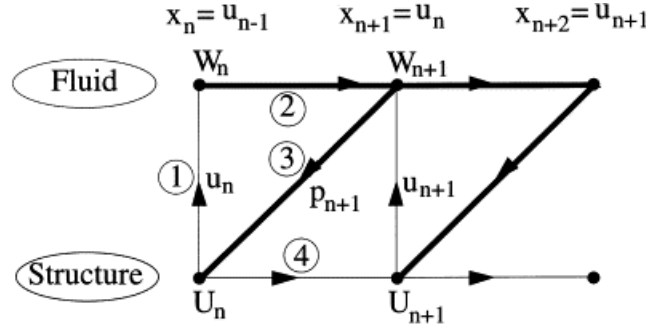


Figure 2.1: CSS: the conventional serial staggered procedure (Farhat and Lesoinne, 2000)

\mathbf{W} represents the fluid velocity, x denotes the interface location, and p represents the pressure. In all terms, the subscript n describes the n th time-step.

The pressure acts on the structure as a force and the resultant displacements at the fluid/solid interface ($\eta(\Gamma)$) obtained from the integration of the structures model are imposed as flow field boundary conditions at the interface such that

$$\hat{u}(x, 0, z, t) = -\eta(\Gamma) \frac{du_b}{dy} \quad (2.15a)$$

$$\hat{v}(x, 0, z, t) = \frac{d\eta(\Gamma)}{dt} \quad (2.15b)$$

These boundary conditions are obtained using a first order Taylor-series expansion assuming small displacements and no tangential (x) displacement of the structure and are an approximation to the exact interface conditions given in Eq. 2.14. It is critical that $\eta(\Gamma) \ll \delta$ where δ represents an inertial length scale in the fluid domain. This restriction must be maintained throughout the computations in order for both the approximation in Eqs. 2.15a and 2.15b to remain valid and so that the structure does not act as a transition promoter if its displacements are large (Morkovin, 1990).

Chapter 3

Numerical Methods

3.1 Fluid Domain

3.1.1 Time Integration Scheme

The numerical method used to integrate Eq. 2.4 is semi-implicit, where we apply the implicit Crank-Nicholson scheme for the vertical diffusion terms. Because mesh stretching results in a very small spacing near the domain boundaries, using an implicit scheme for the diffusion terms allows time-step requirements for numerical stability to be relaxed. For the model equation

$$\frac{\partial u_i}{\partial t} \approx \frac{1}{\text{Re}} \frac{\partial^2 u_i}{\partial x_2^2} \quad (3.1)$$

the Crank-Nicholson scheme can be written as

$$\frac{\hat{u}_i - u_i^n}{\Delta t} \approx \frac{1}{2\text{Re}} \frac{\partial^2 \hat{u}_i}{\partial x_2^2} + \frac{1}{2\text{Re}} \frac{\partial^2 u_i^n}{\partial x_2^2} + \mathcal{O}(\Delta t^2) \quad (3.2)$$

where $\mathcal{O}(\Delta t^2)$ implies that the solution is second-order accurate in time. The predicted velocity \hat{u}_i is obtained from the solution of the linear system

$$\left(1 - \frac{\Delta t}{2\text{Re}} \frac{\partial^2}{\partial x_2^2}\right) \hat{u}_i \approx u_i^n + \frac{\Delta t}{2} M_i^n \quad (3.3)$$

where

$$M_i^n = \frac{1}{\text{Re}} \frac{\partial^2 u_i^n}{\partial x_2^2} \quad (3.4)$$

The remaining terms in Eq. 2.4 (advection, horizontal diffusion, and mean pressure gradient) are advanced using the fully explicit Adams-Bashforth method, which utilizes a two-level integration

technique:

$$\frac{\hat{u}_i - u_i^n}{\Delta t} \approx \frac{3}{2}L_i^n - \frac{1}{2}L_i^{n-1} + \mathcal{O}(\Delta t^2) \quad (3.5)$$

where

$$L_i^n = -\frac{\partial u_i^n u_j^n}{\partial x_j} - \frac{\partial P}{\partial x_i} + \frac{1}{\text{Re}} \left(\frac{\partial^2 u_i^n}{\partial x_1^2} + \frac{\partial^2 u_i^n}{\partial x_2^2} \right) \quad (3.6)$$

Equations 3.5 and 3.6 are fully explicit; this allows each node to independently advance the solution in time completing the predictor step. Combining Eq. 3.3, 3.4, 3.5, and 3.6 yields the following linear system of equations:

$$\left(1 - \frac{\Delta t}{2\text{Re}} \frac{\partial^2}{\partial x_2^2} \right) \hat{u}_i = u_i^n + \Delta t \left(\frac{1}{2}M_i^n + \frac{3}{2}L_i^n - \frac{1}{2}L_i^{n-1} \right) \quad (3.7)$$

where L_i^n and M_i^n are given by Eq. 3.6 and 3.4 respectively.

The velocity field at the advanced time step is obtained by a corrector step to the predicted velocity field,

$$\frac{u_i^{n+1} - \hat{u}_i}{\Delta t} = -\frac{\partial \phi}{\partial x_i} \quad (3.8)$$

Continuity is enforced by taking the divergence of Eq. 3.8 and enforcing $\partial u_i^{n+1}/\partial x_i = 0$. This results in the following linear system for ϕ :

$$\frac{\partial \hat{u}_i}{\partial x_i} = -\Delta t \frac{\partial^2 \phi}{\partial x_i \partial x_i} \quad (3.9)$$

The left-hand-side of Eq. 3.9 is known from solving Eq. 3.7. After solving for ϕ (the pseudo-pressure), the velocity is advanced to the $n + 1$ time step via Eq. 3.8.

3.1.2 Solve for Fractional Velocity and Temperature

The fractional velocity \hat{u}_i is solved using the linear operator previously defined (Eq. 3.7) and the newly computed RHS. For this purpose, the GMRES algorithm is employed which, in these situations, drops the residual by over five orders of magnitude in few iterations (typically 3 – 6). For the system $Ax = b$, the residual can be defined as $r = Ax - b$. PETSc allows the convergence criteria as well as the measure of the residual (e.g.: 2-norm) to be controlled by the user.

The code currently uses the previous solution of \hat{u} as the first guess of the solution in the next time step; if Δt is small, the solution does not vary greatly over one time step. Thus, the number of iterations is reduced by supplying a good initial condition to the solver. The GMRES algorithm could be replaced with incomplete LU factorization, algebraic multigrid, or others. The authors found that this fine-tuning of the solution method with little modification of source-code is one of the best attributes of PETSc.

3.1.3 Solve for Pseudo-Pressure/Updating Velocity

The divergence of the predictor velocity, $\partial\hat{u}_i/\partial x_i$, is a simple operation which requires updating boundary points of each processor in a similar manner as discussed for the explicit terms. Since the pseudo-pressure ϕ is defined on a centered wall-normal y_c mesh, u_2 is interpolated from its original wall y_w grid onto y_c . Upon interpolating and updating boundaries, the LHS of Eq. 3.9 is computed locally.

Solving Eq. 3.9 uses the same GMRES algorithm used for the velocity equations. Neumann conditions ($\partial\phi/\partial x_2 = 0$) are imposed at the lower and upper boundaries. For spatial channel flows, ($\partial\phi/\partial x_1 = 0$) is imposed at the inflow and outflow boundaries. This system is ill-conditioned since a null-space exists in the solution. PETSc provides an easily implemented function which removes the null-space by setting the mean of the pressure field to 0. Since the gradient of the pseudo-pressure is of interest (both for time advancement as well as analysis), removing the null-space is sufficient to obtain an accurate pressure gradient. This can also be achieved by arbitrarily assigning a value to a point in the pressure field in order to correctly pose the problem.

Once the pseudo-pressure is calculated, the velocity field at the advanced timestep, u_i^{n+1} , is computed via Eq. 3.8. Note that the accuracy to which $\nabla \cdot u_i^{n+1} \approx 0$ is dependent upon the accuracy of the solution for ϕ . Our simulations indicate that decreasing the residual of ϕ by five orders of magnitude generally results in an average divergence of approximately 10^{-5} .

3.1.4 Spatial Differences

Spatial differences are approximated using a finite-difference approximation in all coordinate directions. The vertical direction (which incorporates the stretched/staggered mesh) is well suited to this method and high-order Lagrangian polynomials easily accommodate the mesh stretching.

In the present code, finite-differences are used in the horizontal plane, providing a level of versatility for applying to other flow geometries where a stretched grid must be employed in more than one coordinate direction. For example, with only slight modifications, the code can be adapted to model turbulent duct flow (solid boundaries in two directions).

When finite difference methods are employed, dealiasing in the Fourier space has to be replaced with numerical smoothing by artificial viscosity in the physical space in order to dissipate excess energy that cannot be resolved by the grid. This can be accomplished by adding an explicit high-order dissipation term to the finite difference equations, viz.,

$$L_i^n = \dots + \beta \Delta x_i^4 \frac{\partial^4 u_i^n}{\partial x_i^4} \quad (3.10)$$

The coefficient β controls the strength of the dissipation and is bounded by $0 < \beta \leq 0.125$ (Anderson et al., 1984). For typical transition calculations, we keep $\beta = 0.1$.

3.1.5 Parallel Architecture

The above algorithm was implemented using the PETSc libraries. Storage savings are incorporated by only allocating storage for locally owned data on each process and the ghost points from adjacent processes. Similarly, coefficients of linear systems are only saved for local grid points. A sparse storage technique has been implemented to speed up computation the solution of linear systems and save storage.

The scalability of the code was tested (Waggy, Kucala, and Biringen, 2013b) by monitoring the time required to solve a given problem with a varying number of computational resources (strong-scaling). A strong scaling analysis was preformed for two versions of the code. Figure 3.1 demonstrates the strong-scaling of the doubly-periodic code and figure 3.2 demonstrates strong

scaling of the streamwise spatial code. Both codes are parallelized using the PETSc libraries. It is observed that for both codes, the scaling begins to deviate from the ideal scaling at approximately 10^4 unknowns per processor. This scaling, along with our experience in previous simulations on Teragrid resources, lend confidence to the efficiency of the current parallel architecture of the present code.

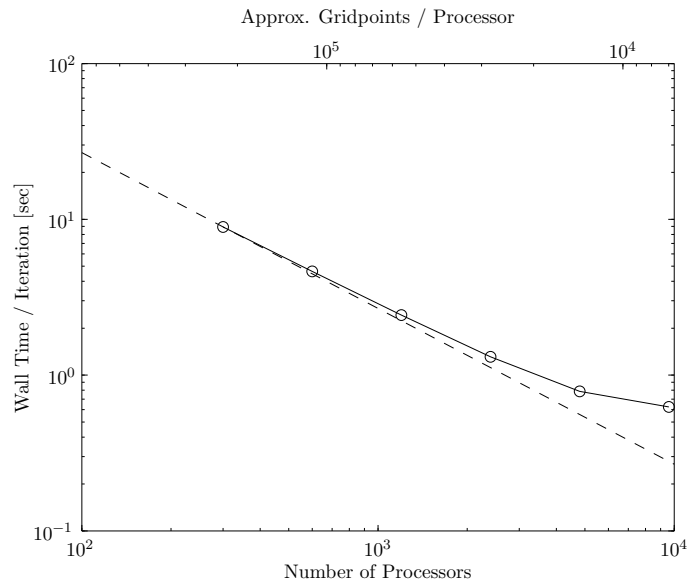


Figure 3.1: Strong scaling for doubly-periodic code: $Re = 1,000$, $512 \times 512 \times 256$, neutrally stratified Ekman Layer. Timing averaged over 200 iterations; startup effects are ignored. Dashed line, theoretical strong scaling; solid line / circles, DNS results.

Improving the efficiency of the code and decreasing the time required per iteration depends upon optimizing the most computationally expensive portion of the code. Monitoring the time required to perform each operation demonstrates the amount of effort spent at each step of the code. A comparison of routines is provided in figure 3.3 for the doubly-periodic code; as before, startup routines have been ignored since these represent a one-time expense and should be small when compared with the total run. The results have been averaged over seven different parallel simulations. The chart clearly demonstrates that the solution of ϕ is by far the most computationally expensive portion of the code accounting for 75% of the total computational time. Due to the stiffness of the problem, the number of iterations required to solve the linear system given

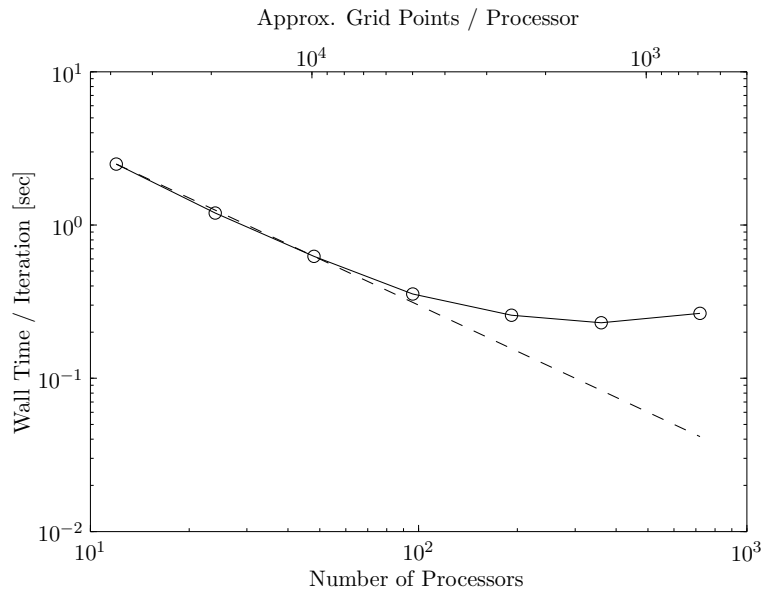


Figure 3.2: Strong scaling for streamwise-spatial code: $Re = 10,000$, $450 \times 16 \times 65$, Channel flow in transition. Timing averaged over 200 iterations; startup effects are ignored. Dashed line, theoretical strong scaling; solid line / circles, DNS results.

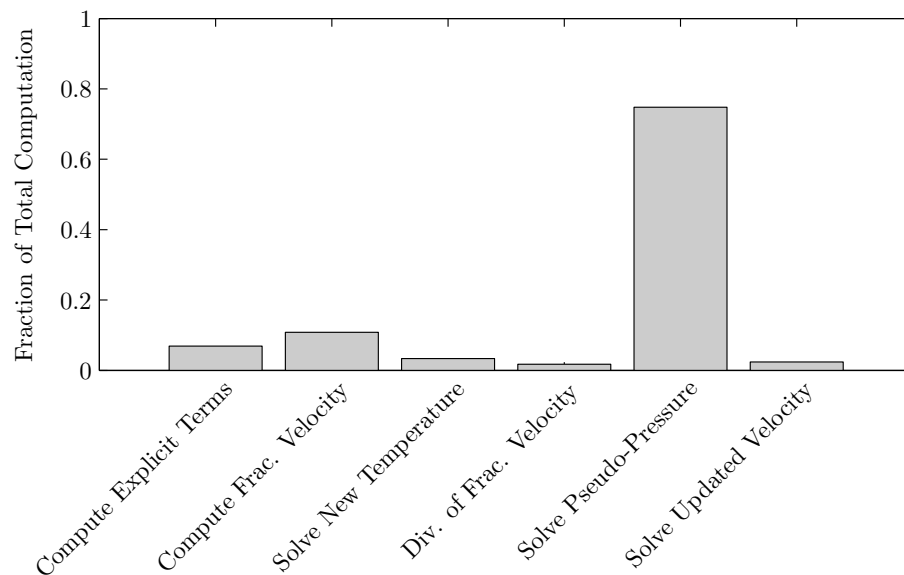


Figure 3.3: Computational Effort for Case B: $Re = 1000$, $512 \times 512 \times 256$, unstably stratified. Results averaged over $300 \leq N_{procs} \leq 9600$.

by Eq. 3.9 dramatically increases over the time required to solve for the velocity and temperature field. While the GMRES algorithm decreased the residual of the velocity and temperature equation

by over 5 orders of magnitude in as little as 10 iterations, the pseudo-pressure equation converges much slower. Figure 3.4 demonstrates a typical convergence curve for solving ϕ . The dashed line

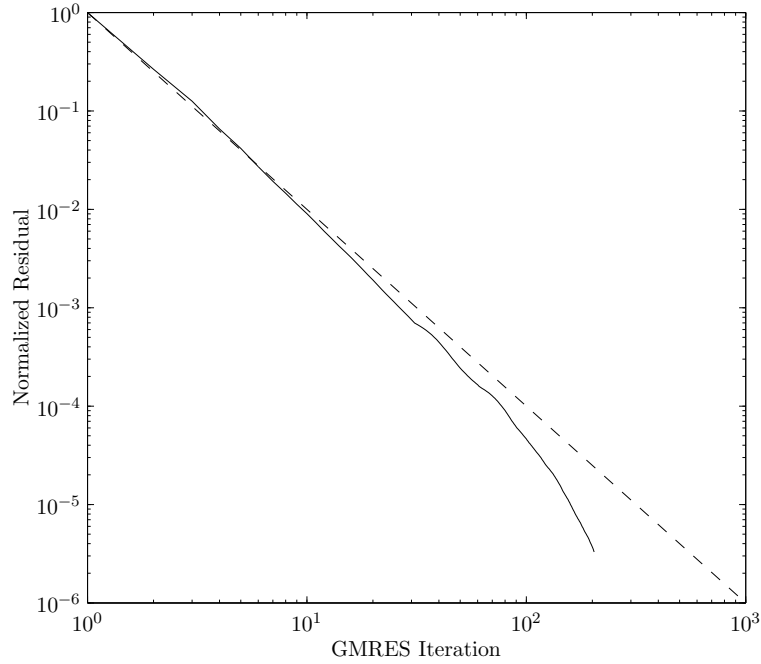


Figure 3.4: Example solution of pseudo-pressure (ϕ) using GMRES algorithm for the periodic code. Solid line, DNS results; dashed line, $\log_{10}(r_i/r_{i-1}) = -2$. Residual normalized by initial residual

represents a converge rate of -2 . Specifically,

$$\log_{10} \left(\frac{r_i}{r_{i-1}} \right) = -2 \quad (3.11)$$

where r_i is the residual of $Ax = b$ at the i^{th} iteration of the GMRES method. We also note that for a given solution procedure such as GMRES, it is possible to decrease the time required to solve the pseudo-pressure equation by relaxing the convergence criteria. Of course because this criteria directly affects the residual divergence of the velocity field, it must be selected such that the magnitude of the quantity remains small. For our simulations we require

$$\|\nabla \cdot u_i^{n+1}\| < 10^{-5} \quad (3.12)$$

Further improvements on the fast solution of the pseudo-pressure ϕ can be made with combining the GMRES algorithm with various pre-conditioners, as well as implementing other other

KSP methods including conjugate-gradient or conjugate-residual methods. The robustness of the PETSc libraries allows us to quickly implement these other methods depending on the problem at hand.

3.1.6 Buffer Domain Technique

In order to prevent reflections at the outflow boundary, a buffer domain technique is employed (Danabasoglu et al., 1991; Kucala and Biringen, 2014) in which the convective terms in the streamwise perturbation equations

$$\frac{\partial uu}{\partial x} = 2u_b \frac{\partial u'}{\partial x} + c(x) \frac{\partial u' u'}{\partial x} \quad (3.13a)$$

$$\frac{\partial uv}{\partial x} = u_b \frac{\partial v'}{\partial x} + c(x) \frac{\partial u' v'}{\partial x} \quad (3.13b)$$

$$\frac{\partial uw}{\partial x} = u_b \frac{\partial w'}{\partial x} + c(x) \frac{\partial u' w'}{\partial x} \quad (3.13c)$$

are smoothly set to zero using a coefficient function

$$c(x) = \frac{1}{2} \tanh [s(L_h - x)] + \frac{1}{2} \quad (3.14)$$

where L_h is half the length of the buffer domain and s is a stretching parameter controlling the gradient of the function.

This allows the perturbations to be convected by the base flow out of the computational domain. The buffer domain is unphysical in a sense that the momentum equations are altered and do not explicitly satisfy conservation of mass and momentum. Therefore, in calculations of the divergence the buffer domain is excluded. Because the accuracy of the derivative is relatively unimportant in the buffer domain, first-order upwinding is used to approximate the streamwise derivatives in the buffer domain to further dissipate any excess energy in the perturbations. In general, the length of the buffer domain is about 20 – 30% of the physical domain. Additionally, the outflow boundary points are included in the inversion of the Navier-Stokes equation (Eq. 3.7)

3.1.7 Pressure Correction

To obtain the pressure at the fluid structure interface, we use the relation

$$p = \phi + \frac{\Delta t}{2Re} \frac{\partial^2 \phi}{\partial x_2^2} \quad (3.15)$$

where p is the non-dimensional “true” pressure, and ϕ is the pseudo-pressure. This transformation is derived due to the numerical method employed here, and because the wall-normal diffusion term is integrated using an implicit method, it appears as a correction term to the “true” pressure. If every term is solved explicitly, the “true” pressure and pseudo-pressure would be identical. Note that the correction term is an order of $O(Re)$ lower than ϕ and thus is quite small and can be considered negligible. However, for completeness any fluid/structure coupling will employ the use of this pressure correction as it is a minor algebraic step and does not significantly impact the performance of the numerical method.

3.1.8 Validation

To assess the accuracy and establish confidence in the present solution method, comparisons between linear theory for both two-dimensional and three-dimensional disturbances for a Reynolds number, $Re = 10,000$ are presented. At this Reynolds number, real frequency $\omega_r = 0.22$, and $\beta_r = \pm 1$ (three-dimensional case), the solution of the Orr-Sommerfeld equation obtains the complex eigenvalues $\alpha_{2D} = 0.9487 - 0.0123i$ and $\alpha_{3D} = 0.7730 + 0.0277i$ for the two-dimensional and three-dimensional disturbances, respectively. The value of ω_r was chosen such that it yields the least stable eigenvalue for $Re = 10,000$ for two-dimensional disturbances. The corresponding spatial eigenfunctions of the Orr-Sommerfeld equation are introduced at inflow with real frequency ω_r and real spanwise wavenumber β_r . For both the two-dimensional and three-dimensional cases, approximately 60 grid points per TS wavelength were used in the streamwise direction, and 64 grid points per wavelength were used in the spanwise direction. At the inflow, the maximum amplitude of the two-dimensional and three-dimensional disturbances were 0.1% of U_c . The time step was chosen such that the maximum Courant-Friedrichs-Lewy (CFL) number remained on the order of

10^{-1} and resolves each TS period into roughly 2000 time steps.

Modal distributions of the wall-integrated kinetic energy

$$E = \frac{1}{2} \int_0^2 (u'^2 + v'^2 + w'^2) dy \quad (3.16)$$

are used as a metric to measure the spatial growth rates of the low-amplitude inflow disturbances. These distributions, presented in figure 3.5, display excellent agreement with the linear theory, with a maximum deviation of 0.05% (two-dimensional) and 0.48% (three-dimensional), measured approximately four TS wavelengths downstream of the inflow. Hence, these results establish confidence in the present numerical method to accurately predict the spatial growth rates of low amplitude two-dimensional and three-dimensional disturbances.

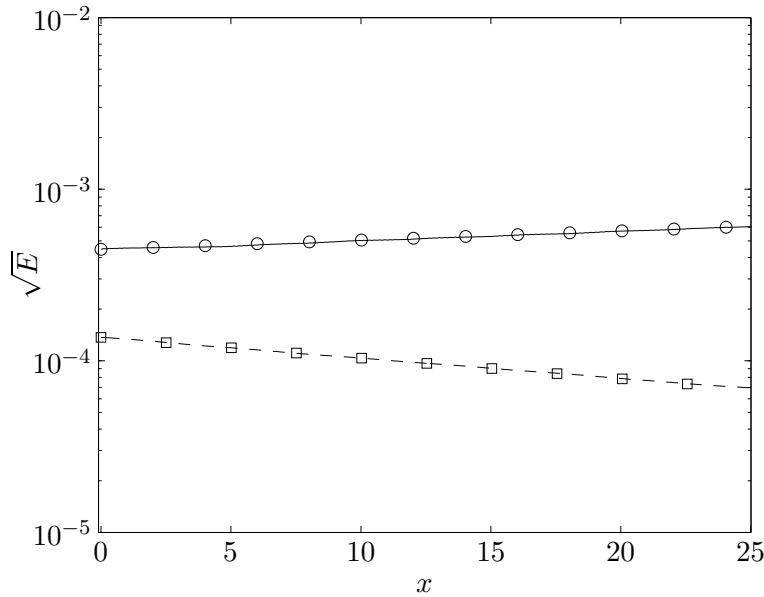


Figure 3.5: Spatial evolution of the (1,0) (solid line) and (1,1) (dashed line) modes for the two-dimensional and three-dimensional disturbances, respectively. \circ : two-dimensional linear theory, \square : three-dimensional linear theory.

3.2 Numerical Methods for Phononic Structures

We numerically analyze the 1D solid domain representing the phononic subsurface using the finite element (FE) method utilizing 1D 2-node iso-parametric elements (Hussein et al., 2006b).

Upon discretization of the unit cell in Problem 1, we obtain a mass matrix, $\tilde{\mathbf{M}}$, and a stiffness matrix, $\tilde{\mathbf{K}}(\kappa)$. Following the Rayleigh proportional damping model, the unit-cell damping matrix is defined as $\tilde{\mathbf{C}} = q_1 \tilde{\mathbf{M}} + q_2 \tilde{\mathbf{K}}$ where q_1 and q_2 are damping constants. The dispersion band structure is obtained by solving the eigenvalue problem $[-\omega^2 \tilde{\mathbf{M}} + i\omega(q_1 \tilde{\mathbf{M}} + q_2 \tilde{\mathbf{K}}(\kappa)) + \tilde{\mathbf{K}}(\kappa)]\tilde{\mathbf{D}} = \mathbf{0}$, where $\tilde{\mathbf{D}} = [\tilde{d}_1 \ \tilde{d}_2 \ \dots \ \tilde{d}_{n_m-1}]^T$ is the Bloch vector, for values of wavenumber in the range $0 \leq \kappa \leq \pi/L_{UC}$ [see Ref. Hussein (2009) for a solution scheme for this form of eigenvalue problem]. The number of nodes in the unit cell is denoted by n_m .

In Problems 2-4 (sections 2.2.2 & 2.2.3), we use the FE method to spatially discretize the entire 10-unit-cell structure (in Problem 4 we also consider homogeneous structures for comparison). For Problem 2, we obtain the matrix problem $[-\omega^{*2} \mathbf{M} + i\omega^*(q_1 \mathbf{M} + q_2 \mathbf{K}) + \mathbf{K}]\mathbf{D} = \mathbf{F}$, where $\mathbf{D} = [d_1 \ d_2 \ \dots \ d_{n_s}]^T$ is a vector of nodal displacements representing the discretized steady-state response, and $\mathbf{F} = [\bar{f}_1 \ \bar{f}_2 \ \dots \ \bar{f}_{n_s}]^T = [\bar{f}_1 \ 0 \ \dots \ 0]^T$ is the harmonic forcing amplitude vector with a nonzero entry only at position $s = 0$. The number of nodes along the entire structure is $n_s = n_c(n_m - 1) + 1$. In figure 1, $\bar{\eta}(0) \approx d_1$ and $\langle \phi(\omega^*) \rangle \approx 1/n \sum_{i=1}^n [f_1^{(i)}/\bar{f}] \cdot [d_1^{(i)}/\max_{i=1}^n(d_1^{(i)})]$, where $n = 4 \times 10^6$.

For Problems 3 and 4 (section 2.2.3), the second order Newmark scheme is used for the time integration. The FE matrix equations following the scheme are

$$\mathbf{D}^{(i+1)} = \mathbf{D}^{(i)} + \Delta t \mathbf{V}^{(i)} + (\Delta t)^2 \left[\left(\frac{1}{2} - \beta \right) \mathbf{A}^{(i)} + \beta \mathbf{A}^{(i+1)} \right], \quad (3.17)$$

$$\mathbf{V}^{(i+1)} = \mathbf{V}^{(i)} + \Delta t \left[(1 - \gamma) \mathbf{A}^{(i)} + \mathbf{A}^{(i+1)} \right], \quad (3.18)$$

$$\mathbf{A}^{(i+1)} = \mathbf{T}^{-1} \left[-\mathbf{K}\mathbf{D}^{(i+1)} - \mathbf{C}\mathbf{V}^{(i)} - \frac{\Delta t}{2} \mathbf{C}\mathbf{A}^{(i)} + \mathbf{F}^{(i+1)} \right], \quad (3.19)$$

where $\mathbf{D}^{(i)}$, $\mathbf{V}^{(i)}$, $\mathbf{A}^{(i)}$, and $\mathbf{F}^{(i)}$ represent the displacement, velocity, acceleration, and force vectors at the i^{th} time-step, Δt is the time step increment, and $\mathbf{T} = \mathbf{M} + \frac{\Delta t}{2} \mathbf{C}$. Here, $\mathbf{D}^{(i)} = [d_1^{(i)} \ d_2^{(i)} \ \dots \ d_{n_s}^{(i)}]^T$ and $\mathbf{F}^{(i)} = [f_1^{(i)} \ f_2^{(i)} \ \dots \ f_{n_s}^{(i)}]^T$. For Problem 3, $\mathbf{F}^{(i)} = [\bar{f}_1 \ 0 \ \dots \ 0]^T \sin(\omega^* i \Delta t)$; for Problem 4, $f_1^{(i)}$ is obtained from the flow solution (as described below) and all other terms in the $\mathbf{F}^{(i)}$ vector are set to zero. The value of Δt is chosen such that the simulation is both accurate and stable for a given forcing frequency ω^* . By selecting $\gamma = 1/2$ and $\beta = 0$, the scheme is rendered fully explicit with an accuracy on the order of $O(\Delta t^2)$. The solution procedure is as follows. At

each time step i , the displacement at the following time step $i + 1$ is first obtained, from Eq. (3.17). After which, Eq. (3.19) is solved for the unknown acceleration $\mathbf{A}^{(i+1)}$. Due to the incorporation of damping, \mathbf{T} is generally not a diagonal matrix and thus obtaining \mathbf{T}^{-1} is computationally expensive and introduces numerical errors, especially for large size matrices. However, utilizing the property that \mathbf{T} is a tridiagonal matrix, we use the compact-storage Thomas algorithm, which is an efficient form of Gaussian elimination suited for tridiagonal systems. Finally, Eq. (3.18) is used to obtain the updated velocity. This process is repeated allowing the simulation to march forward in time until it reaches t_{fin} . It is noteworthy that if $\mathbf{C} = \mathbf{0}$, Eq. (3.19) becomes

$$\mathbf{A}^{(i+1)} = \mathbf{M}^{-1} \left[\mathbf{F}^{(i+1)} - \mathbf{K}\mathbf{D}^{(i+1)} \right], \quad (3.20)$$

and the computational cost of the problem reduces significantly because \mathbf{M} is a diagonal matrix.

Chapter 4

Control of Channel Flows in Transition

In this chapter, we consider a plane-channel flow bounded by two walls and influenced by a mean pressure gradient, the details of such a flow can be found in Section 2.1.2. Each section in this chapter considers a distinct channel flow transition problem. In Section 4.1 we consider a channel flow in which a two dimensional Tollmien-Schlichting (TS) wave is superimposed with random noise at the inflow to determine the path of secondary transition the flow field experiences based on the amplitude of the TS wave. This secondary instability can either be K-type (after Klebanoff) or H-type (after Herbert) (see section 1.1.2). We then apply an active control strategy that consists of a suction/blowing slot which is phase lagged with respect to the pressure signal of the TS wave. Using this strategy, we achieve a significant reduction in the energy of the TS mode, and consequently, the total energy in the flow field through alteration of the turbulent production (Kucala and Biringen, 2014).

As an alternative to this active control strategy, we apply a novel passive control strategy using a periodic medium deemed a *phononic subsurface**. This phononic subsurface acts to alter the phase between the wall pressure signal and displacements at the fluid/structure interface and can act to stabilize or destabilize the unstable TS wave. Stabilization occurs when this phase

*This work was done in collaboration with Professor Hussein and Osama Bilal where they handled most of the analysis and design aspects of the phononic subsurfaces, including the unit cell design and optimization of the band gap that is vitally important to characterize the effect of the subsurface on the flow field. Therefore, the work presented in this chapter will mostly contain the analysis of the influence of the phononic subsurface on the the flow field quantities. See Hussein, Biringen, Bilal, and Kucala (2015).

relationship between the two signals is predominantly out of phase, and destabilization occurs when the two signals are in phase. This alters the correlations between the streamwise (\hat{u}) and wall-normal (\hat{v}) perturbation velocities and lowers the rate of perturbation energy production of the TS waves. These phononic subsurfaces are used to control a number transition scenarios:

- Channel flow in transition with a single unstable wave (Section 4.2)
- Channel flow in transition with multiple unstable waves (Section 4.3)
- Channel flow in K-type (3D) transition (Section 4.4)

In each of these studies, we examine a number of quantities including the perturbation energy growth in time and space, the correlations between velocity components, the effect of using multiple phononic subsurfaces on the flow field, rate of perturbation energy production, and other such measures to carefully characterize the influence of the phononic subsurface on the flow field. Each section will include an introduction, methods, results, and conclusions subsection to describe the unique aspects of each problem

4.1 Spatial Simulation of Channel Flow Instability and Control

4.1.1 Introduction

A common path to transition from laminar to turbulent flow in plane-channel and boundary-layer flows occurs when an initially two-dimensional (primary) instability, also known as the Tollmien-Schlichting (TS) wave, becomes susceptible to three-dimensional disturbances at some finite amplitude. This is known as the secondary instability and is characterized by the appearance of either K-type or H-type disturbance patterns. K-type instabilities (after Klebanoff) were first observed in the ground-breaking boundary-layer experiments of Klebanoff, Tidstrom, and Sargent (1962), and later in plane-channel flow experiments by Nishioka, Asai, and Iida (1980). These are characterized by Λ -shaped structures (Λ vortices) arranging themselves in a distinctive pattern periodic in the streamwise (x) and spanwise (z) directions such that $x \rightarrow x + \lambda_x$ and $z \rightarrow z + \lambda_z$, where λ_x is the streamwise wavelength of the primary (TS) instability and λ_z is the spanwise wavelength of the secondary instability.

As an alternate path to secondary instability, Herbert theoretically predicted the onset of subharmonic modes in both channel flows (Herbert, 1983) and boundary layers (Herbert, 1988) for low two-dimensional amplitudes; Herbert's theory also predicted a mixing of fundamental and subharmonic modes for higher two-dimensional amplitudes. The subharmonic mode is labeled as H-type (after Herbert) and is characterized by a staggered arrangement of Λ vortices invariant to coordinate transformations of the type $x \rightarrow x + 2\lambda_x$ and $z \rightarrow z + \lambda_z$, and by the combined shift $(x, z) \rightarrow (x + \lambda_x, z + \lambda_z/2)$. That is, the subharmonic secondary instability has a streamwise wavelength λ_x that is twice the length of the primary TS wave. The existence of H-type (subharmonic) instability was confirmed in the boundary layer experiments of Kachanov, Kozlov, and Levchenko (1978); Kachanov and Levchenko (1984) and Saric, Kozlov, and Levchenko (1984). In a more recent experimental study considering boundary layer flow with adverse pressure gradient (Borodulin, Kachanov, and Koptsev, 2002), a large band of subharmonic and harmonic modes were found to amplify with random noise, with and without the primary TS wave being forced at the

inflow.

The existence of H- and K-type instability was also captured in temporal direct numerical simulations in doubly periodic domains (Spalart and Yang, 1987; May and Kleiser, 1985; Singer, Reed, and Ferziger, 1989). In these studies, several discrepancies between computational and experimental studies were observed. For example, the boundary layer simulations of Spalart and Yang (1987) did not reveal the existence of pure K-type instability at large two-dimensional amplitudes; instead a mixture of H- and K-type instabilities were detected. This is in contrast with the experiments of Saric, Kozlov, and Levchenko (1984) which clearly identified the formation of K-type structures.

In a similar vein, the direct simulations of Singer (1987) and Singer et al. (1989) obtained a mixture of H- and K- type instability with high amplitude initial two-dimensional disturbances, whereas in the channel flow experiments of Nishioka et al. (1980) secondary instability was pure K-type. Furthermore, channel flow experiments have not revealed H-type instability except in the presence of a forced subharmonic (Ramazanov, 1985), while computations (Singer, 1987; Singer et al., 1989), (May and Kleiser, 1985) and theory (Herbert, 1983), predict the evolution of H-type secondary instability for low two-dimensional excitation amplitudes.

The present study follows the temporal direct numerical simulations (DNS) conducted by Singer (1987); Singer et al. (1989) and Kim and Moser (1989) in a spatially evolving numerical simulation to assess the dominance of either subharmonic or fundamental instability in the path to natural transition. In this paper we define the modes as multiples of the real fundamental frequency ω_r and real spanwise wavenumber $\beta_r = 2\pi/L_z$ such that $\omega = n\omega_r$ and $\beta = m\beta_r$. Every mode can then be expressed as a pair (n, m) , the primary mode being $(1, 0)$. To replicate the vibrating ribbon commonly used in laboratory experiments, the inflow conditions consist of the superposition of a two-dimensional primary TS wave with low-amplitude random noise allowing the growth of the fundamental $(1, m)$, or subharmonic $(0.5, m)$ modes, depending on the amplitude of the primary wave in a spatially evolving channel.

Control of these H- or K-type instabilities were initiated through a spanwise-homogeneous

suction/blowing slot located at a fixed streamwise location in the channel in order to reduce the amplitude of the primary TS wave, thus delaying transition. This method of transition delay, proposed by Biringen (1984) has been demonstrated to reduce the growth of the TS wave in both experiments (Erdmann, Patzold, Engert, Peltzer, and Nitsche, 2011; Baumann and Nitsche, 1996) and computations (Danabasoglu, Biringen, and Streett, 1991). Similarly, the computational work of Choi, Moin, and Kim (1994) and Chang, Collis, and Ramakrishnan (2002) employed opposition control in fully turbulent periodic channel flows, obtaining approximately 20% reduction in turbulent drag. Opposition control samples the wall-normal velocity at some sensing plane above the wall and prescribes an opposing wall-normal velocity through a suction/blowing slot located on the wall. Erdmann et al. (2011) demonstrated the applicability of opposition control in two-dimensional boundary layer transition using an actuating membrane which reduced the amplitude of the primary TS wave by almost 90%. In this case, measurement of the velocity perturbations were made using a hot-wire anemometer which allowed for the proper “tuning” of the control signal for the reduction in the TS wave. In the control cases presented in this paper, the control signal will be tuned using a wall-pressure measurement upstream of the control slot, as opposed to the wall-normal velocity.

4.1.2 Numerical Method

The full nonlinear, time-dependent three-dimensional Navier-Stokes equations are solved in a spatially developing channel flow using a fractional step method (Waggy, Biringen, and Sullivan, 2013a). With all spatial coordinates non-dimensionalized by the channel half-height δ and velocities by the centerline velocity U_c , the Navier-Stokes equations read (in conservative form)

$$\frac{\partial u_i}{\partial x_i} = 0 \quad (4.1)$$

$$\frac{\partial u_i}{\partial t} + \frac{\partial u_j u_i}{\partial x_j} = -\frac{\partial p}{\partial x_i} + \frac{1}{Re} \frac{\partial u_i}{\partial x_j x_j} \quad (4.2)$$

where $Re = U_c \delta / \nu$, ν is the kinematic viscosity, and the vector $\mathbf{u} = \langle u, v, w \rangle$ is composed of three velocity components in the x (streamwise), y (wall-normal), and z (spanwise) directions,

respectively. Also, p represents non-dimensionalized pressure and t represents non-dimensionalized time.

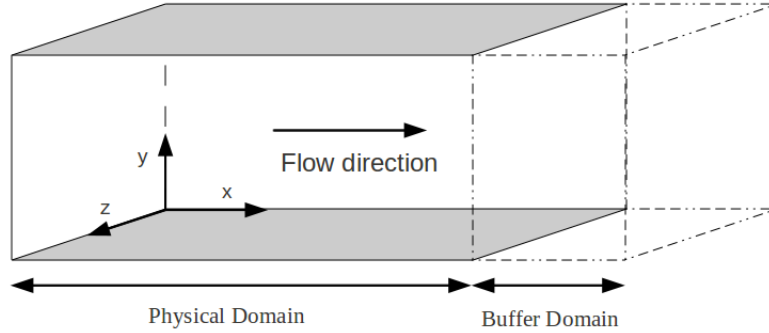


Figure 4.1: Flow geometry and coordinate system for present channel-flow simulation.

The spatial derivatives are computed using fourth order central differences, where the vertical diffusion terms are solved implicitly and the rest of the terms solved explicitly. Hence the time integration is a semi-implicit Adams-Bashforth/Crank-Nicolson type method, which makes the numerical procedure second order accurate in time. The streamwise (u) and spanwise (w) velocity components are discretized on a “centered” vertical mesh, while the wall-normal (v) velocity component is discretized on a “staggered” vertical mesh to enhance coupling between the the vertical velocity and the pressure (Waggy et al., 2013a). The flow geometry is shown in figure 4.1. In Eqs. (4.1) and (4.2), the velocity vector can be decomposed into a base \mathbf{u}_b and a fluctuating component \mathbf{u}' such that

$$\mathbf{u} = \mathbf{u}_b + \mathbf{u}' \quad (4.3)$$

Using the definition of velocity presented in Eq. (4.3), the initial/boundary conditions can be written as

$$\mathbf{u}_b(x = 0, 0 \leq y \leq 2, z) = \langle 1 - (1 - y)^2, 0, 0 \rangle \quad (4.4a)$$

$$\mathbf{u}'(x = 0, y, z, t) = A_{2D} \text{Real}[\mathbf{u}_{e2D}(z)e^{-i\omega_r t}] + \mathbf{u}_r(y, z, t) \quad (4.4b)$$

$$\mathbf{u}(x, y = 0, 2, z) = 0 \quad (4.4c)$$

where A_{2D} is the amplitude of the two-dimensional disturbance and \mathbf{u}_r is a vector field of random

noise applied at the inflow. The amplitude of each component in the random vector field is bounded by A_r and is uniformly distributed in wave space such that there is no wavenumber biasing at the inflow. In addition, $i = \sqrt{-1}$, ω_r is the real frequency of the solution of the Orr-Sommerfeld equation (see Section 2.1), and \mathbf{u}_{e2D} is the corresponding two-dimensional eigenfunction. Also Eq. (4.4a) is the laminar solution for plane Poiseuille flow, where the channel height spans from $0 \rightarrow 2\delta$. For the present simulations, the mass flux is constant throughout the entire domain, as the eigenfunctions themselves explicitly preserve massflow at the inflow for all times, owing to the negative-symmetry of the streamwise perturbation velocity about the channel centerline. Therefore at all times the mass flux is held constant at the inflow boundary providing a realistic model for comparison with experimental data (Barkley, 1990).

The outflow boundary conditions for the spatially evolving (non-periodic) channel flow are modeled as a buffer domain appended to the computational domain (figure 4.1). In the buffer domain, the streamwise perturbation convective and viscous terms in the momentum equation, as well as the right-hand side of the pressure equation, are smoothly reduced to zero using a hyperbolic tangent function (Danabasoglu et al., 1991; Saiki et al., 1993). Periodic boundary conditions are applied in the spanwise (z) direction.

For active control cases the no-slip boundary condition in Eq. 4.4c is modified to include

$$\mathbf{u}(x_s \leq x \leq x_e, y = 0, 2, z) = \langle 0, A_c \cos(\omega_r t + \phi), 0 \rangle \quad (4.5)$$

where x_s represents the front-edge of the suction-blowing slot, x_e represents the back-edge of the slot, and ϕ represents the phase angle, which determines the phase of the control wave. The slot extends along the width of the channel in the spanwise direction, ensuring that the control signal is purely two-dimensional. A_c represents the amplitude of the control wave, and can be varied depending on the amplitude of the wall-normal velocity component of the primary TS wave in accordance with Biringen (1984).

The flow parameters $Re = 10,000$, $\omega_r = 0.22$ were chosen to closely duplicate the conditions of the temporal simulation of Kim and Moser (1989), where the frequency has been selected

| Case | A_{2D} | A_r | $N_x \times N_y \times N_z$ |
|------|-----------|------------|-----------------------------|
| L-A | $0.01U_c$ | $0.001U_c$ | $696 \times 65 \times 128$ |
| H-A | $0.02U_c$ | $0.001U_c$ | $696 \times 97 \times 128$ |

Table 4.1: Computational parameters for $Re = 10,000$, $\omega_r = 0.22$

such that the least stable primary mode is amplified. The amplitudes of the inflow disturbances are $A_{2D} = 0.01U_c$ and $A_{2D} = 0.02U_c$ and are referred to as the low-amplitude (L-A) and high-amplitude (H-A) cases, respectively. Both the L-A and H-A cases impose the two-dimensional spatial eigenmodes of the Orr-Sommerfeld (O-S) solution at the inflow, simulating the effects of a vibrating ribbon common in transition experiments. In both cases, the amplitude of the random disturbance, $A_r = 0.001U_c$, is set to simulate a “natural” disturbance environment (Singer et al., 1989), where a wide spectrum of unbiased modes might be present at the inflow.

For the results that follow, the physical domain lengths are $L_x = 55\delta$, $L_y = 2\delta$, $L_z = 4\pi\delta$. The streamwise physical domain length is chosen such that the inflow conditions will allow for the development of distinct K- or H-type disturbance patterns, where the buffer domain extends from $55 \leq x \leq 75$ and encompasses approximately 26% of the total channel length. A summary of the computational parameters is provided in Table 4.1.

4.1.3 Modal Evolution of Secondary Instability

Spectra of vertically averaged perturbation kinetic energy per unit mass

$$E = \frac{1}{2} \int_0^2 (u'^2 + v'^2 + w'^2) dy \quad (4.6)$$

for the L-A and H-A cases are presented in figures 4.2(a) and 4.2(b), respectively, at $x = 55.80$. In these figures, energy in the primary two-dimensional mode (1,0) was removed, allowing only the observation of the three-dimensional modes to determine K- or H-type dominance. The kinetic energy spectra were obtained over two full periods $T_{TS} = 2\pi/\omega_r$ of the primary disturbance to capture the fundamental and the subharmonic modes. For both the L-A and H-A cases, the amplitudes in the subharmonic ($\omega = 0.5$) and fundamental modes ($\omega = 1$) decrease logarithmically

with increasing spanwise wavenumber β . For the L-A case, the subharmonic modes are about an order of magnitude higher in amplitude for spanwise wavenumbers $0.5 \leq \beta \leq 4$ when compared with the fundamental modes, indicative of H-type dominance in the largest scales. The higher spanwise wavenumbers do not show the same separation, as the intermodal energy transfer mechanisms that determine either K-type or H-type instability occur at the larger scales. For the H-A case, there is evidence of mixed modes at low wavenumbers, where the subharmonic and fundamental modes are approximately of the same amplitude. Consequently, it can be inferred that for the L-A case, there is dominance of H-type instability whereas the H-A case is characterized by mixed modes at the lower spanwise wavenumbers, showing no dominance of K-type or H-type instability.

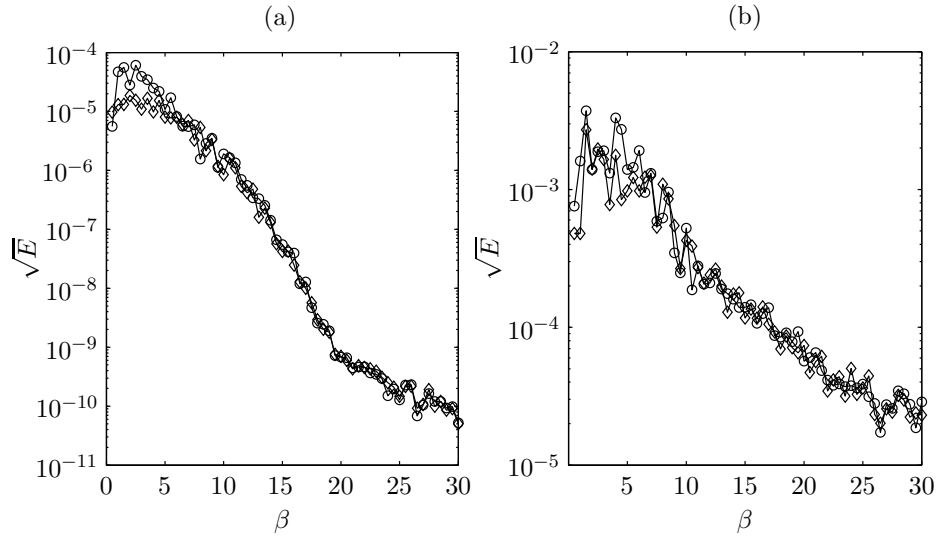


Figure 4.2: Spectrum of vertically averaged kinetic energy at $x = 55.80$ for case (a) L-A, (b) H-A; \circ : $\omega = 0.5$ (subharmonic), \diamond : $\omega = 1$ (fundamental).

Streamwise evolution of the energy containing modes for the L-A and H-A cases are presented in figures 4.3(a) and 4.3(b), respectively. For the L-A case, the two-dimensional mode $(1, 0)$ grows exponentially, as predicted by the linear theory. For $x \geq 40$ the subharmonic modes $(0.5, 1)$ and $(0.5, 2.5)$ have higher amplitudes than their fundamental counterparts indicating H-type dominance, in agreement with the observations of Singer et al. (1989) and Herbert (1983). It is also evident that modal energy amplification is on the order $O(10^1)$ throughout the computational domain. There

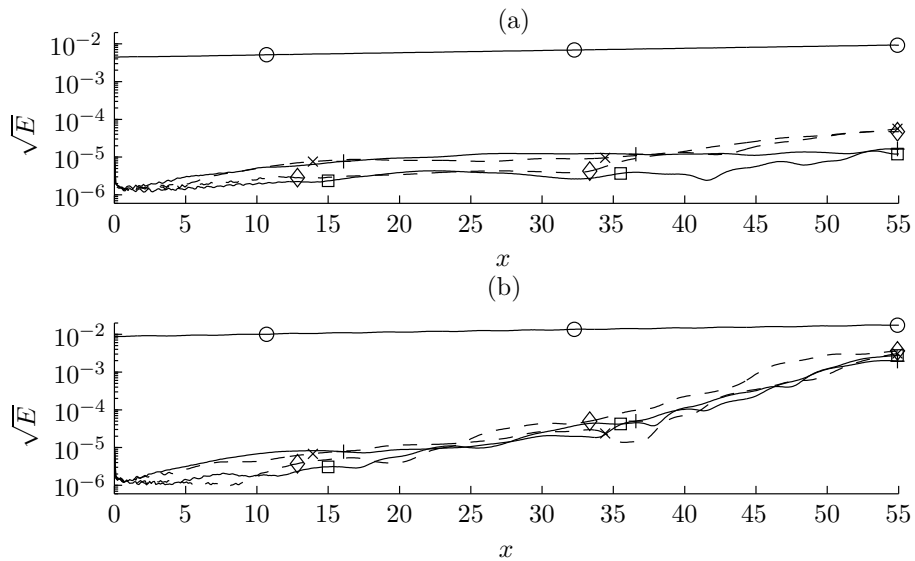


Figure 4.3: Streamwise evolution of vertically averaged kinetic energy for specific modes for (a) case L-A, \circ : (1, 0), \diamond : (0.5, 1), \times : (0.5, 2.5), \square : (1, 1), $+$: (1, 2.5)

, (b) case H-A, \circ : (1, 0), \diamond : (0.5, 1.5), \times : (0.5, 4), \square : (1, 1.5), $+$: (1, 4). Solid lines represent fundamental modes while dashed lines represent subharmonic modes.

is, however, a competition between the fundamental (solid lines) and subharmonic (dashed lines) modes from $0 \leq x \leq 40$, where the amplitudes of the two modes are comparable for a given spanwise wavenumber β . As the disturbances travel downstream, the H-type modes are preferentially excited and become dominant.

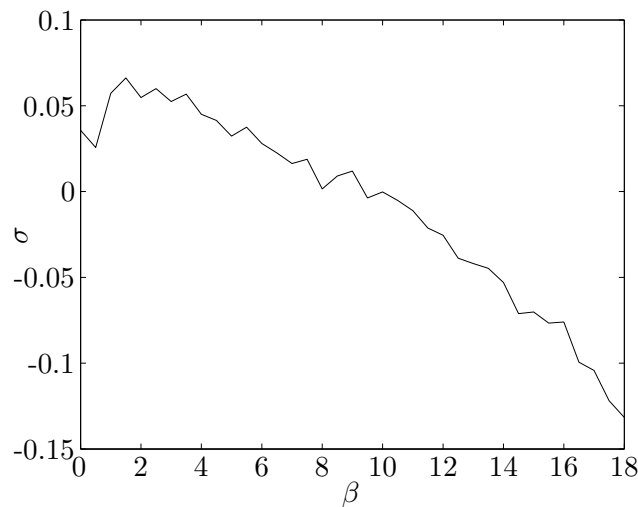


Figure 4.4: Growth rate σ of the subharmonic mode as a function of the spanwise wavenumber β measured at the end of the channel

Figure 4.4 shows the growth rate σ as a function of the spanwise wavenumber β for the L-A case. The maximum growth of the subharmonic mode occurs at $\beta = 1.5$, roughly corresponding to the maximum growth rate calculated by Herbert (1983), $\beta = 1.26$. This discrepancy can be attributed to the finite length of the periodic spanwise domain $L_z = 4\pi\delta$ which yields wavenumbers as multiples of 0.5. In addition, an approximately linear decay in the growth rate with increasing β is observed in figure 4.4, comparable to Hebert's (1983) analysis for H-type instability.

For the H-A case, (figure 4.3(b)), there is competition between the fundamental (solid lines) and subharmonic (dashed lines) modes similar to that observed for the L-A case. However, here there is no clear preferential excitement of the subharmonic modes, and the fundamental modes increase at about the same rate as the subharmonic modes leading to the presence of detuned (mixed) modes for $0 \leq x \leq 35$. In addition, the magnitude of energy in the three-dimensional modes has grown approximately $O(10^3)$, i.e. much more rapidly than the L-A case, although the two-dimensional amplitude A_{2D} is only a factor of two larger. This observation is similar to that of Kim and Moser (1989), that is, once the primary mode reaches a certain "threshold" amplitude, rapid growth in the three-dimensional modes is excited.

Despite the presence of mixed modes at higher two-dimensional amplitudes, the H-type modes still dominate throughout the flowfield, in contrast to the experimental observations of Nishioka et al. (1975) where fundamental modes have higher amplitude. This discrepancy has also been observed in the temporal simulations of Singer et al. (1989), which they attributed to the presence of streamwise vorticity in the experiments of Nishioka et al. (1975). That is, in temporal simulations where H-type modes were found to dominate, introduction of streamwise vortices in the initial conditions yielded K-type dominated modes.

It is important to note that the three-dimensional random disturbances imposed at the inflow for the present simulations follow closely the initial conditions imposed by Kim and Moser (1989), where no coherent streamwise vorticity is initially present. However, the natural evolution of secondary instability in Kim and Moser (1989) yielded K-type dominated modes for low-amplitudes, where the present work yields H-type modes. Kim and Moser (1989) assert that in a transition

experiment where a two-dimensional wave is introduced (e.g. a vibrating magnetic ribbon) in the presence of rather small spanwise distortions in the mean flow, K-type modes should dominate whereas the theory would predict H-type modes. In the present work, the small spanwise distortions in the mean flow, caused by the random disturbance field at the inflow, do not induce a K-type secondary instability.

However, in Kim and Moser (1989), all of the Fourier modes were initially forced at the same amplitudes, whereas in the present study the two-dimensional mode is forced at a higher amplitude than the spanwise modes (See figure 4.3). This may provide an explanation for why Singer et al. (1989) and the present work did not display K-type dominance for low-amplitudes where Kim and Moser (1989) show the opposite, and that coherent streamwise vorticity must be the catalyst for K-type breakdown in the presence of two-dimensional forcing. However, for “natural” transition where a wave packet containing a continuous spectrum of all Fourier modes is introduced, the natural evolution of the initially low-amplitude disturbances should exhibit K-type secondary instability once the primary mode reaches a threshold amplitude (Kim and Moser, 1989).

4.1.4 Flow visualization using Lagrangian Coherent Structures

Lagrangian Coherent Structures (LCS) are defined as ridges in forward finite time Lyapunov exponent (FTLE) fields. LCS represent barriers to transport (Shadden, Lekien, and Marsden, 2005) and can be used to identify vortex boundaries for a visual characterization of the flow field. While LCS have been used as a visualization tool in a variety of flow-fields (Voth, Haller, and Gollub, 2002; Shadden, Lekien, Paduan, Chave, and Marsden, 2009; Lipinski and Mohseni, 2010), they have not been deployed to identify the coherent structures characteristic of the early stages of transition (Λ vortices) reported in numerous experimental (Klebanoff et al., 1962; Kruse and Wagner, 1998) and numerical (Singer et al., 1989; Zang and Krist, 1989; Saiki et al., 1993) studies. In the present work, we have implemented this method for the high-amplitude case to visualize the coherent structures present in secondary instability during laminar-turbulent transition.

In a transition simulation it is possible to trace vortex lines or plot isocontours of vorticity to

visually characterize the Λ vortices present in a secondary instability transition study. Generation of vortex lines, in particular, are sensitive to their spanwise placement of origin. LCS obtained from FTLE fields, in contrast, do not rely on the direct calculation of vorticity from discrete velocity data. Instead, one can take an existing set of Eulerian discrete velocity fields (in both time and space) and advect particles in a Lagrangian fashion to generate the FTLE. The FTLE is rather insensitive to the accuracy of the velocity field data (Haller, 2002) which is an advantage for this particular simulation, due to the noisy inflow conditions which make traditional techniques less than ideal for observing coherent structures. However, the FTLE is sensitive to the integration time τ , and with proper adjustment, coherent structures may be observed regardless of the noise level in the data. The FTLE is defined as

$$\Phi_T^{T+\tau}(\mathbf{x}) = \mathbf{x}(T) + \int_T^{T+\tau} \mathbf{v}(\mathbf{x}(t))dt \quad (4.7a)$$

$$\Delta = \left(\frac{d\Phi}{d\mathbf{x}} \right) * \left(\frac{d\Phi}{d\mathbf{x}} \right) \quad (4.7b)$$

$$\sigma_T^\tau(\mathbf{x}) = \frac{1}{\tau} \ln \sqrt{\gamma_{max}(\Delta)} \quad (4.7c)$$

where σ is the FTLE and $\gamma_{max}(\Delta)$ is the maximum eigenvalue of the Cauchy-Green deformation tensor Δ , which is calculated for each point based on the deformation of the tracer mesh Φ (Lipinski and Mohseni, 2010). Also, T represents the initial time the tracer particles are advected. Note that the direction of integration depends on the sign of τ and represents either a forward or backward FTLE when τ is positive or negative, respectively.

It is important to note that the generation of LCS can be a rather computationally demanding process, however recent developments in ridge-tracking algorithms (Lipinski and Mohseni, 2010) can alleviate this cost. Because FTLE fields define vortex boundaries (Shadden, Dabiri, and Marsden, 2006), they are ideally suited for use in the observation of Λ vortices in a direct numerical simulation. To this end, the integration time τ for the following LCS has been chosen such that

coherent structures can be delineated with sharp boundaries and compare favorably with previous visualizations.

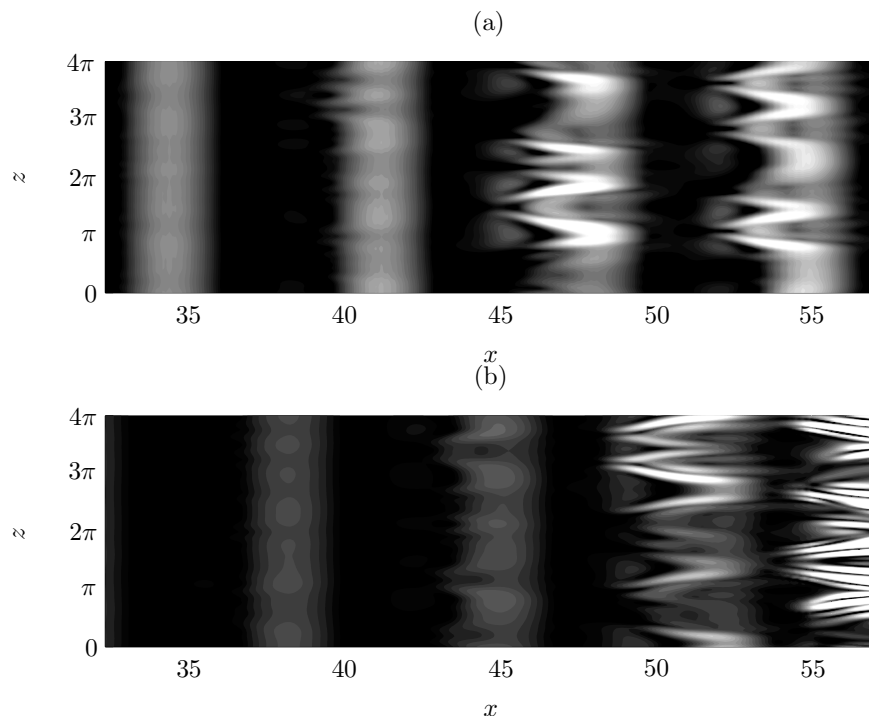


Figure 4.5: 2D forward FTLE fields in the critical layer $y \approx 1.88$ for the H-A case at (a) $T = 225.3$ (b) $T = 270.6$ for an integration time of $\tau = 0.357$

Forward FTLE fields for the H-A case computed on an x-y plane at the critical layer $y \approx 1.88$ (where the mean flow and disturbance phase velocity are equal) at $T = 225.3$ and $T = 270.6$ for an integration time of $\tau = 0.357$ are presented in figure 4.5. In figure 4.5(a), the two dimensional wave begins to break down into three-dimensional disturbances, and form clearly defined Λ vortices at $x \approx 45$, which form a mostly staggered pattern. This is indicative of an H-type instability (Herbert, 1983). The spanwise wavenumber of the Λ vortices varies between $2 \leq \beta \leq 3$ within $45 \leq x \leq 55$; these vortices stretch and distort as they convect downstream as shown at $T = 270.6$ in figure 4.5(b). Similarity of these structures to previous experimental (Kozlov and Ramazanov, 1983; Herbert, 1988) and computational (Zang and Krist, 1989; Saiki et al., 1993) visualizations of the Λ vortices is very strong, lending confidence to the LCS method to capture the characteristic

structures in secondary instability; where the integration time τ was selected to maximize the sharpness of the vortex boundaries.

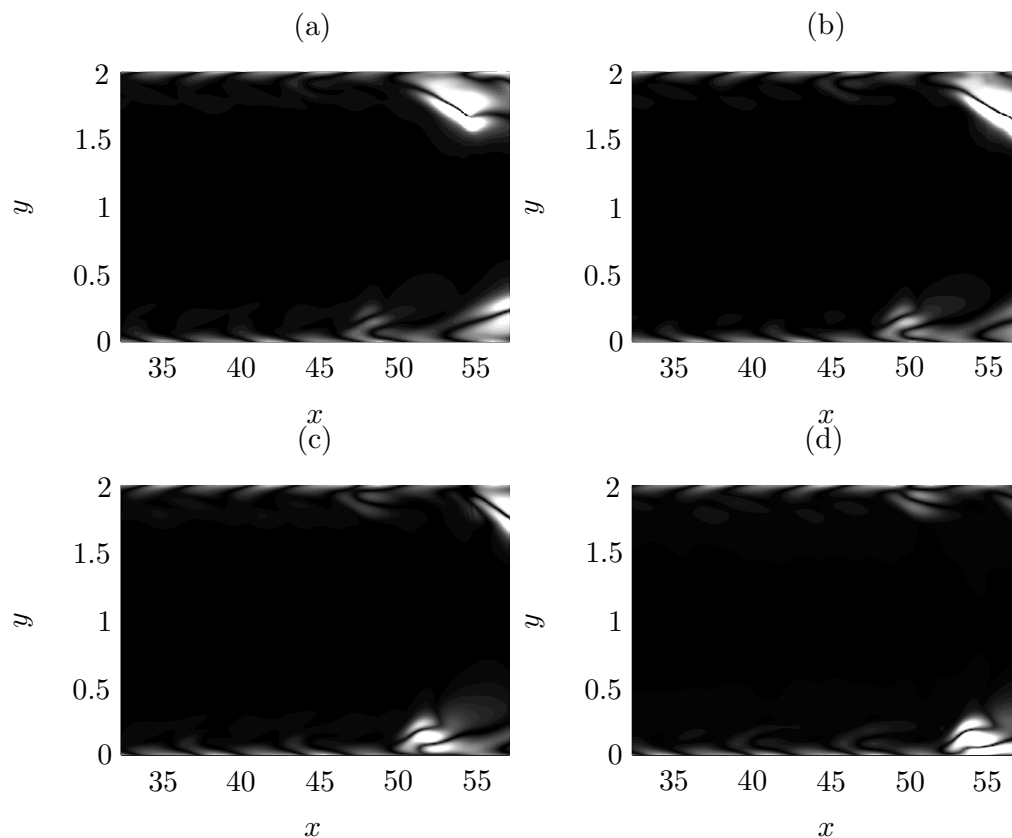


Figure 4.6: 2D forward FTLE fields at $z \approx 3.1$ for the H-A case at (a) $T = 248.1$ (b) $T = 253.8$ (c) $T = 262.4$ (d) $T = 272.4$ for an integration time of $\tau = 0.357$.

Forward FTLE fields in the x-y plane taken at $z \approx 3.1$ are presented in figure 4.6 from $T = 248.1 \rightarrow 272.4$ and captures two vortex lifting events (one at each wall). These events are quasi-periodic and occur in a staggered fashion at the top and bottom walls of the channel. That is, the vortex lifting events at each wall are 180° out of phase with the other as a characteristic of an H-type transition, where the high-shear layers localize and favor one wall (Herbert, 1983; Saiki et al., 1993).

FTLE fields in the y-z plane taken at various streamwise locations at $T = 272.4$ are presented in figure 4.7. The vortices favor either one wall or the other, depending on the streamwise location. It is not until $x \approx 57.1$ (figure 4.7(d)) that the vortices on the bottom wall begin to lift significantly

and form two distinct vortices with large three-dimensional distortions with a spanwise wavenumber of $\beta \approx 2\beta_r$. It is interesting to note that these vortices appear to be biased in the spanwise direction, where the highest vorticity occurs from $y = 0 \rightarrow 2\pi$. It is evident from figure 4.7 that the disturbances switch from showing H-type characteristics (biasing on one wall) to K-type characteristics (no biasing) when traveling downstream. This is consistent with the streamwise evolution of the perturbation kinetic energy shown in figure 4.3(b), where H-type disturbances dominate throughout the length of the channel, until the amplitudes of the K-type (fundamental) modes begin to approach that of the H-type near the end of the channel.

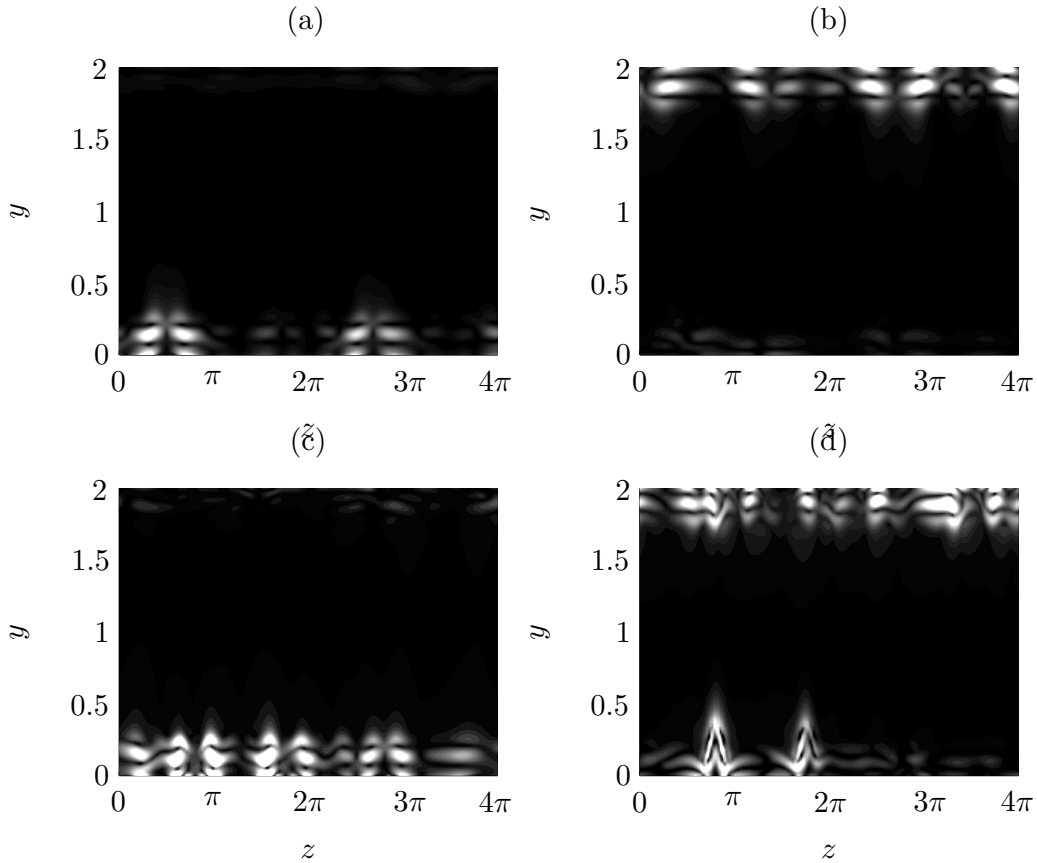


Figure 4.7: 3D forward FTLE fields in the y - z plane at $T = 272.4$ for the H-A case at (a) $x \approx 47.3$ (b) $x \approx 50.6$ (c) $x \approx 53.85$ (d) $x \approx 57.1$ for an integration time of $\tau = 0.357$.

4.1.5 Active Control of Transition

Active control using suction/blowing has been demonstrated to significantly reduce the amplitude of the primary TS wave, thereby delaying transition as the phase between the streamwise and wall-normal velocity component is destroyed (Biringen, 1984). Consequently, the perturbation field cannot transfer energy from the mean motion since the major production term in the turbulent energy equation, $\overline{u'v'}\partial U/\partial y$ is reduced (Biringen, 1984; Danabasoglu et al., 1991), where $\overline{(\)}$ denotes a time-average. In previous work regarding suction/blowing, the inflow conditions specified either H- or K-type secondary disturbances (Biringen, Nutt, and Caruso, 1987) or were explicitly two-dimensional (Erdmann et al., 2011). In the present case, the secondary instability is allowed to evolve naturally with no **a priori** assumptions on its structure. In this section we demonstrate the applicability of transition delay using suction/blowing to attenuate the primary mode, and consequently, the secondary modes in a simulated “natural” instability environment.

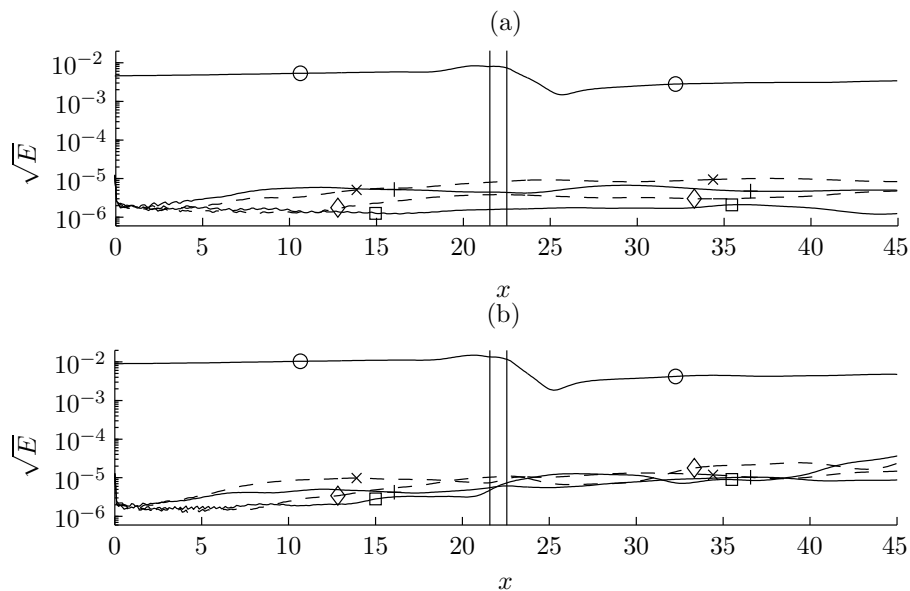


Figure 4.8: Streamwise evolution of integrated kinetic energy for specific modes for (a) case L-A, \circ : (1, 0), \diamond : (0.5, 1), \times : (0.5, 2.5), \square : (1, 1), $+$: (1, 2.5), (b) case H-A, \circ : (1, 0), \diamond : (0.5, 1.5), \times : (0.5, 4), \square : (1, 1.5), $+$: (1, 4). Solid lines represent fundamental modes while dashed lines represent subharmonic modes.

Active control of the L-A case was initiated using a spanwise homogeneous suction/blowing

slot located at $x_s = 21.58$ and $x_e = 22.77$. The amplitude of the control signal was set to $A_c = 5.69 \times 10^{-3} U_c$, and corresponds to the suggested value of Biringen (1984), where this amplitude (as the sum of both walls) must be about twice the amplitude of the wall-normal velocity component. The phase of the control wave for the L-A case was determined by trial and error until attenuation of the primary mode was observed. Evidence of transition delay for the L-A case is presented in figure 4.8(a), where the vertical lines denote the start ($x_s = 21.58$) and end ($x_e = 22.77$) of the suction/blowing slot with the streamwise length of this slot set approximately as 20% of the primary TS wave (Danabasoglu et al., 1991). There is a slight upstream influence of the suction/blowing slot with an increase in the total energy at the slot center, and then a rapid decrease in the total energy downstream of the slot owing to the destruction of phase between u' and v' . Further downstream of the slot, the two velocity components again become phase locked, which produces a linear increase in the total energy along the channel. This is in agreement with previous active control cases (Biringen, 1984; Danabasoglu et al., 1991) where after an initial adjustment, the energy in the flow would again increase linearly downstream of the suction/blowing slot. Near the end of the channel $x = 45$, there is a $\Delta E_{\%} = 57\%$ decrease in the primary (1,0) mode when compared to the uncontrolled L-A case (figure 4.3(a)). In addition, the amplitudes of the secondary modes are redistributed, with a more “mixed” secondary instability as indicated by the similar amplitudes of the subharmonic (dashed lines) and fundamental (solid lines) modes when compared to the overall higher H-type secondary mode observed without control in figure 4.3(a).

As mentioned earlier, the phase angle ϕ of the control signal was determined through trial and error, much like in Danabasoglu et al. (1991). However, by measuring the local wall pressure at some fixed location upstream of the suction/blowing slot, one can “tune” the phase angle such that the phase shift between the measured pressure signal and the control signal (ϕ_{shift}) will properly attenuate the TS wave. This is demonstrated for the L-A case in figure 4.9(a), where the wall pressure was sampled at a fixed location at $x = 18.77$. Note that at this particular location, the wall control signal is 180° out of phase with the wall pressure. We apply this same control strategy for the H-A case by measuring the pressure at this same location and ensuring the control signal

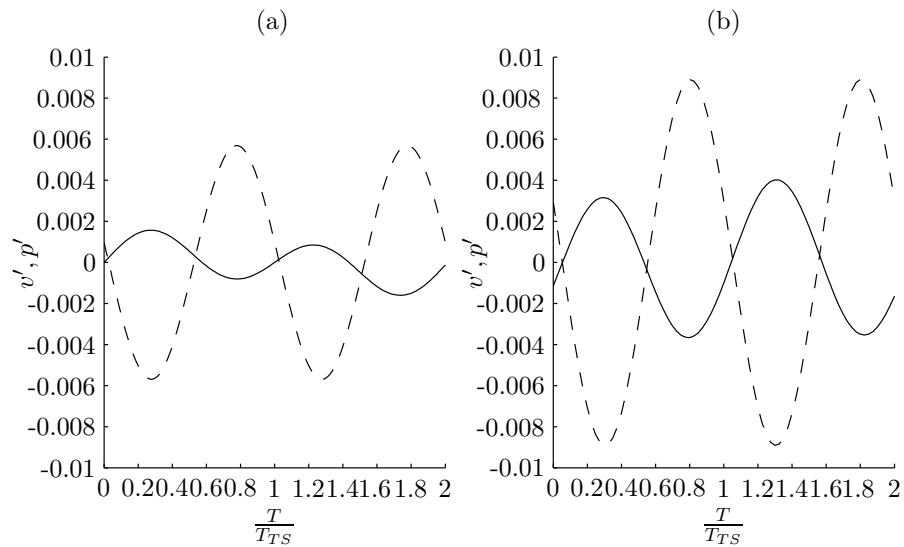


Figure 4.9: Wall-normal control signal measured at the suction/blowing slot and the wall pressure signal measured at $x = 18.77$ over two full TS periods for (a) L-A case, (b) H-A case; solid line: wall pressure signal, dashed line: suction/blowing control signal.

is 180° out of phase with this pressure signal, which is shown in figure 4.9(b).

The results of this control strategy for the H-A case, with the control amplitude $A_c = 8.92 \times 10^{-3} U_c$, is provided in figure 4.8(b) and shows similar attenuation of the primary mode from the suction/blowing slot as the L-A case. There is approximately a $\Delta E_{\%} = 72\%$ decrease in the primary $(1,0)$ mode when compared to the uncontrolled H-A case at $x = 45$. All of the secondary modes have also decreased significantly in amplitude when compared to the uncontrolled case (figure 4.3(b)), where a mixing of fundamental and subharmonic modes is present. Again, some distance away from the control slot the streamwise and wall-normal velocity components become phase locked and begin to transfer energy into the primary mode. This may be circumvented by arranging a series of these two-dimensional suction/blowing slots along the streamwise direction, with each slot tuned to the correct phase angle ϕ to attenuate the TS wave.

Temporally averaged shear stress distributions, spatially averaged over the channel width $\langle \overline{u'v'} \rangle$ are presented in figure 4.10 at $x = 45$. For both the L-A and H-A cases, the suction/blowing slot clearly shows a mitigation of the shear stress across the channel, most pronounced near the critical layer. These distributions are similar to that of Biringen et al. (1987); Danabasoglu et al.

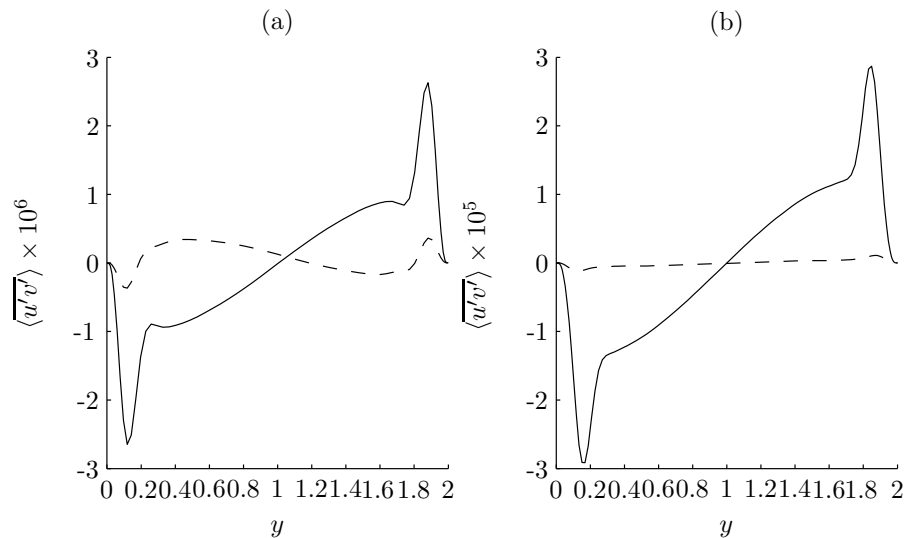


Figure 4.10: $\langle u'v' \rangle$ distributions for (a) Case L-A and (b) Case H-A; solid line: no control, dashed line: with control.

(1991), where large attenuation of the shear stress was observed. It is interesting to note that the control is less effective for low-amplitude disturbances compared to the high-amplitude case, where the phase angle between the pressure and wall signals (figure 4.9) for both cases were equal. In addition, the control amplitude A_c for both cases was set to equal that of the wall-centered uncontrolled velocity for each case, as suggested by Biringen (1984).

This may be attributed to the magnitude of the three-dimensional perturbation streamwise velocity u'_{3D} compared to the two-dimensional velocity u'_{2D} , which is represented by A_{3D} and A_{2D} in Table 4.1. At the inflow for the L-A case, the ratio u'_{2D}/u'_{3D} is twice that of the H-A case. This indicates that the optimum control amplitude may deviate from the wall-centered uncontrolled velocity when the three-dimensional component of the disturbances approach that of the two-dimensional components.

Spatial distributions of maximum root mean squared (RMS) streamwise and spanwise perturbation velocities, spatially averaged across the span of the channel, are given in figures 4.11 and 4.12 for the L-A and H-A cases, respectively. The edges of the suction/blowing slot are noted by straight vertical lines and $\langle \rangle$ denotes a spatial average in the spanwise direction. Observed is an upstream travelling wave due to the presence of the suction/blowing slot, which initially increases

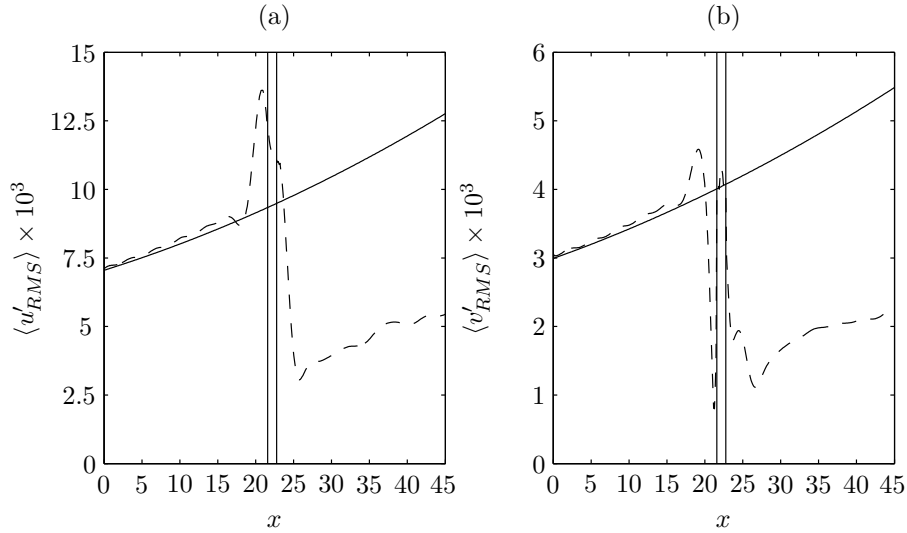


Figure 4.11: Case L-A streamwise evolution of (a) $\langle u'_{RMS} \rangle$ (b) $\langle v'_{RMS} \rangle$; solid line: no control, dashed line: with control.

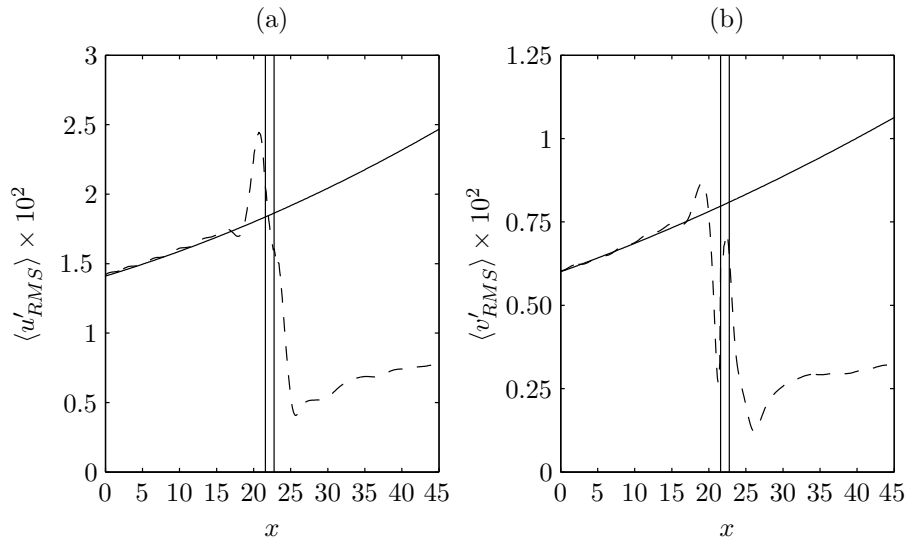


Figure 4.12: Case H-A streamwise evolution of (a) $\langle u'_{RMS} \rangle$ (b) $\langle v'_{RMS} \rangle$; solid line: no control, dashed line: with control.

the amplitude of $\langle u'_{RMS} \rangle$ and $\langle v'_{RMS} \rangle$ and decays rapidly as the wave propagates upstream, in accordance with the experimental observations of Ashpis and Reshotko (1990). Downstream of the slot, $\langle u'_{RMS} \rangle$ and $\langle v'_{RMS} \rangle$ for both cases show a substantial reduction in amplitude and then begin to grow again, albeit at a slower rate than for the cases without control.

In order for this control method to be applicable, the amount of energy supplied to the

| Case | A_{2D}/U_c | A_c/U_c | ϕ_{shift} | $\Delta E\%$ | E_D/E_S |
|------|--------------|-----------------------|-----------------------|--------------|-----------|
| L-A | 0.01 | 5.69×10^{-3} | 180° | 57 | 1.43 |
| H-A | 0.02 | 8.92×10^{-3} | 180° | 72 | 2.42 |

Table 4.2: Summary of control cases for $Re = 10,000$

actuating control slot must be lower than the energy saved using the control strategy. For a constant mass flow rate, any change in the wall shear stress, and consequently in the coefficient of drag, must manifest itself in a corresponding change in the pressure gradient (Chang et al., 2002). This metric is usually used in a fully turbulent flow, where the shear stress changes are large between control and no-control cases, and therefore the change in pressure gradients are also large. However, the current flow is transitional with the perturbations small compared to the mean flow, which implies very small changes in the pressure gradient. Because our aim is to delay transition with this control strategy, a better measure is the amount of decrease in the amplitude of the (1,0) mode in E (Eq. 4.20) for a controlled case compared to an uncontrolled case, averaged from the start of the control slot to the end of the physical domain, defined as

$$E_D = \frac{1}{(L_x - x_s)} \int_{x_s}^{L_x} (E^{nc} - E^{wc}) dx \quad (4.8)$$

where E^{nc} and E^{wc} are the vertically averaged kinetic energies (Eq. 4.20) of the (1,0) mode for the no-control (nc) and with-control (wc) cases. These modal distributions have already been presented in figures 4.3 and 4.9. The average energy that must be supplied to the control slot is given by

$$E_S = \lim_{T \rightarrow \infty} \frac{2}{T} \int_{t_0}^{t_0+T} (\mathbf{u} \cdot \mathbf{n})^2 dt \quad (4.9)$$

where \mathbf{u} is the control slot velocity and is given (Eq. 4.5) and \mathbf{n} is the outward unit normal from the control slot located at the channel walls. The factor of two accounts for the slot which is located at the top and bottom walls. The energy ratio of E_D to E_S then can be used as a measure for the efficiency of this control strategy. This ratio, as well as a summary of the flow control results are presented in Table 4.2.

The energy ratio for the L-A and H-A cases are 1.43 and 2.42, respectively. Because these quantities are greater than unity, the energy saved is greater than the energy expended actuating the control slot. Note that it was assumed that there were no losses from the actuators, so these are “ideal” quantities. It is interesting to also note that the efficiency of the L-A control is less than that of the H-A control, which may be explained by the non-optimal tuning of the amplitude A_c of the control slot for this case. In a real application, the control wave amplitude can be adjusted until an optimal reduction in the primary mode is achieved.

4.1.6 Conclusions

This paper (Kucala and Biringen, 2014) has presented the results of a spatially evolving plane-channel flow with a constant pressure gradient, subject to two-dimensional disturbances superimposed with random noise at the inflow. It was shown that for low amplitudes $A_{2D} = 0.01U_c$, the flow has a bias towards H-type modes with relatively modest growth in the secondary modes ($O(10^1)$), in agreement with the theory of Herbert (1983). For high amplitudes $A_{2D} = 0.02U_c$, initially there is biasing towards the H-type modes, with the K-type modal amplitudes approaching that of the H-type modes as the disturbances travel downstream. In addition, much larger growth in the secondary modes was observed in the H-A case, ($O(10^3)$) compared to the L-A case, despite the initial two-dimensional amplitude for the H-A case being only a factor of two larger. The present high-resolution spatial results verify and confirm previous periodic temporal numerical simulations (Singer et al., 1989). However, in contrast to the results of Kim and Moser (1989), K-type dominated transition was not observed for either the L-A or H-A case.

Forward FTLE fields were used to generate LCS to visualize characteristic Λ vortices as well as vortex lifting events commonly present in a secondary instability transition scenario. The LCS presented here shows qualitative agreement with previous experimental and computational visualizations, and represent a viable means of flow visualization in a transitional flow field.

Finally, it was shown that the control of the L-A and H-A cases was possible using a suction/blowing slot located at a fixed streamwise location and introducing a two-dimensional control

wave at the fundamental TS frequency. The phase of this control wave is determined by measuring the wall pressure at a fixed location upstream of the suction/blowing slot, where the signal is time-lagged with respect to the wall pressure signal. For this case, a substantial reduction in the integrated kinetic energy of the primary mode downstream of the slot was observed owing to the destruction of phase between the streamwise and wall-normal perturbation velocity components. The RMS distributions of streamwise and wall-normal velocity show large reductions in their amplitudes downstream of the control slot, effectively delaying transition when compared to the L-A case with no control. This method was also shown to be efficient, as the energy that must be supplied to the actuator of the suction/blowing slot is lower than the energy saved for both low and high amplitude three-dimensional disturbances.

4.1.7 Acknowledgements

This work was supported by NSF-IDR Award No. 1131802. Computational resources were provided by NSF on the Kraken supercomputer at the National Institute for Computational Sciences. Algorithms for generation of FLTE fields, along with helpful discussions were provided by Dr. Doug Lipinski. The authors thank the anonymous referees for their careful reading of the manuscript and their very helpful comments.

4.2 Control of Primary Instability Using a Phononic Subsurface

4.2.1 Introduction

The most understood path of transition is that of primary instability, which involves the growth of a two-dimensional, convective disturbance known as the Tollmien-Schlichting (TS) wave and is the primarily amplified wave when freestream disturbances are low, which is common in cruise flight conditions. These waves have characteristically low growth rates (in time or space) and are observed mostly in low disturbance environments (Klebanoff et al., 1962; Nishioka et al., 1975). Here, we consider a spatially evolving fluid flow influenced by a mean pressure gradient confined between two rigid walls, commonly referred to as Poiseuille flow, whose laminar solution yields a parabolic base flow. The linear stability of such a flow is governed by the linearized Navier-Stokes equation (Orr-Sommerfeld equation), which predicts the evolution of two-dimensional TS waves. These TS waves have been observed in laboratory experiments for boundary layers (Schubauer and Skramstad, 1948; Klebanoff et al., 1962) and channel flows (Nishioka et al., 1975), in which the predicted unstable waves were generated using a vibrating magnetic ribbon.

These two-dimensional disturbance waves can be controlled either through active or passive control methods. For an active control method, if the amplitude and phase information of a growing linear disturbance in the flow field is detected, a control system may be used to influence the disturbance wave either through direct wave cancellation or alteration of the base flow to reduce the amplitude of this disturbance (Gad-el Hak et al., 1998). Many studies concerning active control have been carried out in the literature, where the use of a suction/blowing slot (Biringen, 1984; Danabasoglu et al., 1991; Erdmann et al., 2011; Kucala and Biringen, 2014), surface heating and cooling (Liepmann and Nosenchuck, 1982), plate vibration (Gedney, 1983), and even Lorentz forcing (Albrecht, Aetzkes, Grundmann, Mutschke, and Gerbeth, 2008) can all be used to alter or cancel the unstable modes, thereby delaying transition. However, one must be careful to consider the amount of power that is required to reduce the amplitude of these waves, and if that power exceeds the savings of transition delay, then the control system is rather useless from an energy

savings standpoint. Also, active control requires the installation of complex hardware such as sensors, actuators, ducts, etc. which adds both excess weight and uncertainty into the control method.

A passive control method, however, would require no external work to actuate the control surfaces and therefore any energy savings obtained by this method of control operates at maximum efficiency. The use of compliant surfaces to delay transition has been investigated as a means to attenuate the TS wave in wall-bounded flows (Carpenter and Garrad, 1985; Davies and Carpenter, 1997; Carpenter, Lucey, and Davies, 2001). However, the relatively low elastic modulus used in these compliant surfaces can cause the surface to deform quite substantially and introduce undesirable unstable modes into the fluid/structure system (e.g. flutter) (Gad-el Hak, 2002). Also, a considerably high compliance is not welcome in an environment where this compliant panel must bear strong loads (housed on the surface of an aircraft wing, for example) and represents a significant drawback in realizing these compliant surfaces for a more realistic engineering application.

In this section, we demonstrate that the phonon motion governed by the design of a phononic crystal can either stabilize or destabilize the TS wave when a phononic subsurface (a periodic arrangement of different materials) replaces a portion of the bottom wall in Poiseuille channel flow[†]. In addition, we demonstrate that the subsurface does not introduce any significant undesirable modes into the flow field and that the surface deformations remain small, which suggests that the subsurface may be used as both a load bearing device as well as a transition-prevention mechanism in a variety of applications.

4.2.2 Methodology

4.2.2.1 Fluid Domain

The flow simulations are based on a Reynolds number $Re = 7,500$ and a non-dimensional frequency $\omega_r = 0.25$. This yields the least-damped eigenvalue of the Orr-Sommerfeld equation

[†]This work is done in collaboration with the group of Professor Mahmoud Hussein, AES Department. See Hussein, Biringer, Bilal, and Kucala (2015)

(Equation 1.2) $\alpha = 1.0004 - i0.0062$. This eigenvalue represents an unstable spatial mode with a growth rate of $-\alpha_I = 0.0062$. The disturbances are perturbed at the inflow through the following equation

$$\mathbf{u}'(x = 0, y, z, t) = A_{2D} \text{Real}[\mathbf{u}_{e2D}(y)e^{-i\omega_r t}] \quad (4.10)$$

where $A_{2D} = 0.01$ is the amplitude of the eigenfunction $\mathbf{u}_{e2D}(y)$ corresponding to ω_r and contains a streamwise and wall-normal perturbation component.

The TS frequency ω_{TS} in (Hz) is obtained by

$$\omega_{TS} = \frac{\omega_r U_c}{2\pi \delta}, \quad (4.11)$$

where either U_c or δ is prescribed for a given fluid viscosity ν and Re . We consider four cases of TS waves with different frequencies. All simulations are done for water with $\nu = 1 \times 10^{-6}$ m²/s and using $\delta = 4.2 \times 10^{-4}$ m. The centerline velocity for the primary simulation (Case B) is $U_c = 17.8$ m/s, which yields the dimensional frequency $\omega_{TS} = 1690$ Hz. The value of U_c is adjusted accordingly to obtain $\omega_{TS} = 1600$ Hz (Case A), $\omega_{TS} = 1700$ Hz (Case C) and $\omega_{TS} = 1800$ Hz (Case D), respectively. While the present analysis is based on water, the geometric scales and the physical fluid properties considered approximately correspond to a free stream velocity of 150 m/s in an air boundary layer developing on a wing of a typical airliner.

In all simulations, the dimensional fluid domain lengths were set as $L_x = 20\delta$, $L_y = 2\delta$, and $L_z = 2\pi\delta$ for the streamwise, wall-normal, and spanwise directions, respectively. The buffer domain length is approximately 30% of the total channel length, effectively preventing reflections at the outflow boundary. The computations were performed on the Kraken supercomputer at the National Institute for Computational Sciences using a $225(x) \times 65(y) \times 8(z)$ mesh in the entire domain availing 60 grid points per TS wavelength ($\lambda_x = 2\pi/\alpha_R$) in the streamwise direction. Also, the time step Δt was chosen such that there are 2000 time steps for every period of the TS wave. This spatial and temporal resolution is adequate in predicting the growth rates of unstable waves governed by the linear theory.

4.2.2.2 Coupled Simulation Geometry and Phononic Subsurface Design

The problem geometry is shown in figure 4.13(a), in which a portion of the bottom wall is replaced by a phononic subsurface spanning the bounds $x_s^* \leq x^* \leq x_e^*$ in the streamwise direction to assess the effect of a phononic subsurface to locally stabilize or destabilize the flow field in the presence of an unstable TS wave. In these bounds, a fluid/structure interaction problem (Section 2.3) is solved at every time step. The length of the phononic subsurface structure along the streamwise direction is chosen as $L_s = 1.6095\delta$ which corresponds to roughly one quarter wavelength of the primary disturbance wavelength λ_x .

For the results that follow, we design the phononic subsurface unit cell to exhibit a stop band over a frequency range encompassing the TS frequency ω_{TS} . The emerging unit cell consists of a layer of ABS polymer (90% volume fraction) and a layer of aluminum (10% volume fraction) and has a total length $L_{UC} = 40$ cm. The material property ratios are $\rho_{Al}/\rho_{ABS} = 2.6$, $E_{Al}/E_{ABS} = 28.7$, and $c_{Al}/c_{ABS} = 3.3$, where ρ is the material density, E is Young's modulus and c is the speed of sound in the material. The dispersive characteristics of a periodic composite is determined by the ratios of material properties, and not the absolute properties of the individual constituents. For completeness: the individual material properties are $\rho_{Al} = 2700$ Kg/m³, $\rho_{ABS} = 1040$ Kg/m³, $E_{Al} = 68.8$ GPa, $E_{ABS} = 2.4$ GPa, $c_{Al} = 5051$ m/s, and $c_{ABS} = 1519$ m/s.

The quantities in figures 4.13(a) and 4.13(b) are the dispersion characteristics and frequency response function (FRF), respectively. Shaded regions indicate a frequency range that prohibits elastic wave propagation where unshaded regions indicate frequency ranges in which the elastic waves are allowed to propagate in the direction of periodicity. Note that the FRF shown in figure 4.13(b) elucidates a truncation frequency in the stop band which provides a powerful resonance that can be utilized even if the structure is forced at a closely neighboring frequency.

The ‘‘phase indicator’’ is defined as the mean of the dot product between the forcing and displacement signals at the interface

$$\langle \phi(\omega^*) \rangle = \int_{t=0}^{t=t_T} \left[\frac{f(0,t)}{\bar{f}(0)} \cdot \frac{\eta(0,t)}{\max(\eta(0,t))} \right] dt, \quad (4.12)$$

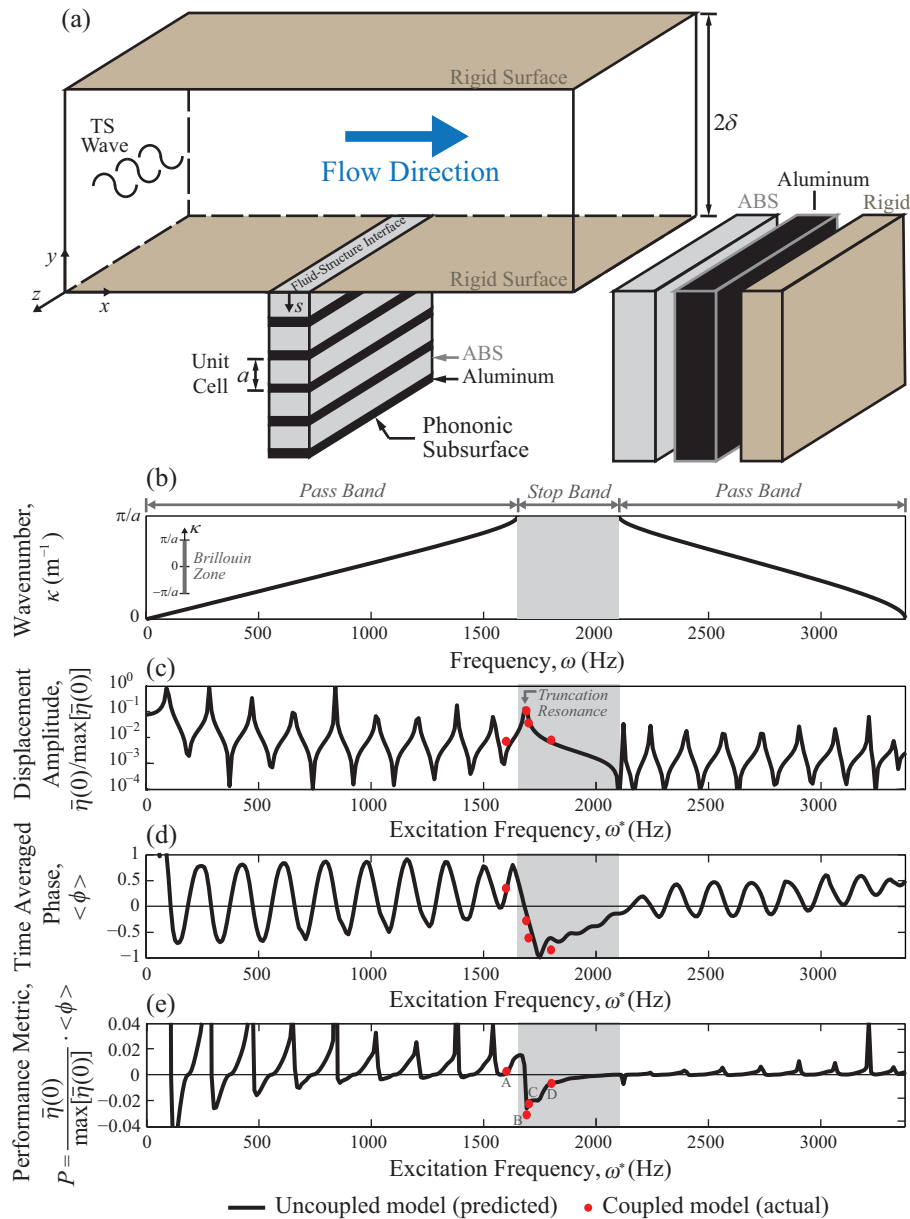


Figure 4.13: (a) Schematic of plane flow channel with phononic subsurface covering a segment in the range $x_s \leq x \leq x_e$, where $x_s = 2.926 \times 10^{-3}$ m and $x_e = 3.602 \times 10^{-3}$ m. For comparison, replacement with a rigid wall or other materials are also considered. (b) Dispersion curves for the 1D phononic crystal from which the subsurface is composed [Brillouin zone (Brillouin, 1946) illustrated in inset]. (c) Steady-state vibration response of phononic crystal top surface. (d) Time-averaged phase between force and displacement at the phononic crystal top surface. (e) Performance metric combining amplitude and relative phase between the force and the displacement at the phononic crystal top surface. Results from the coupled fluid-structure simulations are represented by red dots. In the coupled simulations, the phononic crystal top surface serves as the fluid-structure interface.

and is shown in figure 4.13(c). Here, the total integration time t_T is taken to be long such that $\langle \phi(\omega^*) \rangle$ is invariant with respect to this integration time. When $\langle \phi(\omega^*) \rangle$ is negative, the force and displacement signals at the interface are predominantly out of phase when the subsurface is forced at the specified frequency ω^* . The sign of this phase relation determines whether the subsurface is stabilizing or destabilizing to a TS wave forced at frequency ω_{TS} . Figure 4.13(e) plots the performance metric

$$P = \langle \phi \rangle \cdot \bar{\eta}(0) / \max [\bar{\eta}(0)] \quad (4.13)$$

and includes the amplitude and phase information as a function of ω^* . That is, the sign and magnitude of P will determine how strongly/weakly stabilizing/destabilizing a particular design is for a TS wave acting on the subsurface at a frequency ω_{TS} . Reductions in TS wave energy will be at a maximum when P is at a minimum (when ω_{TS} is near and to the right of the truncation frequency). The quantities in figures 4.13(b) and 4.13(c) are the dispersion characteristics and frequency response function (FRF), respectively. Details of how the dispersion relations and FRFs are obtained can be found in sections 2.2.1 and 2.2.2, respectively. The dispersion characteristics mainly govern the propagation or attenuation of elastic waves through the structure, while the FRF provides the amplitude information at a specific forcing frequency ω^* and is used in the calculation of P (Eq. 4.13)

4.2.3 Effect of the Subsurface on TS Waves

Here, we assess the effect of the phononic subsurface on the TS waves excited at $\omega_{TS} = 1600, 1690, 1700, 1800$ Hz (Cases A-D) to show how ϕ and P affect the stabilizing/destabilizing properties of the subsurface relative to ω^* . Time-histories of volume-integrated perturbation kinetic energy (PKE)

$$T_f^*(t^*) = \rho_f \int_0^{L_z} \int_0^\delta \int_0^{L_x} \frac{1}{2} (\hat{u}^{*2} + \hat{v}^{*2} + \hat{w}^{*2}) dx^* dy^* dz^*, \quad (4.14)$$

are shown in figure 4.14(a). In this equation, the vector $\mathbf{u} = (u, v, w)$ represents the velocity components in the streamwise, x , wall-normal, y , and the spanwise, z , directions, respectively, ρ_f

is the fluid density, L_x and L_y are the channel-base dimensions, and δ is the channel half-height. The symbols $\hat{()}$ and $(\cdot)^*$ are used to represent a fluctuating component of the velocity field and a dimensional quantity, respectively, for the detailed velocity decomposition formulation. The term $T_f^*(t^*)$ directly quantifies the instability wave kinetic energy in the bottom half of the channel as a function of dimensional time t^* . The volume of integration over the bottom half of the channel is bounded by its physical domain, that is, the buffer domain is excluded from the integration

Figure; 4.14(a) makes comparisons between a rigid wall, a phononic subsurface, an aluminum subsurface, and an ABS plastic subsurface when $\omega_{TS} = 1690$ Hz and falls to the right of the truncation frequency $\omega_{truncation} = 1683$ Hz. When the rigid wall is replaced by a phononic subsurface, there is a resonance between the TS wave and the truncation mode. The values of T_f^* oscillate around the rigid wall solution, where the aggregate PKE falls below the rigid wall PKE, indicating on average that the phononic subsurface is removing PKE from the flow. This is in contrast to the solution in which the rigid wall is replaced by either pure aluminum or pure ABS plastic subsurfaces, where small oscillations about the rigid wall solution occur and no discernible resonance is observed due to the lack of dispersion in these homogenous configurations.

Furthermore, when placing the TS frequency in a pass band ($\omega_{TS} = 1600$ Hz) the flow is destabilized by the introduction of the subsurface and is shown in figure 4.14(a), where T_f^* now oscillates around the rigid wall solution, and in the aggregate is predominantly greater than the rigid wall perturbation energy. This result can be inferred from the performance metric P first introduced in figure 4.13(d), in which $P > 0$ and therefore would have a destabilizing effect on the flow field. That is, the phase relationship between the force and displacement at the fluid/structure interface dictates that the energy transfer of PKE at the interface will be destabilizing to the TS wave.

The influence of the wall-normal component of velocity introduced at the fluid/structure interface can be assessed by examining the relative phase between the vertical perturbation velocity \hat{v}^* of a rigid wall solution to a phononic subsurface solution, where these phase relations are taken very near the fluid/structure interface ($y = 0.0108\delta$) and is shown in figure 4.14(c). Here, it can be

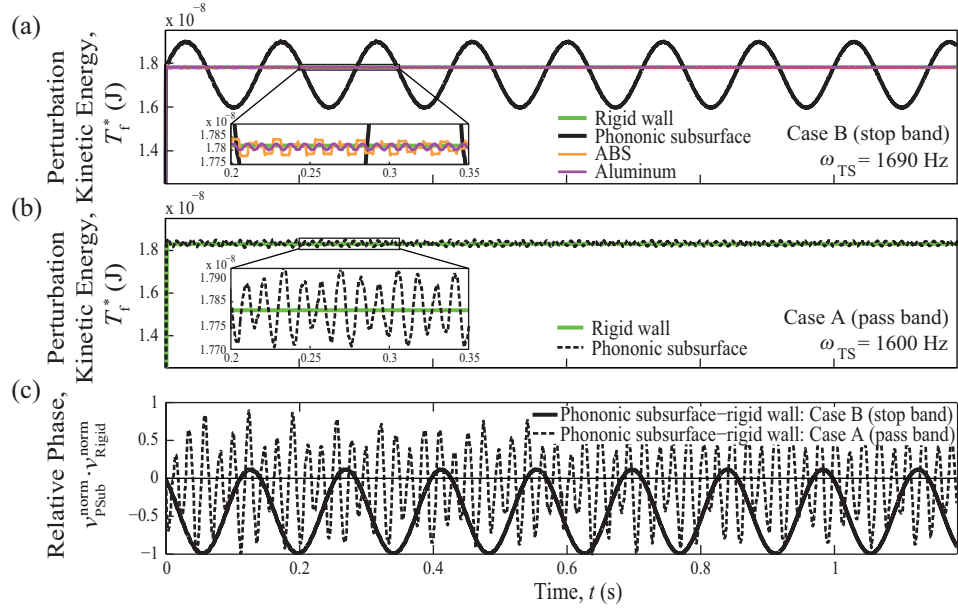


Figure 4.14: Time history of the kinetic energy of the disturbance field within the bottom half of the channel for (a) Case B ($\omega_{TS} = 1690$ Hz in a stop band) and (b) Case A ($\omega_{TS} = 1600$ Hz in a pass band). (c) Relative phase between flow vertical velocity at $(x, y, z) = ([x_s + x_e]/2, 0.0108\delta, z)$ when a phononic subsurface is installed compared to all-rigid walls (Rigid). Each velocity quantity is normalized with respect to its maximum value.

observed that when ω_{TS} is placed in a pass band, there is relatively little aggregate effect (because of the weakness of the chosen pass band frequency) on the phase relations compared to when ω_{TS} is placed in a stop band where P is at a local minimum. That is, when the subsurface is designed such that ω_{TS} is placed at a location in which P is at a local minimum, the phase relationship between the vertical velocity components is greatly altered in the flow field and greatly affects the rate of growth of PKE in the flow field.

The K_f^* is based on a time-area integration and is a function of the dimensional streamwise coordinate x^* . It is defined as

$$K_f^*(x^*) = \frac{\rho_f}{(t_{end}^* - t_{beg}^*)} \int_{t_{beg}^*}^{t_{end}^*} \int_0^{L_z} \int_0^\delta \frac{1}{2} (\hat{u}^{*2} + \hat{v}^{*2} + \hat{w}^{*2}) dy^* dz^* dt^*, \quad (4.15)$$

where t_{beg}^* denotes the beginning of the time-averaging window and t_{end}^* denotes the end of the time-averaging window. In our calculations, $t_{beg}^* = 0.03$ s and $t_{end}^* = 1.17$ s which represents a relatively long integration time (corresponding to approximately 1500 Tollmien-Schlichting wave

periods).

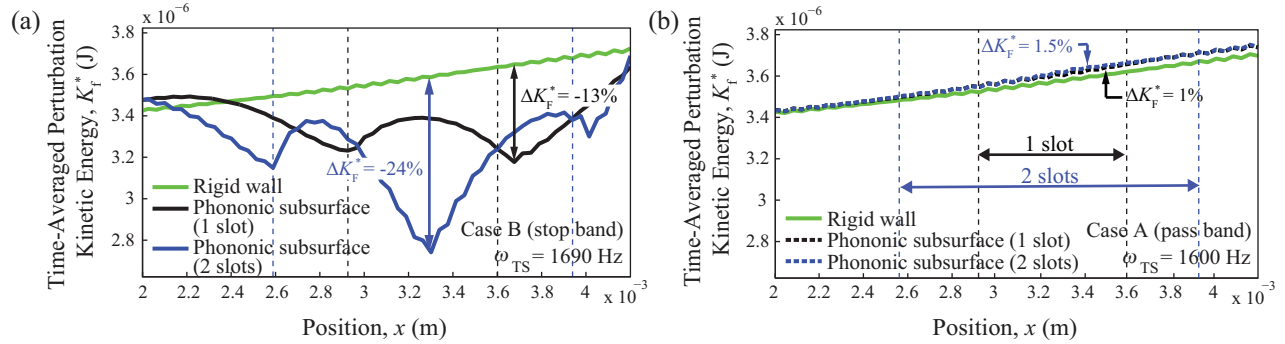


Figure 4.15: Streamwise spatial distribution of the time-averaged kinetic energy of the disturbance field within the bottom half of the channel for (a) Case B ($\omega_{TS} = 1690$ Hz in a stop band) and (b) Case A ($\omega_{TS} = 1600$ Hz in a pass band). The plotted quantity represents the spatial intensity of the flow instability.

Streamwise distributions of K_f^* for Case A and Case B are shown in figures 4.15(b) and 4.15(a), respectively. In this case, either one (black lines) or two (blue lines) subsurfaces may replace a portion of the rigid wall. If two subsurfaces are present, they are placed contiguously downstream of one another. For Case A, $\omega_{TS} = 1600$ Hz and lies in a pass band. As expected from the time-history of the perturbation energy shown in figure 4.14(b), the subsurface acts to weakly destabilize the flow field. This effect is compounded when two subsurfaces are utilized. For Case B, when the TS frequency $\omega_{TS} = 1690$ Hz and lies in a stop band where $P < 0$, a strong stabilizing effect of the phononic subsurface is evident, where a maximum percent difference in K_f^* is -13% and -24% for one and two subsurfaces, respectively. These streamwise distributions of perturbation energy for both cases show the remarkable predicative power of the uncoupled performance metric P and how it affects the flow field disturbances in the presence of a TS wave.

The fundamental mechanism that drives the dynamical phenomenon directly observed in figures 4.14 and 4.15 can be further elucidated by considering the equation for the perturbation

energy flux, written as

$$\frac{d}{dx} \left[\overbrace{\int_0^2 \frac{1}{2} u_b (\langle \hat{u}^2 \rangle + \langle \hat{v}^2 \rangle) dy}^{\text{I}} + \overbrace{\int_0^2 \langle \hat{u} \hat{p} \rangle dy}^{\text{II}} + \overbrace{\frac{1}{Re} \int_0^2 \langle \hat{v} \omega_z \rangle dy}^{\text{III}} \right] = \quad (4.16)$$

$$\underbrace{\int_0^2 -\langle \hat{u} \hat{v} \rangle \frac{du_b}{dy} dy}_{\text{i}} - \underbrace{\frac{1}{Re} \int_0^2 \langle \omega_z^2 \rangle dy}_{\text{ii}} - \underbrace{\langle \hat{v}_w \hat{p}_w \rangle}_{\text{iii}} + \underbrace{\frac{1}{Re} \langle \hat{u}_w \omega_{zw} \rangle}_{\text{iv}},$$

where ω_z denotes spanwise vorticity, “w” refers to a quantity evaluated at the wall, and $\langle \rangle$ expresses a time average. The symbol $(\cdot)_b$ is used to represent a base component of the velocity field. Following Ref. Davies and Carpenter (1997), the first two terms on the left-hand-side are grouped as the integrated mechanical energy flux. The most significant contributions to the energy budget are from the convection term (I) and flow work (II) which are balanced mainly by the kinetic energy production term (i) and, to a much lesser extent, by the irreversible pressure-work term (iii).

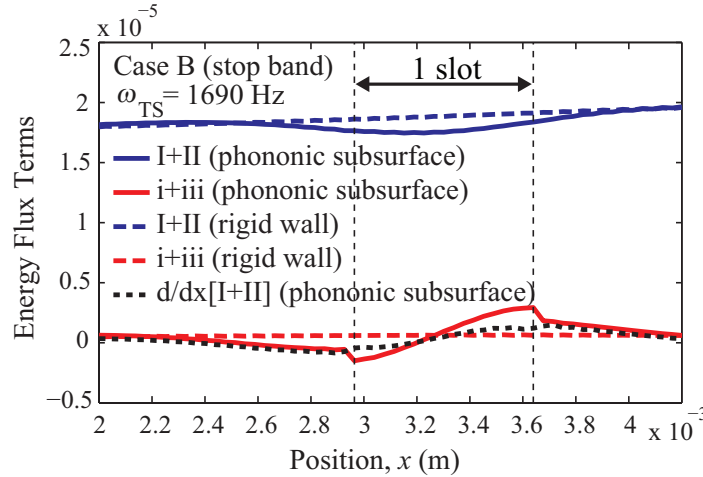


Figure 4.16: Decomposition of the perturbation energy flux in the fluid based on terms in Eq. 4.16.

In figure 4.16, we present the streamwise evolution of these quantities over the phononic subsurface obtained from the coupled simulations. From this figure, it is clear that there is a substantial decrease in the mechanical energy (terms I + II), with a maximum decrease of about 7%, compared to the all-rigid-wall arrangement; strong upstream and downstream effects are also evident. It is interesting to note that in figure 4.16 there is strong indication of reduction of mechanical energy,

but no discernible net decrease in the production term. However, a true comparison should be between the axial rate of change of the mechanical energy term (energy flux) and the production term as these are the actual terms that appear in Eq. 4.16. For the present simulation with the phononic subsurface, the mechanical energy flux term is indicated by the black dotted line in figure 4.16; it is apparent that this term follows the trend of the production term very faithfully, i.e. a negative region followed by a positive region such that the aggregate effect is approximately null flux, as opposed to the all-rigid-wall arrangement where the flux term (indicated by the slope of the dashed blue line) is always positive. Hence, the phononic subsurface instigates changes in the production term and reduces the disturbance kinetic energy by modifying its flux (as caused by changes in the relative phase of the \hat{u} and \hat{v} fluctuations).

Next, we consider the bottom-half integrated rate of production of perturbation energy, which is defined as

$$P_f^*(x^*) = \rho_f \int_0^{L_z} \int_0^\delta -\langle \hat{u}^* \hat{v}^* \rangle \frac{du_b^*}{dy^*} dy^* dz^*. \quad (4.17)$$

When this quantity, which has units of J/(m·s), is positive there is growth in the perturbation energy, and when it is negative, there is a decay. Consistent with all previous behavior, figure 4.17 shows negative values in the upstream region over the phononic subsurface for Case B, and, conversely, positive values for Case A (with increasing intensity when an additional segment is included). This lends further evidence to the impressive stop-band and pass-band wave interference behavior of the phononic subsurface.

A frequently used criterion to determine if a surface is hydraulically smooth is the roughness Reynolds number $Re_k = U_k k / \nu < 25$ where U_k is the local undisturbed velocity, k is height of the roughness element, and ν is the kinematic viscosity Morkovin (1990). Using this criterion, we find that the maximum displacement of the phononic subsurface $\eta(0)_{max} = 1.08 \times 10^{-6}$ m where $k = 1.54 \times 10^{-5}$ m. This is visually depicted in figure 4.18 where the actual wall displacements are well below the critical roughness height k . Also, the displacements are low relative to the inertial scales in the flow field, and validates the linearized fluid/structure coupling used in this study. The

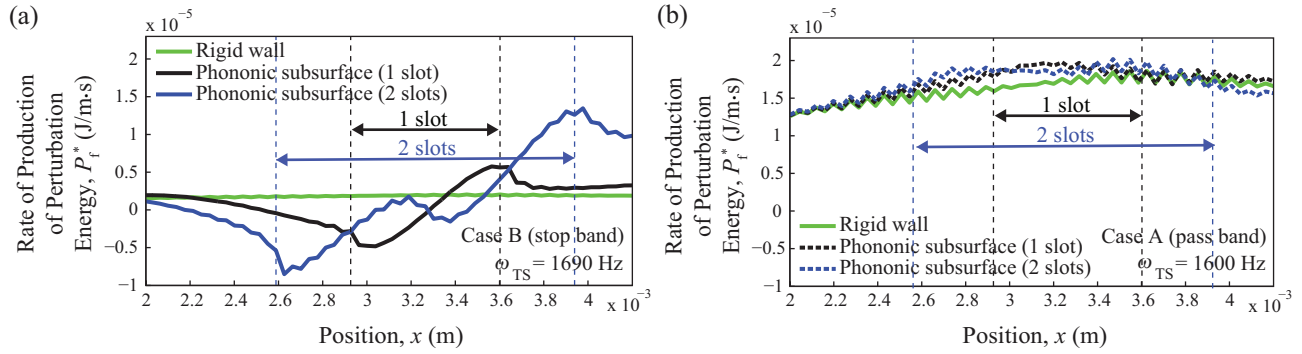


Figure 4.17: Perturbation energy production rate in the fluid for (a) Case B ($\omega_{TS} = 1690$ Hz in a stop band) and (b) Case A ($\omega_{TS} = 1600$ Hz in a pass band).

displacement of the phononic subsurface can therefore be considered sufficiently small and does not act as a surface roughness element, and therefore does not promote or enhance transition.

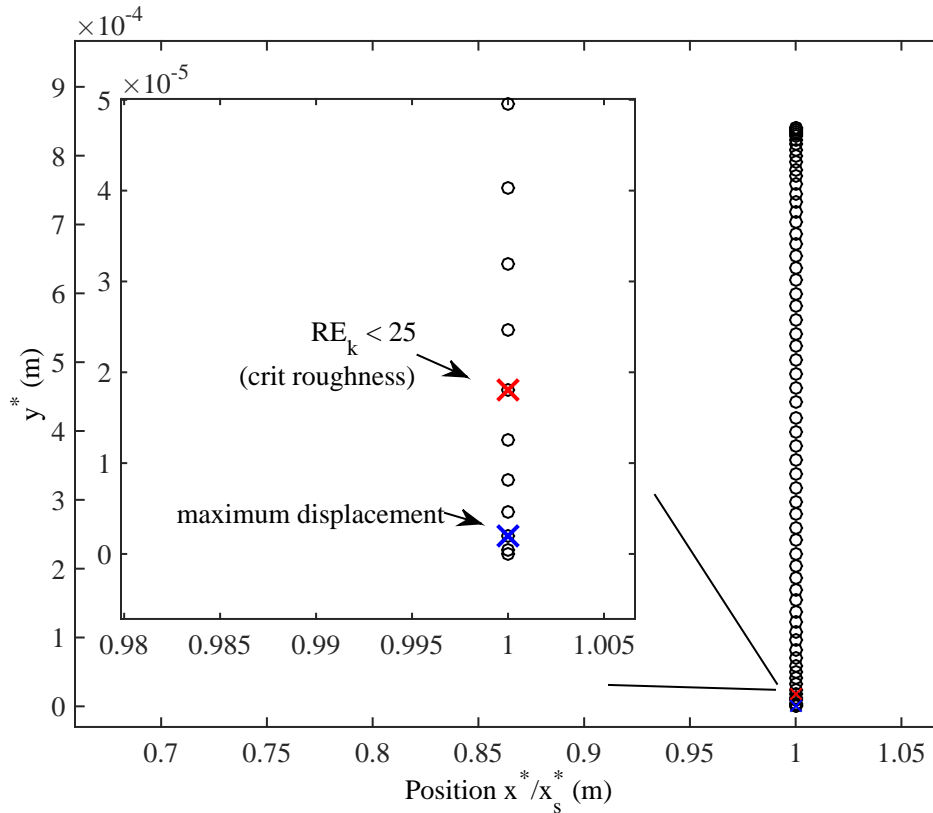


Figure 4.18: Maximum displacement $\eta(0)_{\max}$ for Case B relative to the maximum allowable surface roughness k on the wall-normal (y) grid. Circles represent the discrete grid points in y .

4.2.4 Phononic Subsurface Energetics

In this section, we analyze the time evolution and spatial distribution of the displacement field inside the phononic subsurface in the context of the coupled fluid-structure simulations described earlier. Out of the four cases of different TS frequencies considered in figure. 4.13, here we again focus on Case B and Case A.

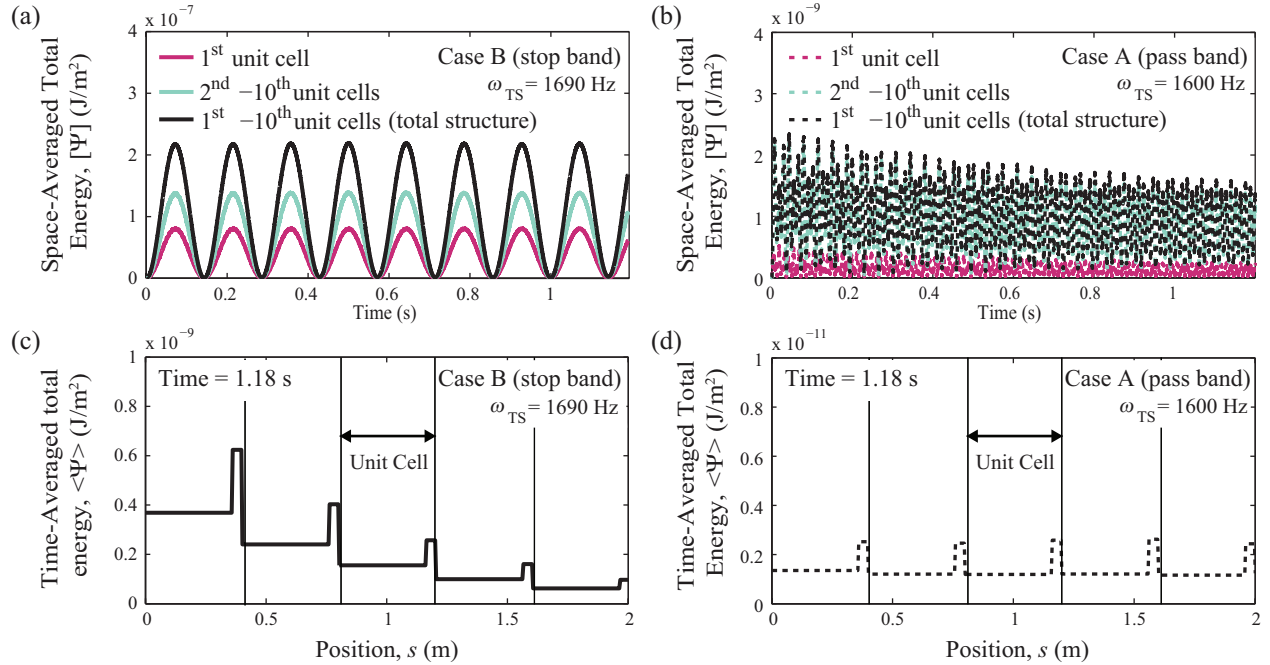


Figure 4.19: Average quantities of the total elastodynamic energy in the phononic subsurface for Case B ($\omega_{TS} = 1690$ Hz in a stop band) and Case A ($\omega_{TS} = 1600$ Hz in a pass band). The space-averaged total energy, $\{\Psi(\omega^*; s, t)\}$, is shown in (a) for Case B and in (b) for Case A. The time-averaged total energy, $\langle \Psi(\omega^*; s, t) \rangle$, is shown in (c) for Case B and in (d) for Case A. Information on how these average quantities are computed is provided in Appendix A. The energy inside the phononic subsurface displays a beat frequency of approximately 7 Hz. The unit cells are marked by vertical lines.

In figure 4.19, we show average quantities of the total energy in the phononic subsurface from the coupled simulations, defined as

$$\Psi(\omega^*; s, t) = \frac{1}{2} (E\eta^2 + \rho_s \eta^2) \quad (4.18)$$

From this quantity, a number of observations can be made. First, due to the stop band nature of Case B, the energetics in the structure decay as the elastic waves propagate down the length

of the structure in the periodic direction s (figure 4.19(c)). This is in contrast to the behavior of Case A, which exhibits pass band characteristics. That is, the disturbance energy is allowed to propagate through the structure. This confirms the stop/pass band behavior predicted in figure 4.13(a). Furthermore, as seen in figure 4.13(e), the value of the performance metric, both the predicted, P_P (black solid line), and the actual, P_A (red dots), indicate a near local minima for Case B and a low positive value for Case A. As such, it is expected for Case B to see large overall response at the interface between the fluid and the phononic subsurface, and in Case A a small overall response.

Figures 4.19(a) and 4.19(b) present a spatially-averaged total (kinetic and potential) energy for Case B and Case A, respectively, displaying oscillating patterns and a two-orders of magnitude larger overall response for Case B as anticipated by the performance metric P . Also noticeable is that in both cases the motion of the phononic subsurface, including the upper boundary which interfaces with the flow, is stable. That is, all temporal modes in the structure are stable with respect to time and do not interact with the flow field in any meaningful way.

For all of the results discussed previously, a minimal amount of damping was included into the model which suppressed the growth of the truncation frequency such that its amplitude did not exceed the amplitude of the TS waves. This is demonstrated in figure 4.20, where two frequencies are shown in the power spectra of wall displacement $\psi_{\eta(0)}$. The frequency to the right is the TS frequency $\omega_{TS} = 1690$ Hz and to the left is the truncation frequency $\omega_{Truncation} = 1683$ Hz. Here, the effect of damping is quite evident. In the case of no damping (figure 4.20(a)), the amplitude of the truncation frequency exceeds the TS frequency amplitude which causes the flow field to be destabilized in time. However, when a moderate amount of damping is introduced ($q = 6 \times 10^{-8}$) the truncation frequency is stabilized and its amplitude is slightly lower than that of the TS frequency which is shown in figure 4.20(b). Consequently, the volume integrated perturbation energy in the fluid T_f is now stable with respect to time and has an overall attenuating effect to the TS wave.

As shown previously, the performance metric P can be used to predict the amount of PKE reduction in the flow field compared to a rigid wall. Because P is a minimum near $\omega_{Truncation}$

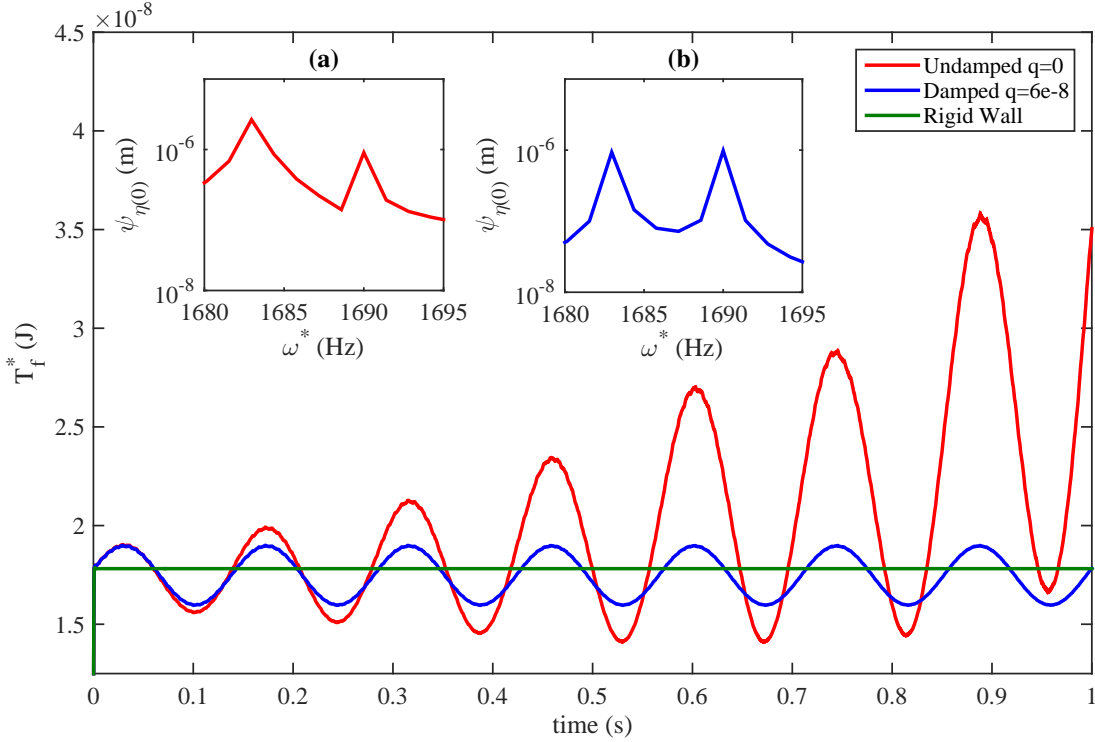


Figure 4.20: The effect of damping on flow energy T_f^* and power spectra of interface wall displacements $\psi_{\eta(0)}$ of Case B for (a) Undamped case ($q = 0$) and (b) Damped case ($q = 6 \times 10^{-8}$)

and is fixed for a given design, $(\Delta K_f)_{\max}$ can then also be quantified with respect to $\Delta\omega^* = (\omega_{\text{TS}} - \omega_{\text{Truncation}})$, and is summarized in table 4.3 for cases B-D.

| Case | $\Delta\omega^*$ (Hz) | $(\Delta K_f)_{\max}$ (%) | $\frac{\psi(\omega_{\text{truncation}})_{\eta(0)}}{\psi(\omega_{\text{TS}})_{\eta(0)}}$ |
|------|-----------------------|---------------------------|---|
| B | 7 | -13.0 | 0.95 |
| C | 17 | -6.5 | 0.78 |
| D | 117 | -0.6 | 0.04 |

Table 4.3: Summary of $(\Delta K_f)_{\max}$, $\Delta\omega^*$ and $\frac{\psi(\omega_{\text{TS}})_{\eta(0)}}{\psi(\omega_{\text{Truncation}})_{\eta(0)}}$ for cases B-D

The relationship between $(\Delta K_f)_{\max}$ and $\Delta\omega^*$ is useful as a first-order estimate as it only requires the knowledge of the frequency of the TS wave in the fluid and the truncation frequency

of the particular phononic subsurface design. This allows for the quick assessment of whether a particular subsurface will stabilize the TS wave and at what intensity, as the truncation frequency is a computationally inexpensive quantity to compute. This is in contrast to the computation of $\langle \phi(\omega^*) \rangle$ which requires the inversion of a large system of equations and is rather computationally demanding. Ideally it would be most beneficial to place the TS frequency as close as possible to the truncation.

However, one must be careful when placing the TS frequency close to the truncation frequency. Shown in table 4.3 and figure 4.20, as $\Delta\omega^*$ decreases, the ratio between the power spectra of surface displacement between the TS frequency and truncation frequency increases (for Case B the values of $\psi_{\eta(0)}$ are shown in figure 4.20(b)). As shown in figure 4.20, if $\psi(\omega_{\text{Truncation}})_{\eta(0)} > \psi(\omega_{\text{TS}})_{\eta(0)}$, T_f is unstable in time and therefore the effect of the subsurface is to destabilize the TS wave. Therefore, it is critical that this ratio between the displacement amplitude of the truncation frequency and TS wave does not exceed unity, otherwise the flow will be unstable (although this may be desirable in some applications). This ratio is therefore a function of the material damping and a function of $\Delta\omega^*$ within the vicinity of the truncation resonance.

4.2.5 Summary and Conclusions

Here we have demonstrated the applicability of a properly designed phononic subsurface to reduce the integrated PKE in a channel flow in which an unstable TS instability is present. The TS instability frequency is accommodated within a stop band for stabilization and within a pass band for further destabilization. The stabilization or destabilization of the TS wave occurs due to the wave-scattering interferences taking place within the periodic medium and is characterized through the phase relation between the interface forcing and displacement. With proper tuning of the phononic subsurface truncation frequency, the intensity of the fluid-structure interaction is also controlled.

Figure 4.21 shows that the predicted performance metric (which is obtained independently from the coupled fluid-structure simulations) correlates very nearly with the actual performance

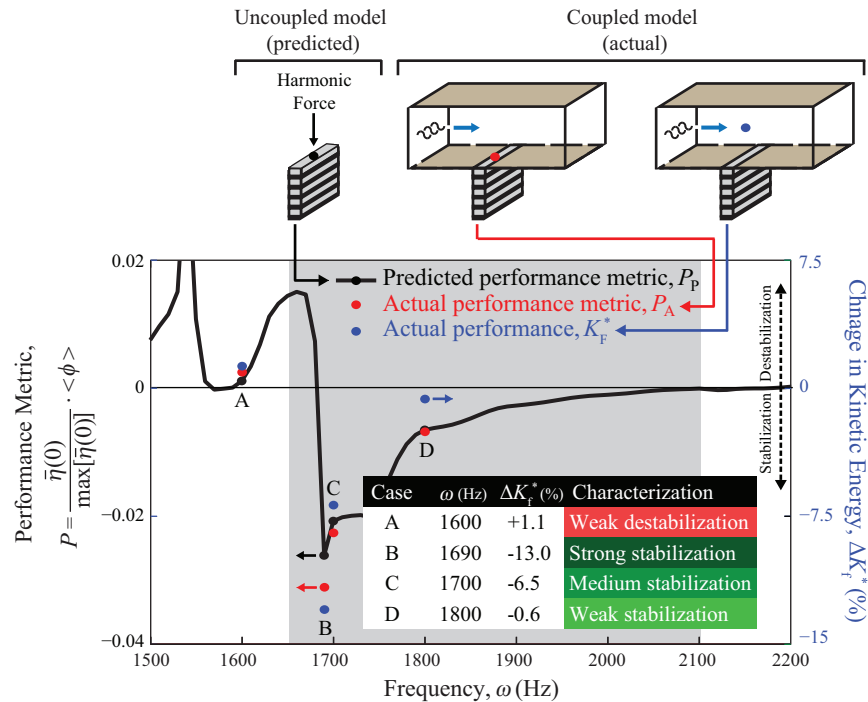


Figure 4.21: Predicted and actual performance metric (left ordinate) and actual change in flow disturbance kinetic energy (right ordinate) for Cases A-D. Grey region covers band gap of phononic-subsurface unit cell. Schematics above the chart refer to the computational domain considered for obtaining each quantity. A performance summary is provided in the inset.

metric including the actual change in the PKE, both as computed from the coupled simulations. This allows us to design a particular phononic subsurface without explicitly incorporating the unstable flow field, giving an unprecedented design methodology to finely tune the phononic subsurface depending on the application. Additionally, the approach does not depend on having a highly compliant or a highly damped surface, thus simultaneously maintaining surface stability while attenuating the unstable TS wave. While the current implementation utilizes a single- (or double-) phononic subsurface line segment, the dispersion characteristics of the control region act locally.

4.2.6 Acknowledgements

This research was funded by the National Science Foundation's Interdisciplinary Research program under grant number 1131802 and a CU-Boulder Innovation Seed Grant.

4.3 Phononic Subsurfaces for Multi-Frequency Instability Control

4.3.1 Introduction

Previously, we have demonstrated the ability of a phononic subsurface to reduce the amplitude of the primary mode in a channel undergoing transition when a single unstable TS wave is excited. In that study, it was shown that phonon motion underneath an elastic surface may be tuned to passively generate a spatiotemporal elastic deformation profile at the fluid/structure interface to reduce the mean perturbation kinetic energy in the flow field.

The mechanism for this reduction was identified as a frequency-dependent destructive interference of the disturbance wave occurring at the fluid/solid interface, governed by the frequency band structure intrinsic to a phononic crystal. The direction of wave propagation in the fluid domain and phononic subsurface are perpendicular, where the subsurface is composed of a periodic arrangement of phononic crystals and extends in the wall-normal direction (relative to the fluid, where wave propagation primarily occurs in the streamwise direction). This is in contrast to the previous work in compliant coatings (Carpenter and Garrad, 1985; Davies and Carpenter, 1997), where the wave propagation in both the fluid and elastic structure are both parallel and predominantly admits Rayleigh elastic waves along the surface (Gad-el Hak et al., 1998).

The study conducted in Section 4.2 concerned the attenuation of a single unstable TS wave artificially excited in the flow field. However, in a more natural transition environment, a range of unstable frequencies may be present in the flow field. In this case, it would be desirable to affect a range of frequencies that may be present in the flow for a given Reynolds number. That is, knowing the (approximate) Reynolds number of the flow, is it possible to design a phononic subsurface that can reduce the amplitude of a range of unstable modes, without introducing other undesirable modes into the flow field? Here, we will demonstrate the ability of a properly designed phononic subsurface to reduce the amplitude of a number of unstable modes that may be present in a low-disturbance environment transition scenario.

4.3.2 Methodology

The methodology for both the fluid and solid will follow closely to what was described in section 4.2 whereby a single unstable TS disturbance was introduced at the inflow. However, in this particular simulation, several TS modes may be excited at the inflow plane and be allowed to grow downstream. For completeness, the flow simulations presented here are based on a Reynolds number $Re = 7,500$. The coupled geometry is discussed in section 4.3.3.3.

4.3.3 Case Descriptions

4.3.3.1 Unstable Fluid Frequency Selection

The disturbances are introduced at the inflow using a linear superposition of modes that span a majority unstable range of frequencies for a fixed laminar Reynolds number. These disturbances are the eigenfunctions corresponding to the solution of the Orr-Sommerfeld equations, given previously in Eq. 4.4b. The unstable frequencies that are introduced at the inflow and their growth rates are summarized in table 4.4. These unstable frequencies were chosen such that they span the range of unstable frequencies in the flow field at a specific Reynolds number according to the solution of the Orr-Sommerfeld equation. For all the cases that follow, the Reynolds number $Re = 7,500$.

| ω^* [Hz] | ω_r | α_r | $-\alpha_i$ |
|-----------------|------------|------------|-------------|
| 1487 | 0.22 | 0.9167 | 0.003733 |
| 1690 | 0.25 | 1.0003 | 0.006168 |
| 1892 | 0.28 | 1.0828 | 0.001307 |

Table 4.4: Selected unstable frequencies for $Re = 7,500$

In table 4.4, the dimensional frequency ω^* is obtained as

$$\omega^* = \frac{\omega_r U_c}{2\pi \delta} \quad (4.19)$$

where either U_c or δ is prescribed for a given fluid viscosity ν and Re . For the present simulations, $U_c = 17.8$ m/s, $\delta = 4.2 \times 10^{-4}$ m, and $\nu = 1 \times 10^{-6}$ m²/s (water). These *real* frequencies will be

used to design a phononic subsurface which will mitigate a portion or all of the unstable frequencies in the flow field, depending on the design of a specific phononic subsurface.

4.3.3.2 Phononic Subsurface Design

The unit cells are composed of layers of Aluminum (Al) and Acrylonitrile butadiene styrene (ABL) plastic. The material property ratios are $\rho_{Al}/\rho_{ABS} = 2.6$, $E_{Al}/E_{ABS} = 28.7$, and $c_{Al}/c_{ABS} = 3.3$, where ρ is the material density, E is Young's modulus and c is the speed of sound in the material. The dispersive characteristics of a periodic composite is determined by the ratios of material properties, and not the absolute properties of the individual constituents. For completeness: the individual material properties are $\rho_{Al} = 2700 \text{ Kg/m}^3$, $\rho_{ABS} = 1040 \text{ Kg/m}^3$, $E_{Al} = 68.8 \text{ GPa}$, $E_{ABS} = 2.4 \text{ GPa}$, $c_{Al} = 5051 \text{ m/s}$, and $c_{ABS} = 1519 \text{ m/s}$. The unit cell length is 40 cm for both designs.

A viscoelastic damping model is used for the the material damping. This introduces an additional matrix (\mathbf{C}) in the system where $\mathbf{C} = p\mathbf{M} + q\mathbf{K}$, for stiffness proportional damping $p = 0$. The damping constants $q_{ABS} = 6 \times 10^{-8}$ and $q_{Al} = 0.1 \times q_{ABS}$. This translates into $\max(\zeta_2(\kappa)) = 0.06\%$, where $\max(\zeta_2(\kappa)) = \max(\frac{1}{2}q\omega(\kappa))$ is the maximum shift in the optical branch of the dispersion diagram due to the presence of damping.

Here, two different designs will be implemented. The band gap of the first subsurface (design A) will cover only half of the unstable frequency range, while the second subsurface (design B) will consist of a band gap which covers unstable fluid frequency range. These two designs are shown in figures 4.22 and 4.23 respectively, where the prescribed unstable fluid frequencies are indicated with shaded circles.

We will briefly describe each subplot in figure 4.22. The quantities in figures 4.22(a) and 4.22(b) are the dispersion characteristics and frequency response function (FRF), respectively. Details of how the dispersion relations and FRFs are obtained can be found in sections 2.2.1 and 2.2.2, respectively. Shaded regions indicate a frequency range that prohibits elastic wave propagation where unshaded regions indicate frequency ranges in which the elastic waves are allowed

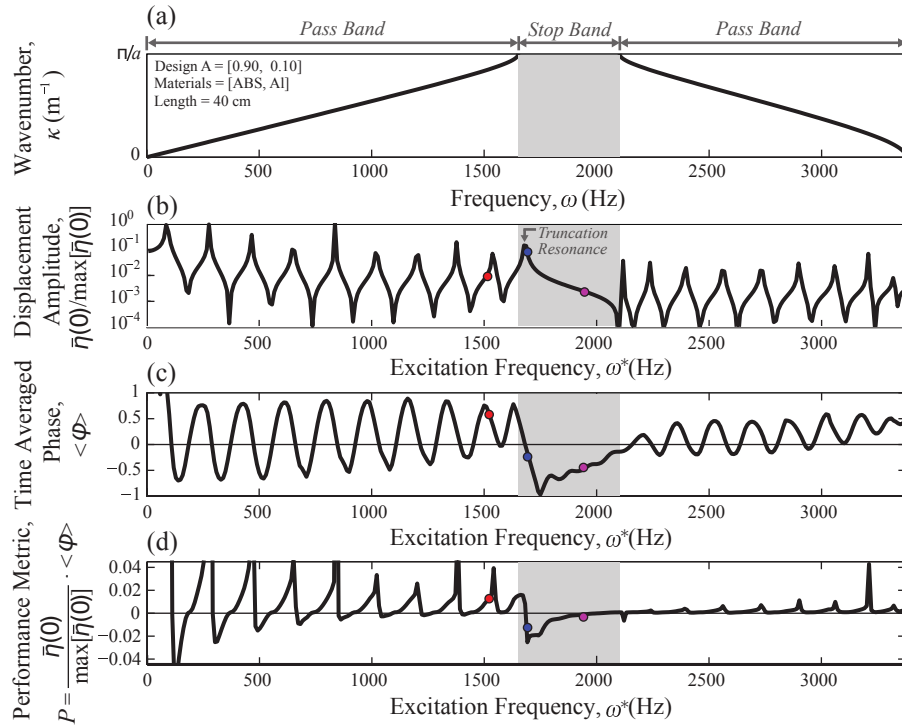


Figure 4.22: Phononic subsurface design A; (a) Dispersion curves for the 1D phononic crystal from which the subsurface is composed (material arrangements of the 1D periodic lattice is detailed on the inset). (b) Steady-state vibration response of phononic crystal top surface. (c) Time-averaged phase between force and displacement at the phononic crystal top surface. (d) Performance metric combining amplitude and relative phase between the force and the displacement at the phononic crystal top surface. Legend for dots is as follows: Red - 1487 Hz; Blue - 1690 Hz; Magenta - 1892 Hz

to propagate in the direction of periodicity. Note that the FRF shown in figures 4.22(a) and 4.23(a) elucidates a truncation frequency in the stop band which provides a powerful resonance when the structure is artificially forced with a closely neighboring frequency.

The “phase indicator” is defined as the mean of the dot product between the forcing and displacement signals (see Eq. 4.12) at the interface and is shown in figure 4.22(c). Here, the total integration time t_T is taken to be long such that $\langle \phi(\omega^*) \rangle$ is invariant with respect to this integration time. When $\langle \phi(\omega^*) \rangle$ is negative, the force and displacement signals at the interface are predominantly out of phase when the subsurface is forced at the specified frequency ω^* . The sign of this phase relation determines whether the subsurface is stabilizing or destabilizing to a TS wave forced at frequency ω^* (Hussein et al., 2015). Figure 4.22(d) describes the performance metric

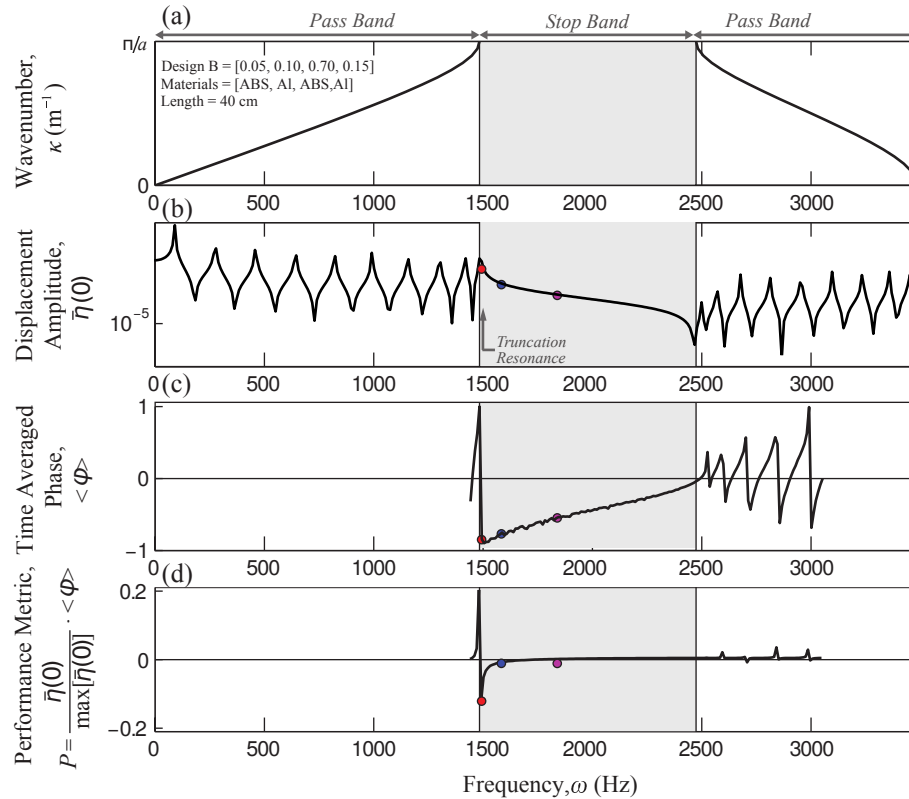


Figure 4.23: Phononic subsurface design B; (a) Dispersion curves for the 1D phononic crystal from which the subsurface is composed ((material arrangements of the 1D periodic lattice is detailed on the inset). (b) Steady-state vibration response of phononic crystal top surface. (c) Time-averaged phase between force and displacement at the phononic crystal top surface. (d) Performance metric combining amplitude and relative phase between the force and the displacement at the phononic crystal top surface. Legend for dots is as follows: Red - 1487 Hz; Blue - 1690 Hz; Magenta - 1892 Hz

P and includes the amplitude and phase information as a function of ω^* . That is, the sign and magnitude of P will determine how strongly/weakly stabilizing/destabilizing a particular design is for a TS wave acting on the subsurface at a frequency ω^* . Reductions in TS wave energy will be at a maximum when P is at a minimum (when ω^* is near and to the right of the truncation frequency). For a more thorough discussion of these plots, please refer to the discussion in Hussein et al. (2015).

4.3.3.3 Coupled Simulation Geometry

For the results that follow, the physical domain lengths in the fluid are $L_{x^*} = 5.04$ mm, $L_{y^*} = 0.840$ mm, $L_{z^*} = 2.6$ mm. The buffer domain extends from $5.04 \text{ mm} \leq x^* \leq 8.4$ mm and encompasses approximately 40% of the total channel length. The resolution for the rigid wall and control cases is $225 \times 8 \times 65$ in the streamwise (x), spanwise (z), and wall-normal (y) directions, respectively. Up to two phononic subsurfaces may be used to control the disturbance waves in the flow field for a selected case. The phononic subsurface is located on the lower wall at $y^* = 0$ and spans from a starting location x_{sk}^* and ending location x_{ek}^* where $k = 1, 2$ depending on the location of the phononic subsurface. For a subsurface at location 1, $x_{s1}^* = 2.93$ mm and $x_{e1}^* = 3.60$ mm. For a subsurface at location 2, $x_{s2}^* = 3.60$ mm and $x_{e2}^* = 4.27$ mm. In addition, the influence of the phononic subsurface is assumed constant along the spanwise spatial coordinate (z^*) due the invariance of the flow field in that direction. Inside these bounds, a fluid/structure interaction problem is solved at every time step (see Section 2.3), where streamwise and wall-normal velocity boundary conditions are imposed. Outside of these bounds, the wall is assumed rigid and the boundary conditions on the wall then are no-slip (see Eq. 2.15a, 2.15b). A summary of the cases considered can be found in table 4.5.

| Case | Subsurface 1 | $x_{s1}^* \rightarrow x_{e1}^*$ | Subsurface 2 | $x_{s2}^* \rightarrow x_{e2}^*$ |
|------|--------------|---------------------------------|--------------|---------------------------------|
| A | A | 2.93 mm \rightarrow 3.60 mm | N/A | N/A |
| A-A | A | 2.93 mm \rightarrow 3.60 mm | A | 3.60 mm \rightarrow 4.27 mm |
| B | B | 2.93 mm \rightarrow 3.60 mm | N/A | N/A |
| B-B | B | 2.93 mm \rightarrow 3.60 mm | B | 3.60 mm \rightarrow 4.27 mm |
| A-B | A | 2.93 mm \rightarrow 3.60 mm | B | 3.60 mm \rightarrow 4.27 mm |

Table 4.5: Case summary

4.3.4 Results and Discussion

4.3.4.1 Spectral Analysis

Spectra of vertically integrated perturbation kinetic energy per unit area in the fluid

$$E^*(x^*, \omega^*) = \rho_f \int_0^\delta (\hat{u}^{*2} + \hat{v}^{*2} + \hat{w}^{*2}) dy^* \quad (4.20)$$

is presented in figure 4.24(a) when phononic subsurface design A is used as the control material. Note that in this figure, the dashed line represents the rigid wall solution, and the solid line represents the solution where the phononic surface replaces a portion of the rigid wall. The vertical dashed lines indicate the upstream (x_{s1}) and downstream (x_{e1}) boundaries of the phononic subsurface. It is expected from figure 4.22(d) that any disturbance with a frequency falling to the left of the truncation frequency (1487 Hz) should increase in amplitude and that any disturbance frequency to the right of the truncation frequency (1690 Hz and 1892 Hz) should decrease in amplitude as the disturbances pass over the phononic subsurface.

This prediction is in agreement with the results shown in figure 4.24(a), where both the 1690 Hz and 1892 Hz disturbance frequencies experience a decrease in amplitude and the 1487 Hz disturbance frequency experiences an increase in amplitude. As mentioned earlier, the strength of the effect is dictated by the placement of these frequencies relative to the truncation frequency (figure 4.22(d)), where the modes closest to this frequency will experience the greatest attenuation (Hussein et al., 2015) when the performance metric P is at a minimum. Here we have demonstrated that the phononic subsurface acts in accordance with the predicted performance metric in the presence of multiple unstable excitation frequencies in the flow field. Is it possible, then, to design a phononic subsurface in which the range of unstable modes in the fluid may be known *a priori* and can all be stabilized?

Energy spectra in the flow field when phononic subsurface B is installed (Case B) is presented in figure 4.24(b). Here, the attenuation of the 1487 Hz mode is now strong, dictated by the design of subsurface B in which the performance metric P for this particular frequency lies near a minimum (figure 4.23(d)). Also, this particular design places the 1690 Hz and 1892 Hz modes to the right

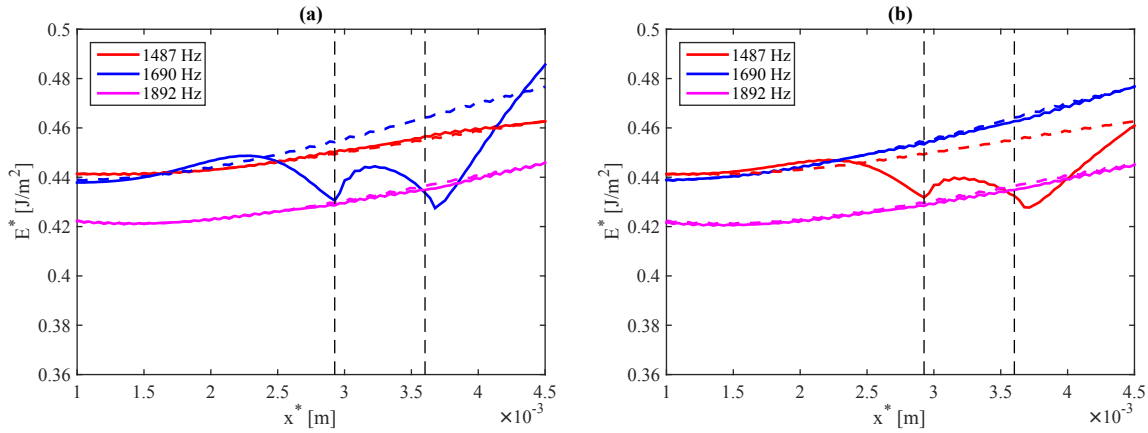


Figure 4.24: Vertically averaged kinetic energy spectra in the fluid for (a) Case A; (b) Case B. Dashed lines represent a rigid wall case where solid lines represent the control case. Vertically dashed lines indicate the upstream and downstream boundaries of the phononic subsurface.

of the truncation frequency, in which the performance metric P is negative, although lower in magnitude than the 1487 Hz mode. This causes those modes to be weakly stabilized in the presence of the phononic subsurface, and thus any unstable fluid mode predicted by the Orr-Sommerfeld equation can be positively affected (either strongly or weakly). This is a powerful demonstration of the localized beneficial effect of a properly designed phononic subsurface where a range of unstable frequencies can be attenuated.

Looking closely at the spectra in figure 4.24(a) for Case A, there is a large upstream influence of the subsurface where a significant decrease in the amplitude of 1690 Hz mode is observed. Also, there is rather large growth in the amplitude of this mode downstream of the trailing edge of the phononic subsurface. We can exploit this upstream influence by placing another phononic subsurface of the same design directly downstream of the first phononic subsurface in an effort to maintain the attenuation of the unstable modes over a longer distance. The results of such a configuration is shown in figure 4.25(a) for case A-A, figure 4.25(b) for case B-B.

For these two cases, the upstream influence of the phononic subsurfaces can be compounded to greatly increase the amplitude reductions in the attenuated modes. Due to the compounding nature of these consecutive subsurfaces, it may be possible to arrange these subsurfaces in series where

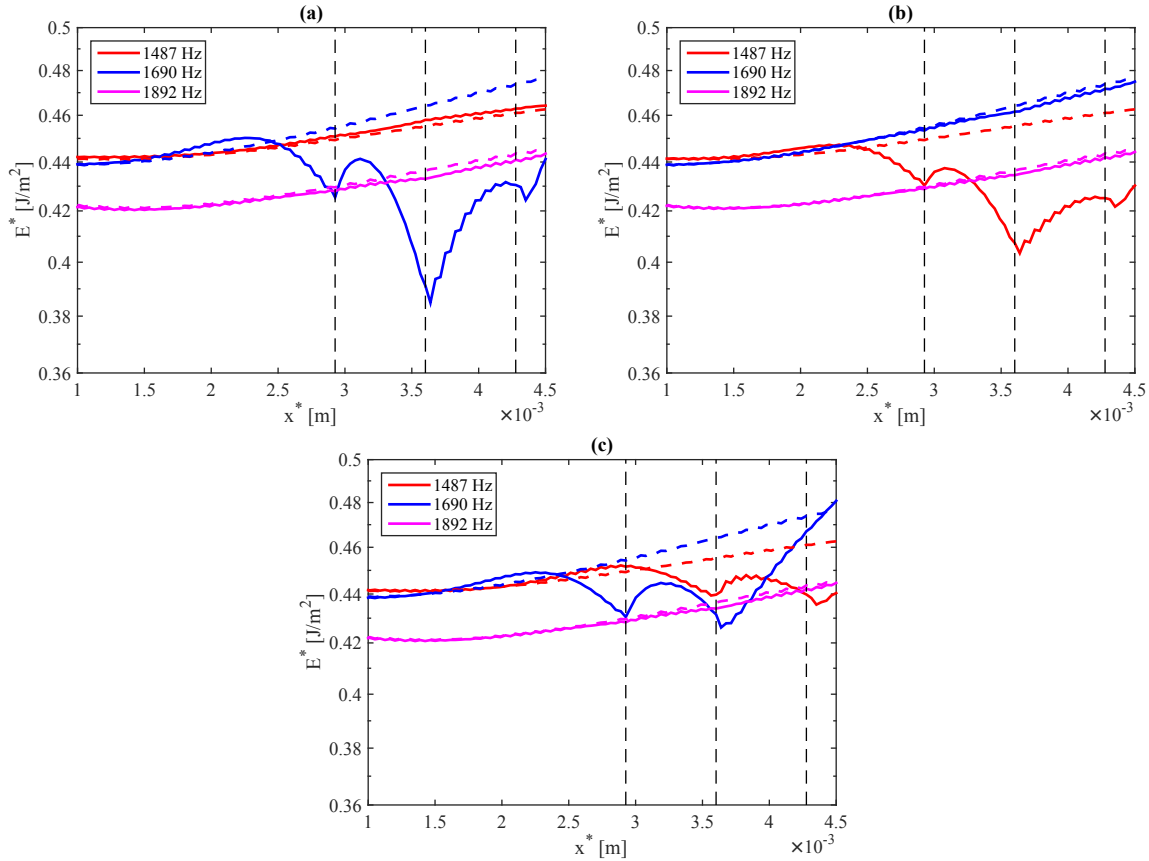


Figure 4.25: Vertically averaged kinetic energy spectra in the fluid for multiple subsurfaces (a) Case A-A; (b) Case B-B; (c) Case A-B. Dashed lines represent a rigid wall case where solid lines represent the control case. Vertically dashed lines indicate the upstream and downstream boundaries of the phononic subsurface.

the unstable fluid modes can be attenuated indefinitely downstream, thereby delaying transition and denying the development of secondary instability, a precursor to turbulence in low disturbance environments.

Another configuration is shown in 4.25(c) (Case A-B), in which the two subsurfaces of different designs (design A and design B) are placed contiguously downstream of one another. Here, the localized effect of each phononic subsurface design is highlighted. As the disturbance passes over the first subsurface (design A), the 1690 Hz mode is strongly attenuated and the 1892 Hz mode is weakly attenuated, as expected. However, in contrast to figure 4.25(a), the 1487 Hz mode is

actually attenuated over the first subsurface (design A) due to the strong upstream effect of the second subsurface (design B).

As the disturbances pass over the second subsurface, a notable change in the performance of the 1690 Hz mode is observed. It is expected from the performance metric in figure 4.23(d) that this mode should be attenuated as it propagates over the second subsurface (design B). However, in this particular configuration the subsurface trend appears to be moving firmly in the destabilizing direction to the 1690 Hz mode. Examining figure 4.24(a), there is large downstream growth of the 1690 Hz mode as the disturbance propagates downstream of the trailing edge of the subsurface (x_{e1}^*). It would appear then, that this downstream growth can only be attenuated if a second subsurface of similar (or identical) design is placed immediately downstream of the first subsurface such that performance metric P is of similar magnitude for both designs (figure 4.25(a)). However, P for the second subsurface (design B) in figure 4.25(c) is much lower in magnitude than design A (owing to the placement of this mode relative to the truncation mode) and does not appear to have a strong enough influence on the 1690 Hz mode to prevent the large downstream growth. However, careful observation between the recovery of the 1690 Hz mode downstream of the first slot in figures 4.24(a) and 4.25(c) shows that the growth of this mode is slightly lower in the latter case due to the small attenuating influence of the second subsurface (design B).

| Case | 1487 Hz | 1690 Hz | 1892 Hz |
|------|---------|---------|---------|
| A | +0.1% | -7.1% | -0.3% |
| A-A | +0.5% | -17.1% | -0.8% |
| B | -6.2% | -0.4% | -0.3% |
| B-B | -11.4% | -0.6% | -0.5% |
| A-B | -5.6% | -8.2% | -0.6% |

Table 4.6: Maximum modal energy differences $\Delta E_{\%}^*$ for various cases

We have demonstrated that a phononic subsurface may attenuate multiple unstable excitations in such a way that all three modes interact independently and favorably with the structure such that the phase between pressure and velocity at the fluid/surface interface ensures the attenuation of these discrete unstable disturbance frequencies. A summary of the interaction of the

two designs with the various unstable modes is presented in table 4.6, where we use the maximum percent difference between rigid wall fluid energy and controlled fluid energy. This metric characterizes the effect of a particular arrangement of the phononic subsurfaces on each unstable fluid mode.

$$\Delta E_{\%}^* = \left(1 - \frac{E_{\text{control}}^*}{E_{\text{rigid}}^*} \right)_{\text{max}} \quad (4.21)$$

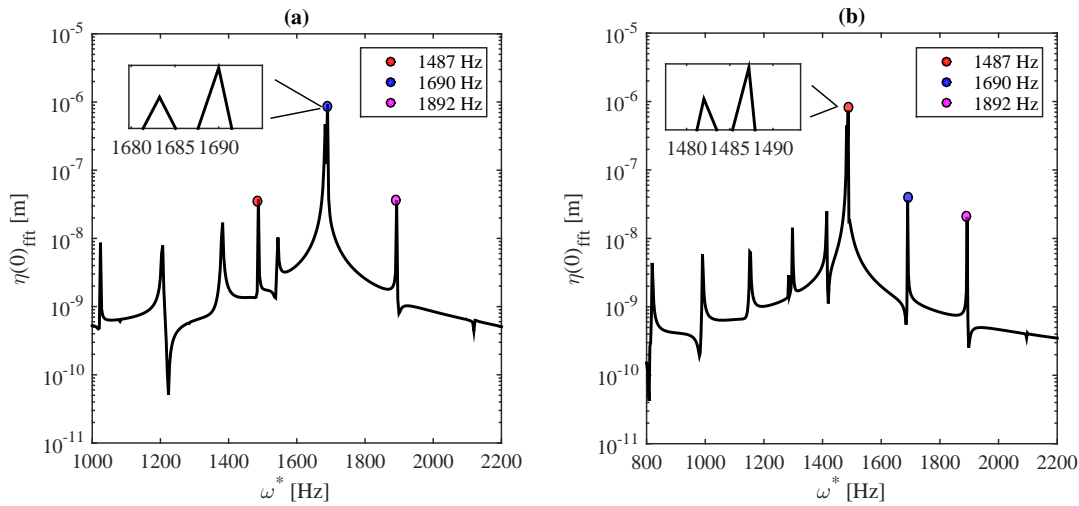


Figure 4.26: Spectra of phononic subsurface displacement at fluid/structure interface $\eta(0)$ for (a) Design A; (b) Design B.

Spectra of phononic subsurface displacement $\eta(0)$ at the fluid/structure interface is presented in figure 4.26, where a comparison of the relative amplitudes of displacement at the interface can be made for the each frequency. In figure 4.26(a), we show that for phononic subsurface A, the 1690 Hz mode has the highest displacement amplitude and falls to the right of the truncation frequency. Therefore, strong stabilization of this frequency is expected and correlates well with the maximum modal kinetic energy reductions $\Delta E_{\%}^*$ presented in table 4.6. In figure 4.26(b) for

phononic subsurface B, we show that all three frequencies fall in the attenuation range ($P < 0$) with the 1487 Hz mode having the highest displacement, owing to its close proximity to the truncation mode. The 1687 Hz and 1892 Hz modes have lower displacement amplitude and therefore have a relatively minor attenuating effect on the flow field, and corresponds to the values of $\Delta E_{\%}^*$ reported in table 4.6. The displacement spectra elucidates a number of natural modes that appear in the structure, and that their resulting displacements are much lower in amplitude than the modes excited by the TS waves. These modes then will have a relatively weak effect on the flow field dynamics and thus will not introduce any significant instabilities into the flow.

4.3.4.2 Time Averaged Kinetic Energy Analysis

The total reduction in the time averaged perturbation kinetic energy (PKE) K_f^* in the fluid is shown in figure 4.27 for all cases presented here. Here, $K_f^*(x^*)$ is a function of the dimensional streamwise coordinate x^* , t_0^* defines the beginning of the time-averaging window and t_f^* denotes the end of the time-averaging window. The time averaging window was taken when the PKE in the fluid domain exhibited a periodic steady-state such that the statistics were invariant of the time averaging window. Streamwise distributions of PKE are important as they contain all of the spectral characteristics in the fluid, and provides a measure of the contribution of spurious wall modes excited in the flow field due to the unique dispersion characteristics of the phononic subsurface.

In figure 4.27(a) and 4.27(b), we see the influence of the phononic subsurface on the mean PKE distributions compared to a rigid wall case. For these two figures, the effect of the phononic subsurface is compounded at the junction between the first and second subsurface, leading to a much larger maximum reduction in the PKE. In figure 4.27(a), we observe the high growth rates of the PKE downstream of the first subsurface for a single subsurface case (Case A), earlier attributed to the large downstream growth of the 1690 Hz mode. However, when a second subsurface is placed contiguously downstream (case A-A), the effect is somewhat mitigated and follows a similar trend to that of the 1690 Hz mode in figure 4.25(a). From these observations, we show that the phononic

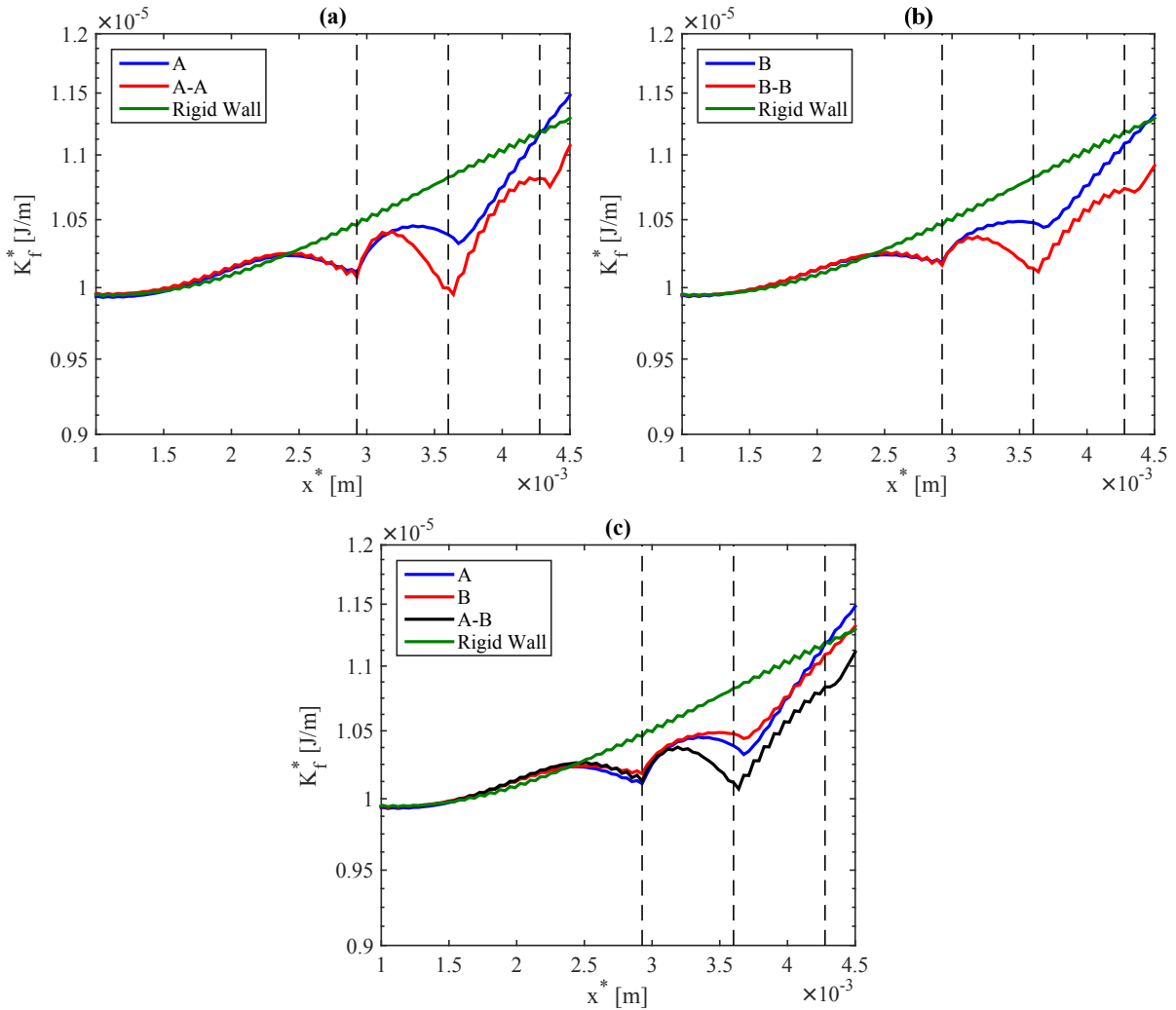


Figure 4.27: Time averaged perturbation kinetic energy in the fluid. Dashed lines indicate control using two phononic subsurfaces. Vertically dashed lines indicate the upstream and downstream boundaries of the phononic subsurface.

subsurface both lowers the overall PKE in the fluid locally across each subsurface, and that any spurious mode present at the fluid/structure interface does not have a substantial effect on the fluid PKE. That is, the subsurface primarily acts on the streamwise propagating TS modes to decrease the overall PKE in the flow field.

Figure 4.27(c) compares mean PKE distributions for cases A, B, and A-B. For case A, the 1690 Hz mode is attenuated strongly, while the 1487 Hz mode is attenuated strongly for case

B; shown earlier (figure 4.25). Now, both frequencies are able to be controlled, although when passing over the second slot, the 1690 Hz mode experiences downstream growth, although this growth rate is slightly less than if the second subsurface is replaced by a rigid wall, as mentioned earlier. This demonstrates the compounding effect of placing two distinct phononic subsurface designs contiguously downstream of one another and that case A-B out-performs case A and case B alone (see table 4.7). This lends us to believe that an array of subsurfaces of different designs can be placed contiguously downstream and may be able to attenuate a large range of continuous frequencies (say the frequencies present in a turbulent wall-bounded flow field). These designs can therefore reduce the perturbation energy in the fluid, effectively widening the strongly stabilizing frequency range of the phononic subsurface. This is a topic that warrants further investigation.

| Case | $(\Delta K_{f\%})_{\max}$ |
|------|---------------------------|
| A | -5.2% |
| A-A | -8.2% |
| B | -3.9% |
| B-B | -6.7% |
| A-B | -7.1% |

Table 4.7: Summary of maximum kinetic energy reductions $\Delta K_{f\%}$ for all cases

It should also be noted that for all cases, the PKE experiences large growth downstream of the second phononic subsurface. Looking closely at figures 4.27(a)(b) and comparing the values of $(\Delta K_{f\%})_{\max}$, this growth rate appears to be a function of the maximum PKE reduction. That is, the subsurface may act as a trampoline such that when there is less maximum reduction in PKE, the recovery of the flow back to a rigid wall state is slower. When designing an array of phononic subsurfaces, it would be beneficial to maximize the streamwise extent of reduced PKE compared to a rigid wall to sustain the effect of the phononic subsurface. Case B-B appears to be the case that satisfies this requirement, in which the PKE experiences the lowest growth rate downstream of the phononic subsurfaces, and also acts to suppress all unstable TS modes in the flow field (figure 4.25(b)) with longer streamwise extent.

4.3.4.3 Instantaneous Velocity Fields

The instantaneous streamwise perturbation velocity fields \hat{u} in the half-channel are presented in figure 4.28 for the cases A-A, B-B, and A-B. Here, the strength of the field is visualized by taking the absolute value of \hat{u} in order to assess the effect of the phononic subsurface on the instantaneous amplitude of the velocity fluctuations.

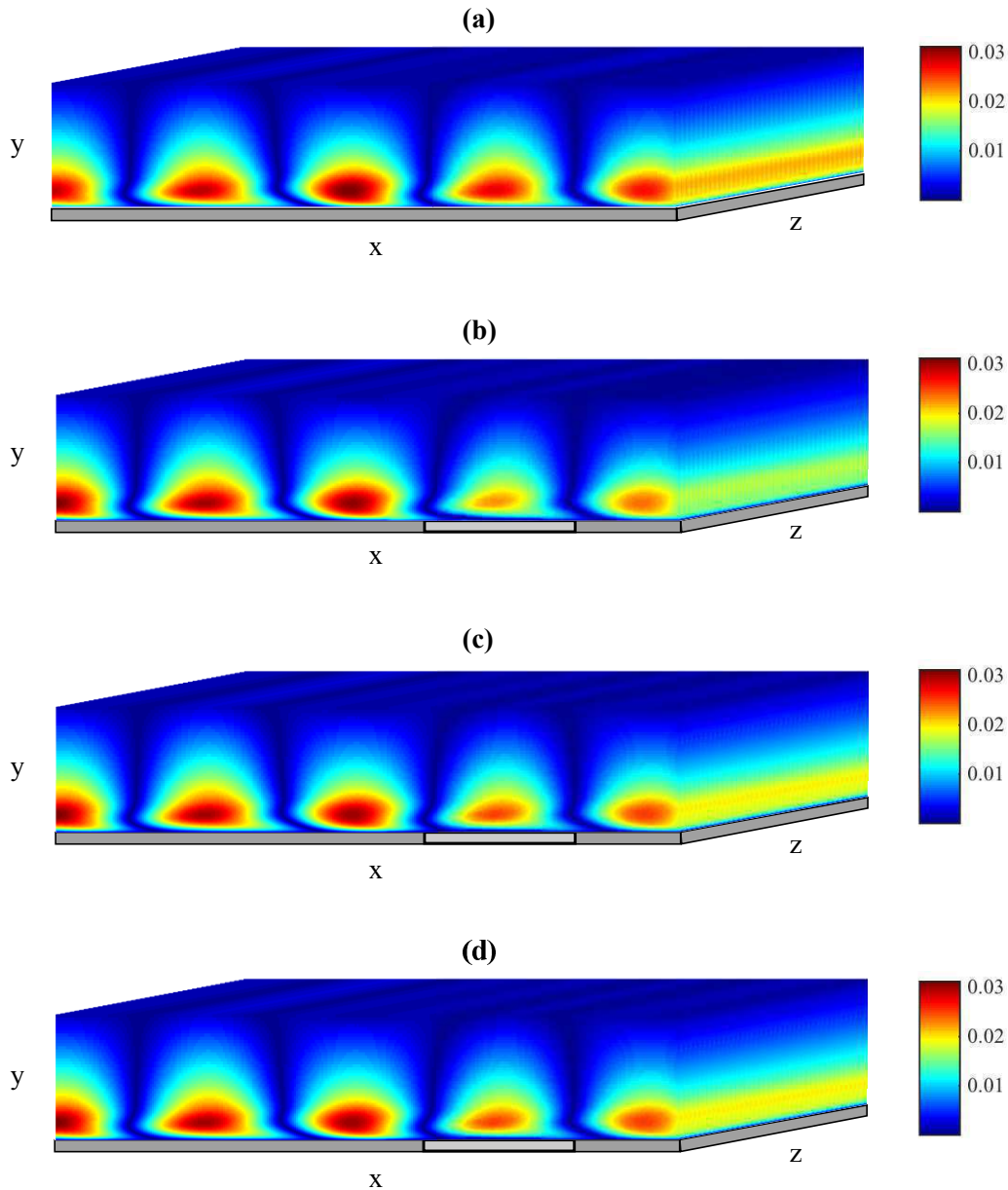


Figure 4.28: Instantaneous contours of streamwise perturbation velocity \hat{u} in the half-channel for (a) Rigid wall; (b) Case A-A; (c) Case B-B; (d) Case A-B. Gray strip indicates the control area.

The rigid wall case is presented in figure 4.28(a) in which the disturbances grow linearly in the streamwise direction. When a portion of the rigid wall is replaced by the phononic subsurface, a reduction in the amplitude of \hat{u} is observed, and is shown in figures 4.28(b-d). The streamwise extent of the subsurfaces are indicated by a shaded gray region on the wall. The reductions in the amplitude of \hat{u} follows the PKE reductions shown in table 4.7, where case A-A appears to have the strongest instantaneous attenuating effect. Case B-B and A-B show a similar trend in the both the instantaneous amplitude reductions of \hat{u} , in agreement with the PKE reductions presented earlier.

4.3.5 Summary and Conclusions

This section presented a low-disturbance transition scenario in which a discrete set of unstable TS modes were introduced in the flow field that spanned the unstable frequency range based on the solution of the Orr-Sommerfeld equation at a Reynolds number $Re = 7,500$. We then used two phononic subsurface designs to demonstrate the applicability of a phononic subsurface to reduce the perturbation energy present in the flow field. It was shown that each design acts rather independently on the structure and corresponds well with the expected performance of each TS mode described by the performance metric P . By comparing the energy spectra to the mean PKE (summation of all spectral modes), it was shown that the behavior of the PKE closely matched the behavior of each individual mode, and that any spurious modes introduced into the flow field were rather weak compared to the influence of the TS waves.

The recovery period of the most attenuated modes in each particular design was investigated, and it was shown that the larger the reductions in PKE, the faster the recovery period of the previously stabilized mode. Therefore, there is a balance between maximum PKE reduction and the extent that the reduction can be maintained downstream of the subsurface. The recovery of an individual mode can be delayed, however, by placing two contiguous subsurfaces downstream of one another of the same or similar design such that performance metric P is comparable at that specific frequency ω^* . It may be possible, then, to place a continuous array of subsurfaces downstream to delay the recovery period indefinitely and thus delay transition for a considerable

streamwise distance.

4.4 Control of K-type Instability Using Phononic Subsurfaces

4.4.1 Introduction

Secondary instability in both boundary-layers and channel flows can take three different forms, K-type (after Klebanoff), H-type (after Herbert) and C-type (after Craik) (Herbert, 1988). Here we will focus on K-type and H-type secondary instability in channel flows. K-type transition had been first identified in the boundary-layer transition experiments of Klebanoff et al. (1962), in which they observed the three-dimensional breakdown of an initially two-dimensional TS wave. This breakdown was observed experimentally as Λ vortices, where the streamwise wavelength of these structures matched that of the TS wave and were aligned in rows.

H-type instability is distinct from K-type in that instead of the vortices being aligned in rows, the structures are now staggered and have a wavelength that is twice that of the TS wave. Therefore this secondary instability is known as subharmonic transition. Although this type of instability has been predicted and even observed in numerical simulations (Herbert, 1988; Singer et al., 1989; Kucala and Biringen, 2014), its presence in a real transition experiment has been difficult to observe. Singer et al. (1989) and Kim and Moser (1989) attributed this to the presence of coherent streamwise vortices at the inflow in most experimental setups, which is a consequence of a non-trivial level of turbulence present at the inlet (freestream turbulence).

It is important to be able to control secondary instability, as transition from laminar to turbulent flows happens very rapidly once this three-dimensional breakdown occurs. Also, it is very unlikely that in a real transition scenario only two-dimensional waves will be present, as the freestream turbulence levels will contain a wide-spectrum of modes, including three-dimensional modes (in the form of streamwise vorticity). Due to the fact that H-type transition seems to be relatively rare [unless arbitrarily excited in a transition experiment (Saric et al., 1984)], we will focus on the control of a K-type transition scenario.

Earlier, we have demonstrated the applicability of a phononic subsurface to stabilize the TS wave when one or multiple waves are present in the flow field (sections 4.2 and 4.3, respectively).

The goal of this research endeavor will be to explore the applicability of the phononic subsurface to control a TS wave superimposed with three-dimensional waves. The three-dimensionality of the flow field leads to rapid streamwise growth in the perturbation velocities, and therefore the perturbation kinetic energy. While demonstration of the control of TS waves alone is beneficial in a controlled transition experiment, real transition contains a wide spectrum of three dimensional modes, the most amplified of which will contain the K-type modes (Kim and Moser, 1989; Singer et al., 1989). Therefore, exploring the applicability of phononic surfaces for this flow field will elucidate their applicability for flows in a more realistic transition environment.

4.4.2 Case Descriptions and Subsurface Design

4.4.2.1 Flow Field Parameters

In order to generate the disturbances that involve K-type transition, we will use the following inflow conditions

$$\begin{aligned} \mathbf{u}'(x=0, y, z, t) = & A_{2d} \text{Real}[\mathbf{u}_{e2d}(y)e^{-i\omega_{r2d}t}] \\ & + \frac{1}{2}A_{3d} \text{Real}[\mathbf{u}_{e3d}^+(y)e^{i(\beta z - \omega_{r3d}t)}] + \frac{1}{2}A_{3d} \text{Real}[\mathbf{u}_{e3d}^-(y)e^{i(\beta z - \omega_{r3d}t)}] \end{aligned} \quad (4.22)$$

where ω_{r2d} and ω_{r3d} are the real, non-dimensional frequencies for both two-dimensional and three-dimensional disturbances, respectively. When $\omega_{r2d} = \omega_{r3d}$, K-type transition will occur. $\mathbf{u}_{e2d}(y)$ corresponds to the two-dimensional eigenfunction of the disturbance from the solution of the Orr-Sommerfeld equation, and $\mathbf{u}_{e3d}(y)$ corresponds to the three-dimensional eigenfunction. In addition, A_{2d} and A_{3d} correspond to the amplitude of the two- and three-dimensional eigenfunctions, respectively. Also, β is the spanwise wavenumber. Generation of the eigenfunctions to satisfy the dispersion relationship $F(Re, \omega_r, \pm\beta) = 0$ is accomplished using an existing solver for the Orr-Sommerfeld equation (Eq. 1.2) (Reynolds, 1969).

| Re | A_{2d} | A_{3d} | ω_{r2d} | ω_{r3d} | β |
|------|-------------|------------|----------------|----------------|---------|
| 7500 | $0.0225U_c$ | $0.002U_c$ | 0.25 | 0.25 | ± 1 |

Table 4.8: Computational parameters for K-type instability

The case we will run can be found in Table 4.8. For this given Reynolds number, ω_{r2d} was chosen as it yields the least damped eigenvalue for the two-dimensional problem (highest TS wave growth rate). $\omega_{r3d} = \omega_{r2d}$ was selected as this represents a K-type transition scenario (Saiki et al., 1993). Also, this was the Reynolds number/frequency combination used in our study of phononic surfaces to control primary instability (Section 4.2).

For the present simulations, $Re = 7500$, $U_c = 17.8$ m/s, $\delta = 4.2 \times 10^{-4}$ m, and $\nu = 1 \times 10^{-6}$ m²/s (water). Also, $\omega_{r2d} = \omega_{r3d} = 0.25$ where the non dimensional circular frequency is dimensionalized through Eq. 4.19. For these simulations, the primary real frequency corresponding to ω_{r2d} is $\omega^* = 1690$ (Hz).

4.4.2.2 Phononic Subsurface Design

The design of the subsurface for this problem is given in figure 4.29. Here, the subsurface was designed such that both the primary mode (1690, 0) and harmonic (3380, 0) lie in a band gap and to the right of the truncation frequency of each gap. Therefore, it may be hypothesized that both of these modes should be attenuated in space since the performance metric P lies near a minimum for these two modes.

The unit cells are composed of layers of Aluminum (Al) and Acrylonitrile butadiene styrene (ABL) plastic and the arrangement of these materials in the periodic lattice is inlayed in figure 4.29(a). The material property ratios are $\rho_{Al}/\rho_{ABS} = 2.6$, $E_{Al}/E_{ABS} = 28.7$, and $c_{Al}/c_{ABS} = 3.3$, where ρ is the material density, E is Young's modulus and c is the speed of sound in the material. The dispersive characteristics of a periodic composite is determined by the ratios of material properties, and not the absolute properties of the individual constituents. For completeness: the individual material properties are $\rho_{Al} = 2700$ Kg/m³, $\rho_{ABS} = 1040$ Kg/m³, $E_{Al} = 68.8$ GPa, $E_{ABS} = 2.4$ GPa, $c_{Al} = 5051$ m/s, and $c_{ABS} = 1519$ m/s. The unit cell length is 41.1 cm for this design.

A viscoelastic damping model to model the material damping. This introduces an additional matrix (\mathbf{C}) in the system where $\mathbf{C} = p\mathbf{M} + q\mathbf{K}$, for stiffness proportional damping $p = 0$. The

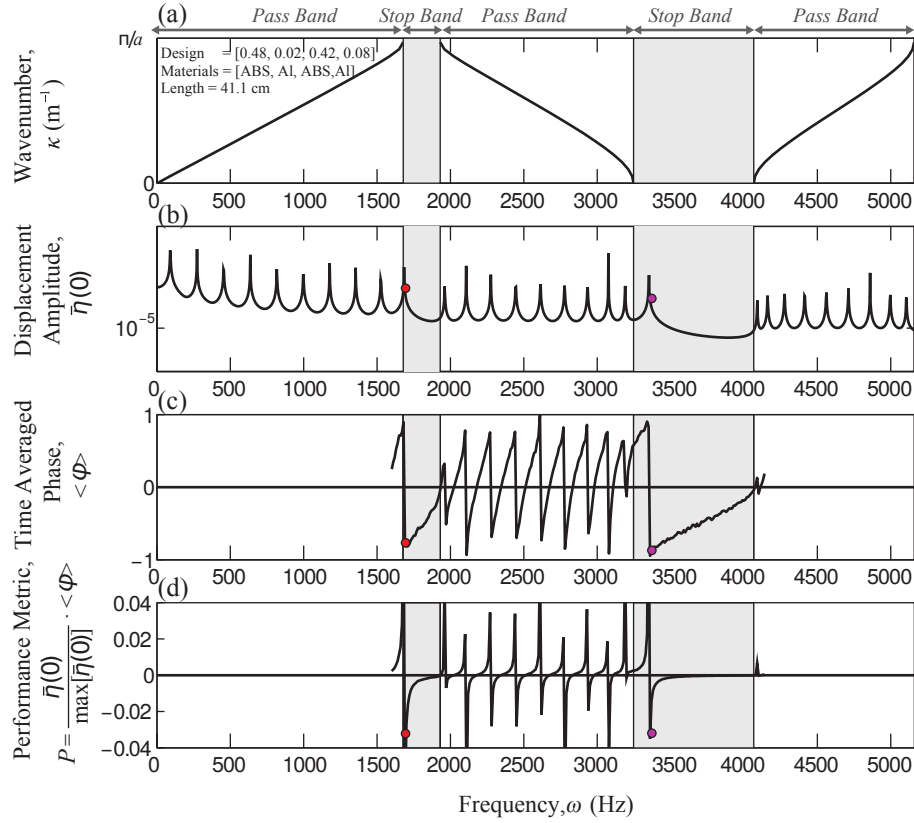


Figure 4.29: Phononic subsurface design to control 3D disturbances; (a) Dispersion curves for the 1D phononic crystal from which the subsurface is composed (material arrangements of the 1D periodic lattice is detailed on the inset). (b) Steady-state vibration response of phononic crystal top surface. (c) Time-averaged phase between force and displacement at the phononic crystal top surface. (d) Performance metric combining amplitude and relative phase between the force and the displacement at the phononic crystal top surface. Red dot indicates location of primary mode (1690, 0); Magenta dot indicates location of first harmonic (3380, 0)

damping constants $q_{\text{ABS}} = 6 \times 10^{-8}$ and $q_{\text{Al}} = 0.1 \times q_{\text{ABS}}$. This translates into $\max(\zeta_2(\kappa)) = 0.06\%$, where $\max(\zeta_2(\kappa)) = \max(\frac{1}{2}q\omega(\kappa))$ is the maximum shift in the optical branch of the dispersion diagram due to the presence of damping.

4.4.2.3 Coupled Simulation Geometry

The geometry of coupled fluid/structure simulations will follow that of figure 4.13(a) in which a single subsurface will replace a portion of the all-rigid bottom wall. The subsurface will span from $x_s^* = 0.0092 \text{ m} \rightarrow x_e^* = 0.0099 \text{ m}$ and spans approximately one quarter wavelength of the primary

2D disturbance. This allows us to take a midpoint in the pressure signal which will act as the forcing to the structure, similar to the method outlined in section 4.2. In the spanwise direction, one can not simply assume the structure to be homogenous, owing to the three-dimensional nature of the pressure signal in that direction. Therefore, in the spanwise (z) direction, the 1-D structure should be placed at every gridpoint in the spanwise direction, such that the structure will conform to the spanwise pressure waves which have non-zero β wavenumber. Therefore, the structure can be described as being quasi two-dimensional, where only wall-normal displacements will be considered. Once the K-type structures are fully formed within the channel, and are independent of time-step and grid size, we initiate control using the method outlined in Section 4.2.

4.4.3 Results

Streamwise and wall-normal integrated perturbation kinetic energy

$$S_f^*(t^*, z^*) = \rho_f \int_0^\delta \int_0^{L_x} \frac{1}{2} (\hat{u}^{*2} + \hat{v}^{*2} + \hat{w}^{*2}) dx^* dy^* \quad (4.23)$$

is used to assess the effect of the phononic subsurface on the total perturbation kinetic energy in the flow field. This equation is similar to the Eq. 4.14, however due to the three dimensional nature of the disturbance field, the spanwise integration is omitted. This provides a three-dimensional representation of the flow field energetics. In order to determine whether the subsurface is stabilizing or destabilizing to the flow field, the arithmetic difference between the integrated energy of a controlled case S_f^{*c} and “no control” case (rigid wall) S_f^{*nc} is plotted as a function of time, t^* and spanwise position z^* , shown in figure 4.30.

From this figure, we see that the influence of the subsurface is to lower the perturbation KE, on average, compared to an all rigid wall case due to the overall negative value of $T_f^{*c} - T_f^{*nc}$. Also, we see that the perturbation energy is decaying in time which shows that the subsurface is not introducing any temporally unstable modes in time and indicates that the truncation mode in the structure is below that of the primary energy carrying wave (see figure 4.20). Also, the spanwise distributions of the perturbation energy show the wave-like nature of the disturbances both in the

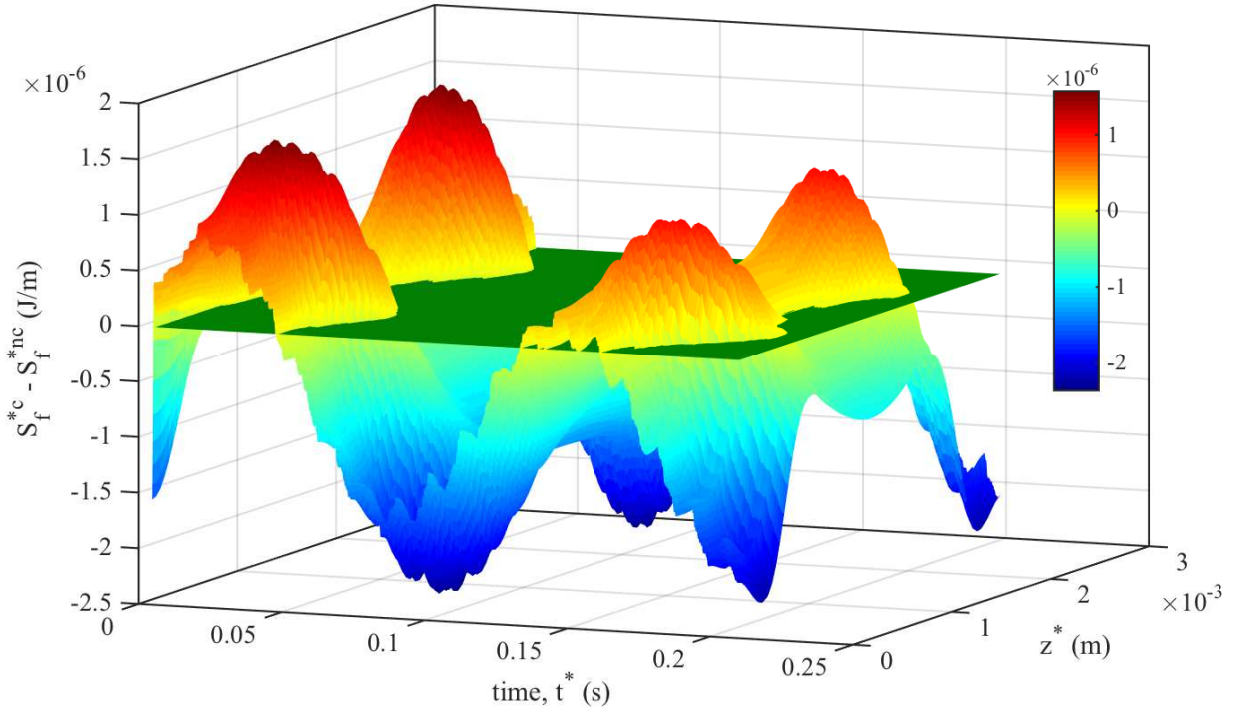


Figure 4.30: Surface of $S_f^{*c} - S_f^{*nc}$ as a function of time t^* and spanwise position z^*

flow field and on the phononic subsurface.

The total reduction in the time averaged perturbation kinetic energy (PKE) in the fluid

$$K_f^*(x^*) = \frac{\rho_f}{(t_f^* - t_0^*)} \int_{t_0^*}^{t_f^*} \int_0^{L_z} \int_0^{L_y} (\hat{u}^{*2} + \hat{v}^{*2} + \hat{w}^{*2}) dy^* dz^* dt^* \quad (4.24)$$

is shown in figure 4.31 for all cases presented here. Here, $K_f(x^*)$ is a function of the dimensional streamwise coordinate x^* , t_0^* defines the beginning of the time-averaging window and t_f^* denotes the end of the time-averaging window. The time averaging window was taken when the PKE in the fluid domain exhibited a periodic steady-state such that the statistics were invariant of the time averaging window. Streamwise distributions of PKE are important as they contain all of the spectral characteristics in the fluid, and provides a measure of the contribution of spurious wall modes excited in the flow field due to the unique dispersion characteristics of the phononic subsurface.

From this distribution, we see that the mean PKE is lower than that of a rigid wall case, and

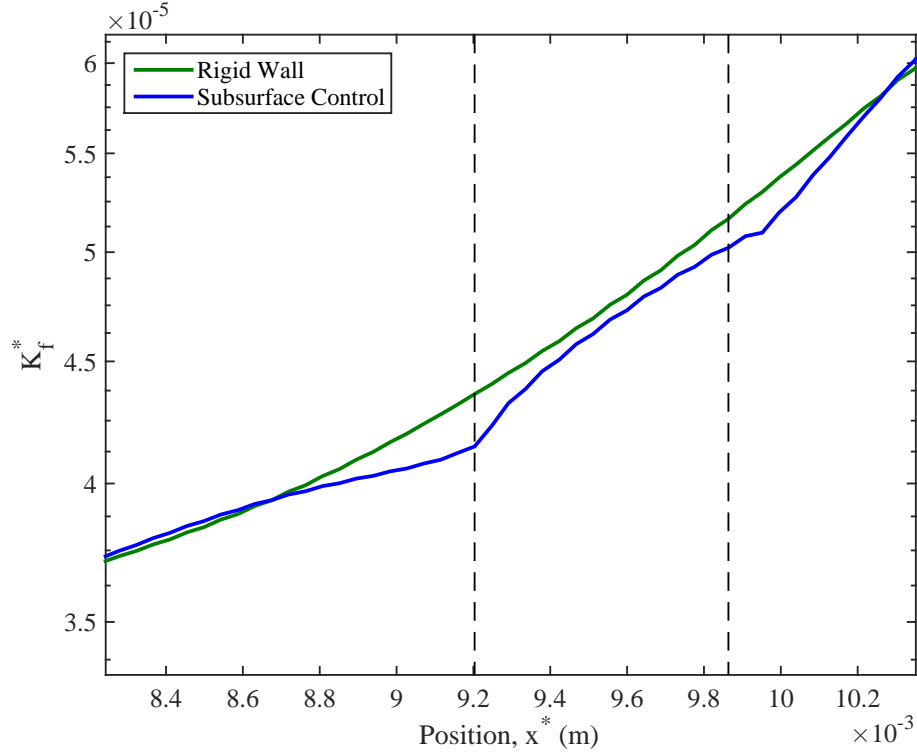


Figure 4.31: Mean perturbation kinetic energy in the fluid K_f^* as a function of streamwise position x^* . Dashed vertical lines indicate upstream and downstream boundaries of the subsurface surface

has a maximum reduction of approximately 5%. Here we demonstrate that even in the presence of a three dimensional disturbance that exhibits nonlinear growth, the flow field is still grossly stabilized due the placement of the frequency of the primary 2D disturbance relative to the truncation such that the performance metric P is both negative and large, shown in figure 4.29.

It has been observed earlier that this stabilizing phenomenon can be attributed to a reduction, on average, of the perturbation energy production term (term i in Eq. 4.16) by altering the correlation between the streamwise and wall-normal perturbation quantities, \hat{u}^* and \hat{v}^* respectively. When this correlation is predominantly negative, there is a net increase in the total perturbation energy. Similarly, when the correlation is positive (or less negative) the net increase in perturbation kinetic energy is negative (or less positive). Here, we assess the correlation of these two flow field quantities through the dot product $\hat{u}^* \cdot \hat{v}^*$ as a function of time and compare this quantity to the

trend of volume integrated perturbation kinetic energy (Eq. 4.14) in the flow field compared to a rigid wall case. The correlations are taken at a location $x = 22.4\delta$, $y = 0.177\delta$, $z = 1.396\delta$ and roughly corresponds to a position of peak production for a rigid wall transition scenario. The location in the streamwise position x was chosen such that a comparison between a rigid wall and subsurface case can be made. This comparison is made in figure 4.32.

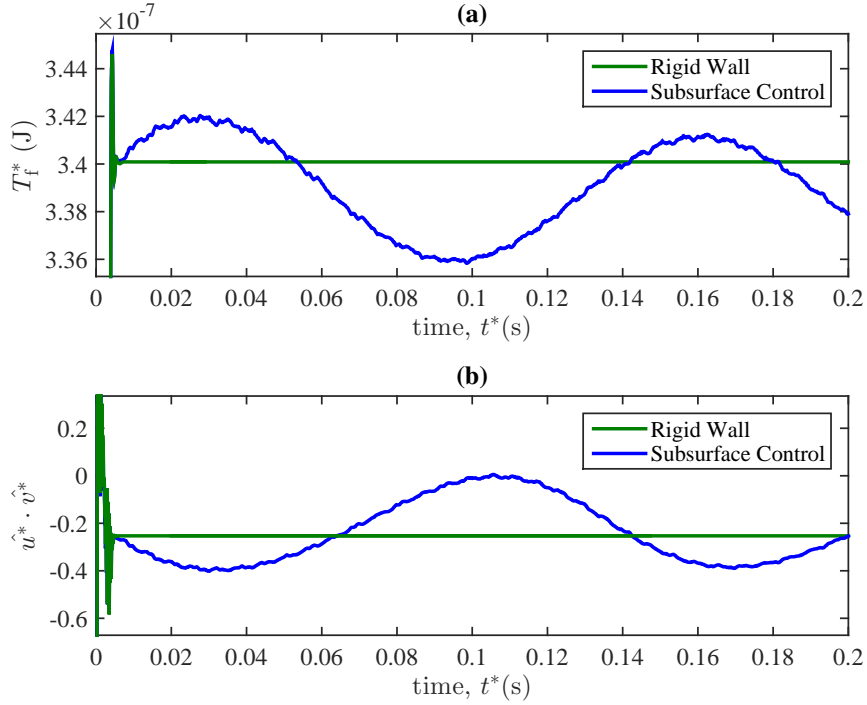


Figure 4.32: Rigid wall and control case comparisons of (a) Volume integrated PKE T_f^* ; (b) Perturbation velocity correlations $\hat{u}^* \cdot \hat{v}^*$ at $x = 22.4\delta$, $y = 0.177\delta$, $z = 1.396\delta$.

In figure 4.32(b), we see that for the rigid wall, after the initial transients settle, $\hat{u}^* \cdot \hat{v}^*$ is constant and negative, indicating that there is a net increase in perturbation kinetic energy at the location of the phononic subsurface. The volume integrated perturbation energy for the rigid wall case remains constant as well (figure 4.32(a)). The influence of the phononic subsurface on the velocity correlations $\hat{u}^* \cdot \hat{v}^*$ is evident in figure 4.32(b), showing that the correlations oscillate with the same frequency as the volume integrated perturbation energy (figure 4.32(a)). That is, when the correlations become more negative, the perturbation energy increases in comparison to a rigid

wall. Alternatively, when the correlations become more positive, the perturbation energy decreases with respect to a rigid wall. These comparisons show a direct influence of the perturbation energy production on the total perturbation energy in the fluid, and that the main mechanism of this control strategy is to alter the correlations between the perturbation velocity components, and on average result in a net decrease in the PKE.

In order to assess this phononic subsurface's effect on the various modes in the flow, we use the integrated perturbation energy spectra

$$E^*(x^*, \omega^*, \beta) = \rho_f \int_0^\delta (\hat{u}^{*2} + \hat{v}^{*2} + \hat{w}^{*2}) dy^* \quad (4.25)$$

integrated over the half channel. This quantity represents the spectral contributions of the total perturbation kinetic energy in the fluid and these modes can be expressed as a pair $(\omega^*, n\beta_r)$ where n is an integer and β_r is the real spanwise wavenumber $2\pi/L_z$ and is non dimensional. For example, the primary mode (TS mode) is expressed as the pair (1690, 0) and represents a two-dimensional mode. Also, the fundamental K-type mode is expressed as (1690, 1) and the TS wave harmonic is expressed as (3380, 0). The streamwise evolution of these selected modes are shown in figure 4.33. From these distributions, the primary mode (1690, 0) exhibits a similar streamwise evolution as the mean PKE (figure 4.31) where significant upstream effects and the concavity of the energy distributions over the length of the subsurface is observed. The reduction in this primary mode, then, is responsible for a majority of the reduction in the mean PKE and is similar to the results exhibited in section 4.3 in which the reductions in the primary mode attributed to the total reductions in PKE. The fundamental and harmonic modes, shown in figures 4.33(c) and (b), respectively, exhibit rather modest growth when passing over the phononic subsurface. However, the magnitude of these modes is significantly less than the magnitude of the primary mode, and therefore contributes very little to the total PKE.

It is interesting, however, that these modes are not positively affected by the subsurface. The fundamental mode represents a three-dimensional mode and includes spanwise variations in the pressure signals which feeds into structure displacement. As shown in figure 4.30, the subsurface's

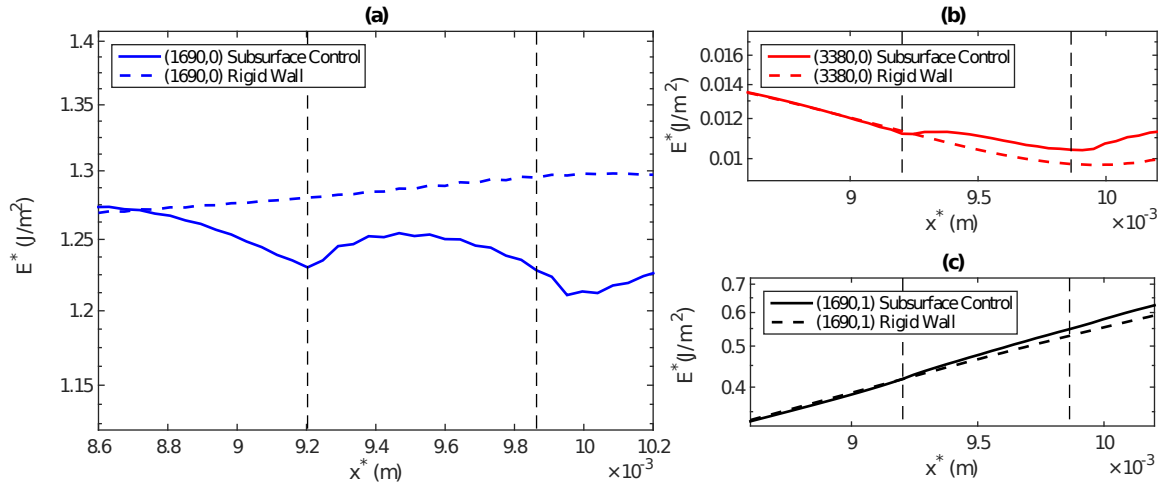


Figure 4.33: Streamwise evolution of modal energy E^* for (a) Primary TS mode (1690,0); (b) Harmonic of TS mode (3380,0); (c) Fundamental K-type mode (1690,1).

influence on the flow field shows spanwise variation, though it appears from figure 4.33 that the highest energy carrying mode is the primary mode and thus the subsurface primarily influences this mode. For the harmonic, the placement of this mode relative to a second truncation frequency in figure 4.29(d) suggests that this mode should be attenuated. However, the growth of the (3380,0) mode can be directly attributed to the weak nonlinear interaction of the primary mode through the streamwise advective terms in the Navier-Stokes equation. Therefore, it appears that the phononic subsurface design methodology used to affect a primary disturbance is not applicable to disturbances that grow through nonlinear modal interactions, at least in this current design configuration. However, when the (3380,0) mode is introduced as a primary mode, this mode experiences stabilization in the presence of the subsurface (not shown).

4.4.4 Summary and Conclusions

Here, a channel flow was subject to K-type instability, whereby a phononic subsurface was installed in place of a rigid wall at the bottom of the channel. The distinction here is that the waves are now three-dimensional and have spanwise variation, where the fundamental wave has

much larger spatial growth rates compared to the two dimensional TS wave. It was found that the phononic subsurface was successful in reducing the total perturbation kinetic energy in the flow field in both time and space. The main mechanism involved the attenuation of the TS wave through the alteration of the phase between the streamwise and wall-normal velocity components in the critical layer. The other modes, however, were actually destabilized by the presence of the subsurface. This destabilization was rather weak compared to the stabilization of the TS wave, and therefore the total perturbation energy (as a summation of all spectral modes) remained below that of the rigid wall case over the subsurface. Therefore, the TS wave was stabilized even in the presence of three dimensional waves, and the total perturbation energy was overall lower than a rigid wall case, demonstrating the applicability of these subsurfaces to lower the perturbation energy in the flow field for weakly nonlinear high amplitude waves.

Chapter 5

Bursting Frequency in a Turbulent Channel Flow

5.1 Introduction

In wall-bounded turbulent flows, the important characteristics of the near-wall region of the flow are governed by the low-velocity streaks in the sublayer (Kline, Schraub, and Runstadler, 1967). Typically, these low-velocity streaks have a streamwise length of approximately $1000\nu^*/u_\tau^*$ and a spanwise spacing of about $100\nu^*/u_\tau^*$ (Kim, Moin, and Moser, 1987) where ν^* is the dimensional kinematic viscosity and u_τ^* is the wall-shear velocity defined as

$$u_\tau^* = \sqrt{\left. \frac{1}{\rho^*} \frac{dU^*}{dy^*} \right|_w} \quad (5.1)$$

where U^* is the mean velocity, y^* is the wall-normal coordinate, ρ^* is the fluid density, and the subscript “w” refers to a wall quantity.

These low-velocity streaks are then ejected into the outer region of the flow, and these ejection events contribute to a major part of the Reynolds stress and turbulent energy production in the boundary layer (Kim, Kline, and Reynolds, 1971). The ejection of low-speed fluid away from the wall is often referred to as a “burst” and will be used interchangeably throughout this chapter. As these low-speed streaks are ejected away from the wall, the low-speed fluid in the near-wall layer is then replaced by high-speed fluid from the outer layer, which is commonly referred to as a “sweep” event (Kim, Moin, and Moser, 1987; Corino and Brodkey, 1969). An important property of these streaks is that they appear to form between a pair of counter-rotating streamwise vortices (Blackwelder and Haritonidis, 1983) and that the ejection and sweep events that characterize the

motion of these streaks are influenced by these streamwise vortex pairs.

Ejection and sweep events are typically characterized by evaluating the Reynolds shear stress $\overline{u'v'}$ using a quadrant based analysis where u' is the abscissa and v' is the ordinate in a cartesian coordinate system. For an ejection, $u' < 0$ and $v' > 0$ and therefore is described as a second quadrant event $(\overline{u'v'})_2$. For a sweep event, $u' > 0$ and $v' < 0$ and is described as a fourth quadrant event $(\overline{u'v'})_4$. It was found by Lu and Willmarth (1973) that the ejection events contribute about 77% to $\overline{u'v'}$ and the sweep events contribute about 55% to $\overline{u'v'}$, where the excess of 100% is balanced by the negative contributions of the first and third quadrant events (Kim et al., 1971; Lu and Willmarth, 1973).

The largest contribution of turbulent energy production is attributed to the second quadrant events and is therefore an important quantity to identify within a turbulent wall-bounded flow. A number of techniques have been used to identify turbulent bursts. One such technique employed is the variable-interval time-averaging (VITA) algorithm first used by (Blackwelder and Kaplan, 1976) which takes into account large streamwise velocity gradients to characterize the bursting event. Another technique used involves detecting a second quadrant event $(\overline{u'v'})_2$ that is above some threshold magnitude to identify a burst. Bogard and Tiederman (1986) made a comparative study between these (and other) burst measurement techniques and found that the quadrant based technique had the greatest reliability and probability of detecting ejection events when compared to dye-flow experimental visualizations.

Using these aforementioned measurement techniques, one can identify the frequency or period of these burst events and in principle disrupt these burst events to lower the turbulent production, and therefore lower the skin friction. Here, we simulate a turbulent channel flow with either periodic or inflow streamwise boundary conditions and measure the period between bursts, burst period, and convection velocity of the structures associated with these burst events using flow visualizations of Lagrangian Coherent Structures and the second quadrant technique $(\overline{u'v'})_2$.

5.2 Case Descriptions

Two cases will be run at a Reynolds number based on the laminar centerline velocity $Re_{cl} = 8000$, which corresponds roughly to a Reynolds number based on the friction velocity $Re_\tau = 200$. One case will consist of periodic boundary conditions in the streamwise direction and is denoted as Case P. The second case will use crossflow planes sampled from case P as inflow boundary conditions in order to emulate spatial turbulence and will be hereby referred to as Case S. The details of this sampling method will be discussed in section 5.2.2. The physical domain lengths, corresponding resolutions, and Reynolds numbers of these two cases is summarized in table 5.1.

| Case | Re_τ | $N_x \times N_y \times N_z$ | L_{x^*} | L_{y^*} | L_{z^*} |
|------|-----------|-----------------------------|--------------|-----------|-------------|
| P | 200 | $256 \times 129 \times 128$ | $4\pi\delta$ | 2δ | $\pi\delta$ |
| S | 200 | $100 \times 129 \times 128$ | $2\pi\delta$ | 2δ | $\pi\delta$ |

Table 5.1: Case summary

5.2.1 Periodic Channel

For Case P we use periodic boundary conditions in the streamwise x direction to simulate a turbulent channel flow in a periodic domain. We initiate this flow field by superimposing high-amplitude two-dimensional and three-dimensional disturbances on a laminar channel flow profile which acts to “trip” the flow into turbulence. As the flow transitions, we track the wall-shear u_τ as a function of time until the flow reaches a statistical steady state. All statistical quantities are averaged in the periodic directions as these are assumed to be infinite and therefore invariant in space. All time averaged flow field quantities are denoted by an overbar ($\bar{\cdot}$). In addition, any quantity with a superscript $+$ has been nondimensionalized using wall units (e.g. $y^+ = y^*u_\tau^*/\nu^*$).

The mean velocity U^+ as a function of y^+ is given in figure 5.1 for Case P. In this distribution, the red-dashed line represents the expected shape of the viscous sublayer (Pope, 2008) and the black-dashed line represents the log layer (von Karman, 1930) where

$$U^+ = \frac{1}{\kappa} \ln y^+ + B \quad (5.2)$$

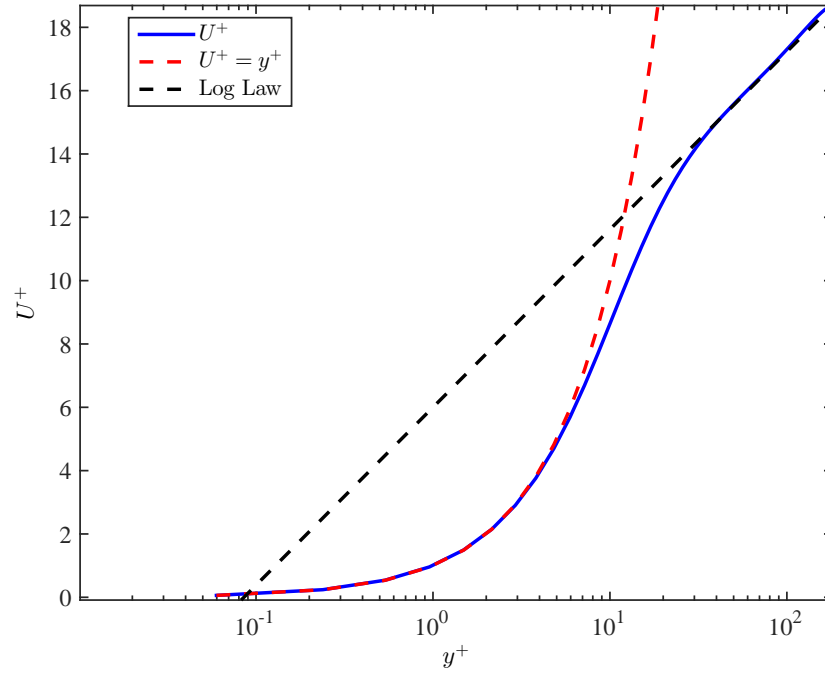


Figure 5.1: Mean velocity U^+ in wall-units for Case P; the black dashed line represents the log law given in Eqs. 5.2-5.3.

where B is a constant and κ is the von Karman constant. The values of these constants in figure 5.1 are

$$\kappa = 0.41, B = 5.2 \quad (5.3)$$

and are in close agreement with the accepted values in the literature (Pope, 2008). The viscous sublayer exhibits a linear relationship with the mean velocity, due to the dominance of viscosity in this region of the flow, when scaled with wall coordinates and shows good agreement with the expected linear trend when $y^+ < 5$. Similarly, the outer layer is well represented using the law of the wall (Eq. 5.2) when $y^+ > 40$. These distributions of mean velocity agree very favorably with previous direct numerical simulations of turbulent channel flow (Kim et al., 1987), in which we capture both the viscous sublayer and the outer layer to high fidelity.

Root-mean-squared distributions (r.m.s.) of the perturbation velocity components u' , v' , and w' across the channel are represented in figure 5.2, where these quantities are normalized by

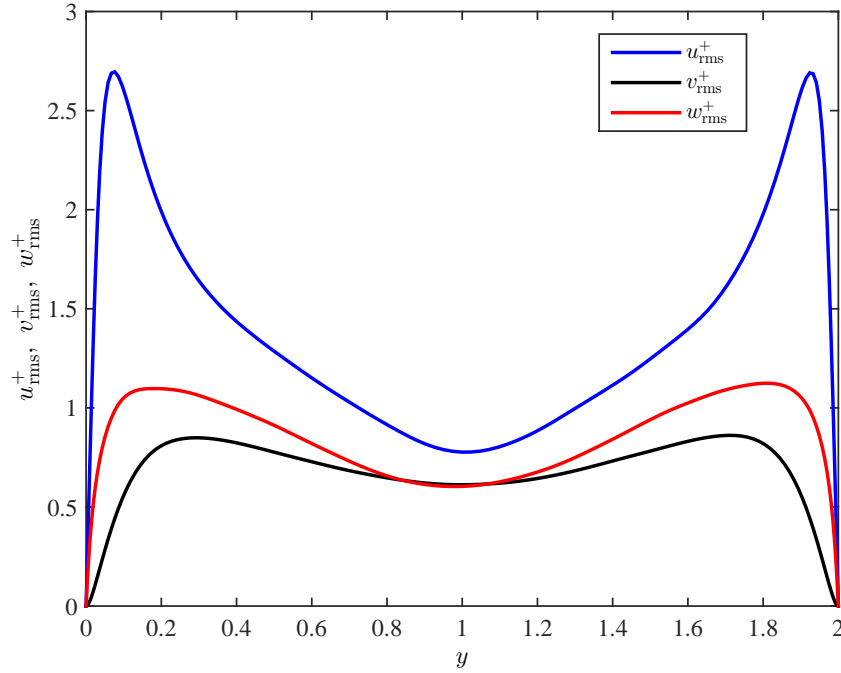


Figure 5.2: Root-mean-squared distributions of u_{rms}^+ , v_{rms}^+ , w_{rms}^+ across the channel.

the wall-shear velocity u_τ . Excellent agreement is observed with the literature (Kim et al., 1987), where the symmetry displayed across the channel indicates the adequacy of the sample taken for the average. In addition, the peaks of the maximum rms values are in near-exact agreement with Kim et al. (1987) for each velocity component, the largest in magnitude being the streamwise component.

Distributions of the shear stress $\overline{u'v'}$ and total shear stress τ given as

$$\tau = \overline{u'v'} + \frac{1}{Re} \frac{\partial U}{\partial y} \quad (5.4)$$

are shown in figure 5.3. In fully developed turbulent channel flow, the total shear τ must balance the mean streamwise pressure gradient dP/dx (Pope, 2008). Since dP/dx is a constant, the total shear stress τ must be linear and is therefore an indicator of whether true steady state turbulence is being modeled. We exhibit this linear trend in the total shear stress in figure 5.3 which shows that the flow field has achieved a state of fully developed turbulent channel flow. In addition, the

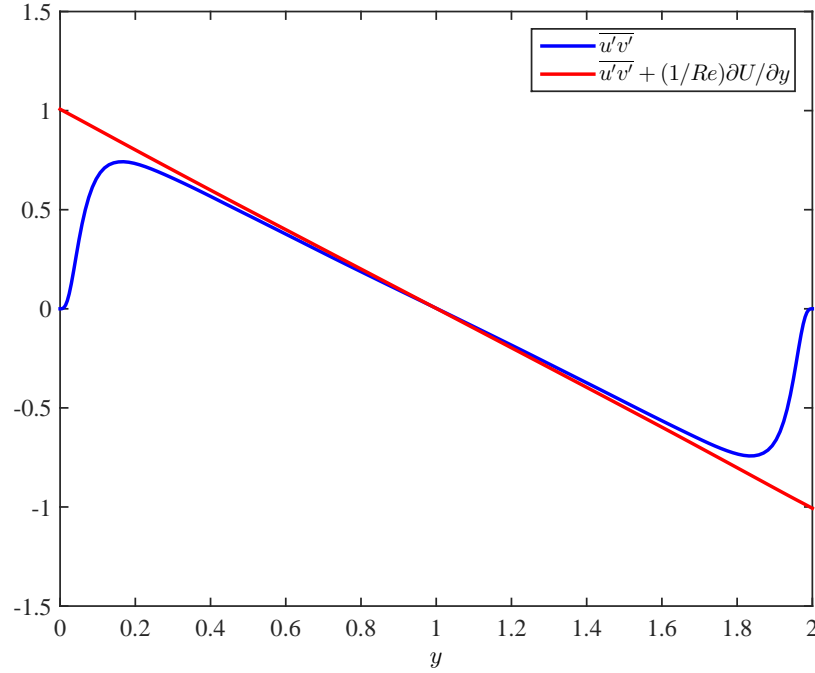


Figure 5.3: Shear stress distributions $\overline{u'v'}$ and total shear τ across the channel

Reynolds shear stress $\overline{u'v'}$ exhibits negative symmetry across the center of the channel and agrees well with Kim et al. (1987).

Ensemble averaged streamwise and spanwise energy spectra taken at $y^+ = 21.2$ is shown in figures 5.4(a) and (b), respectively. This location in the wall-normal direction corresponds to the location of peak production (Kim and Spalart, 1987). Here, k_x represents the streamwise wavenumber and k_z represents the spanwise wavenumber. These distributions show the adequacy of the streamwise and spanwise resolution owing to the exponential decay of the energy spectra from low wavenumbers (large scales) to high wavenumbers (small scales) over several decades. Also, no evidence of energy pile up (aliasing) is present in the higher wavenumbers and the streamwise spectra compares favorably with Kim et al. (1987). It should be noted that the spanwise domain length $L_z = \pi$ is shorter than what was used by Kim et al. (1987), however the spanwise spectra agrees favorably with the minimal flow unit (MFU) study carried out by Jimenez and Parvis (1990) and thus is adequate in representing the turbulent dynamical processes taking place in the spanwise

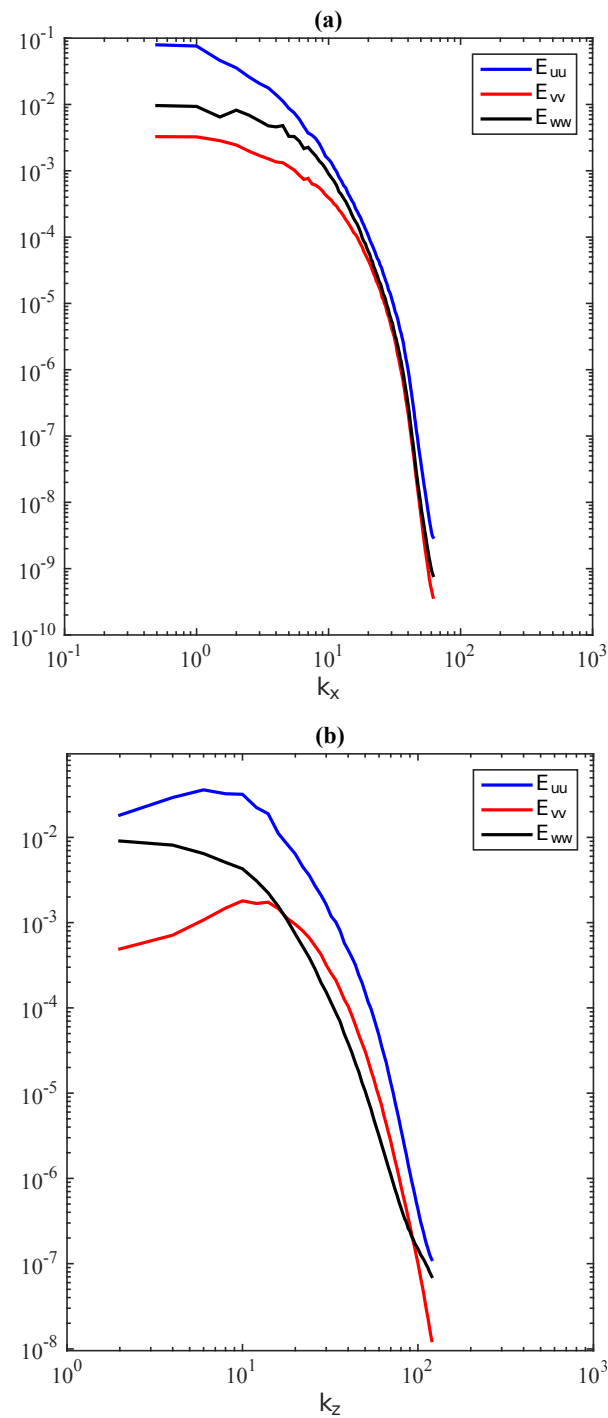


Figure 5.4: Energy spectra of Case P for the streamwise E_{uu} , wall-normal E_{vv} , and spanwise E_{ww} velocity components at $y^+ = 21.2$; (a) Streamwise spectra, (b) Spanwise spectra

direction.

The distributions of mean velocity, Reynolds stresses, and energy spectra presented here confirm the accuracy of the turbulent periodic channel flow being modeled. This flow field can be used to detect ejection (or bursting) events and will be presented in section 5.3.1. Also, crossflow (y, z) planes from the velocity field data can be used as inflow conditions for the spatial model of turbulent channel flow (Case S), where a direct comparison of the bursting frequencies and coherent flow structures can be made between a periodic and spatial turbulent channel flow.

5.2.2 Spatial Channel

For Case S, we use a spatial model for turbulent channel in which the streamwise direction is finite, and thus requires boundary conditions at both the inflow and outflow planes. At the inflow, we take (y, z) planes from Case P at $x^* = 2\pi\delta$ for the streamwise u , spanwise w , and wall-normal v velocity components and use these as inflow boundary conditions in the spatial channel model. This method was used in Chung and Sung (1997) and was shown to exhibit the correct phase information and dynamics in a turbulent channel flow. An example of the streamwise u plane used as an inflow condition is shown in figure 5.5. For the results that follow for Case S, we sample the inflow planes at roughly $0.08 \delta/U_{cl}$ over a total period $T = 240 \delta/U_{cl}$. This sampling provides both high fidelity sampling in time while allowing 240 eddy turnover cycles to occur before recycling the inflow planes. It would be ideal for no recycling to take place ($T = \infty$), however the amount of I/O required would render this unfeasible and therefore T must be finite. The outflow is handled by employing a buffer zone encompassing roughly 50% of the computational domain which allows the disturbances to propagate out of the physical domain without reflections (see section 3.1.6).

A comparison of the rms values of the streamwise, wall-normal, and spanwise velocity components (normalized by u_τ) is made between Case S and Case P in order to assess the validity of the inflow conditions; this is shown in figure 5.6. It is evident that the ensemble averages of these r.m.s. distributions compare well with one another, where small deviations from the periodic channel flow distributions can be observed in the spatial case. In addition, comparisons of the ensemble averaged shear stress distributions $\overline{u'v'}$ and total shear τ are made between Case P and Case S

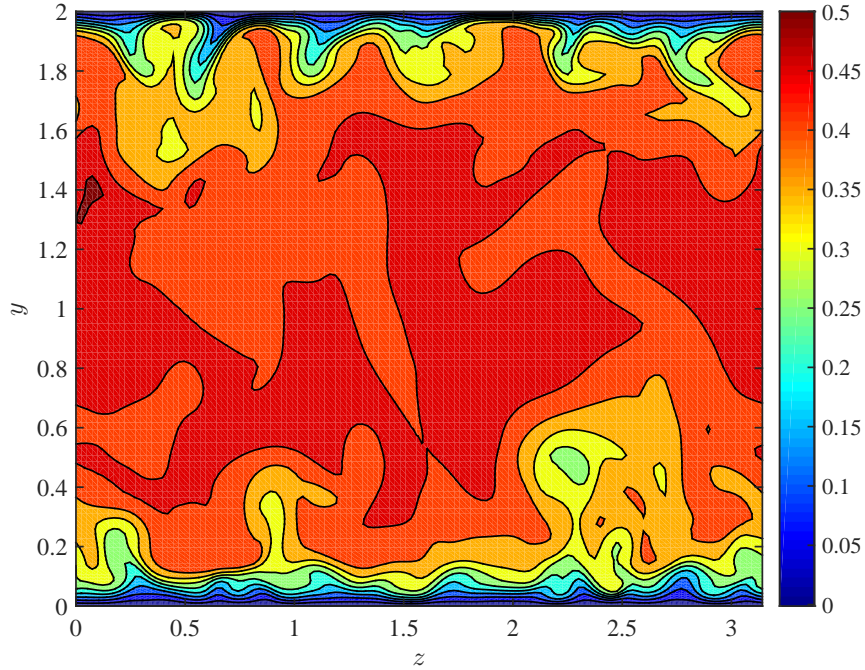


Figure 5.5: Crossflow plane of u at $x^* = 2\pi\delta$ and time $t^* = 2064 \delta/U_{cl}$

in figure 5.7. Again, very small differences are noted between the periodic and spatial cases and the comparison is favorable. By comparing the total stress and rms distributions for both periodic and spatial turbulent channel flow models, it appears that the inflow conditions used in Case S are adequate and that direct comparisons with Case P can be made in the subsequent sections.

Temporal energy spectra at $x^+ = 628$ ($x = \pi$) and $y^+ = 21.2$ is presented in figure 5.8. Here, the energy spectra is now a function of non-dimensional frequency ω as there is no periodicity in the streamwise (x) direction. The spectra shows similar behavior to the streamwise spectra previously shown in figure 5.4(a), although the drop off to the higher frequencies (or wavenumbers) is less pronounced in the spatial case. However, there is an exponential drop off in the energy along with a well developed integral region (Pope, 2008).

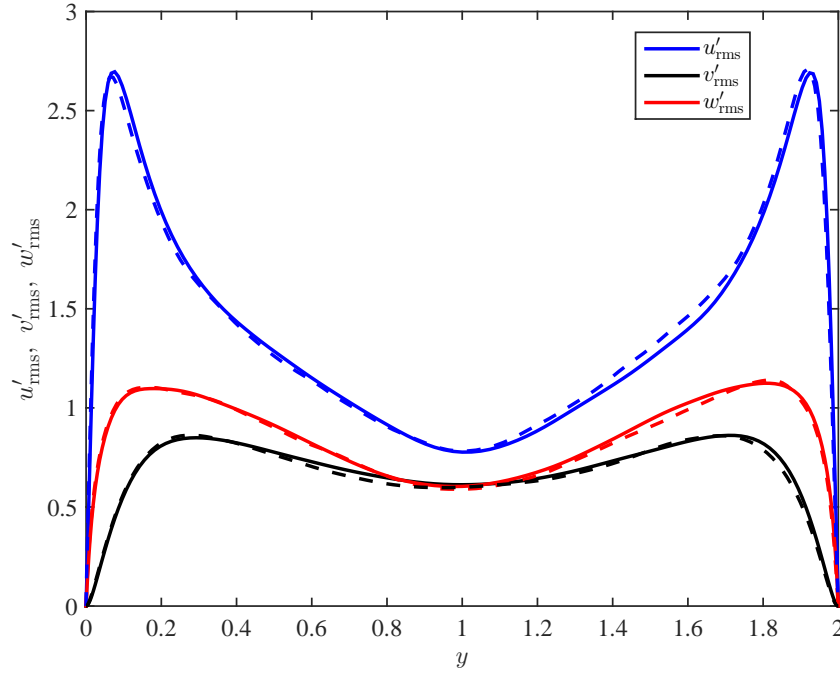


Figure 5.6: Comparison of root-mean-squared distributions (normalized by u_τ) between Case P (solid lines) and Case S (dashed lines).

5.3 Results and Discussion

This section is split into three subsections. The first subsection details the identification of bursting events using (x, z) planes of streamwise u' and wall-normal v' perturbation velocity for both Case S and Case P, whereby identification is carried out using the second quadrant technique (Lu and Willmarth, 1973; Kim and Spalart, 1987; Bogard and Tiederman, 1986). In the second subsection we will use the method of Lagrangian Coherent Structures (LCS) to identify coherent structures in the turbulent channel for Case S. In addition, identification of bursting events and their correlation with the LCS technique will be made. The third section we will carry out the transformation of mean burst length (measured in Case P) to mean bursting period (measured in Case S) through the convective velocity of these bursting events measured utilizing the LCS visualizations.

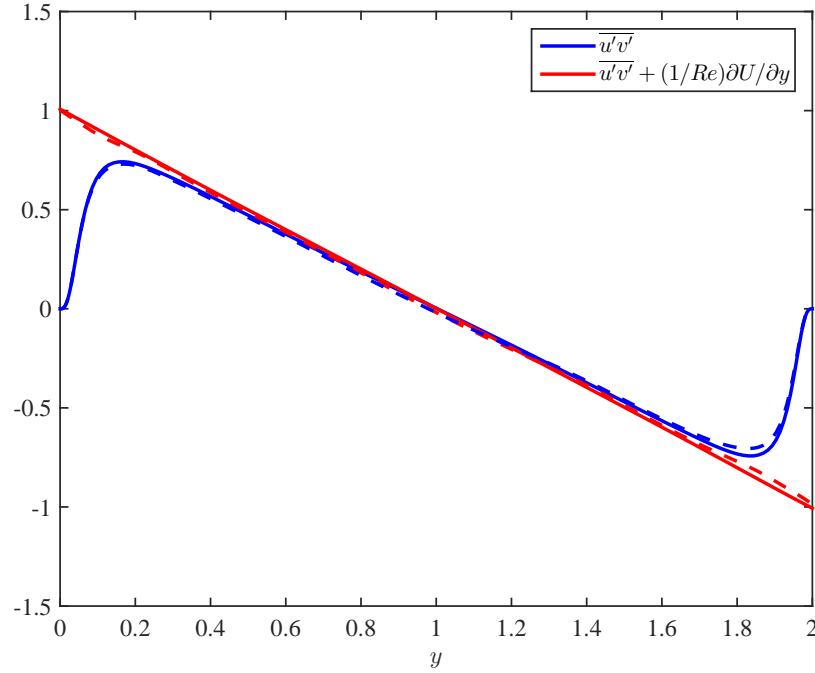


Figure 5.7: Comparison of shear stress distributions $\overline{u'v'}$ and total shear τ across the channel between Case P (solid lines) and Case S (dashed lines).

5.3.1 Identification of Bursts in the Periodic Channel

The identification of the bursting events is carried out for Case P. Here, we use the quadrant technique in which we identify second quadrant events $(\overline{u'v'})_2$ in an (x, z) plane at $y^+ \approx 20$. Here, an ejection or burst is identified when

$$|(\overline{u'v'})_2| \geq H u'_{rms} v'_{rms} \quad (5.5)$$

where H is a threshold parameter. In the literature, this parameter can generally vary between $0.25 \leq H \leq 1.25$ and in this range there is an approximately 7% variation in the number of burst detections (Luchik and Tiederman, 1987). Thus, we select the threshold parameter $H = 1$ which is consistent with the previous experimental (Bogard and Tiederman, 1986; Luchik and Tiederman, 1987) and numerical (Kim and Spalart, 1987) studies that used this technique to identify bursts or ejection events in turbulent channel flows. Here, we take instantaneous velocity fields in an (x^+, z^+) plane and if Eq. 5.5 is satisfied with the specified threshold parameter H , a burst event

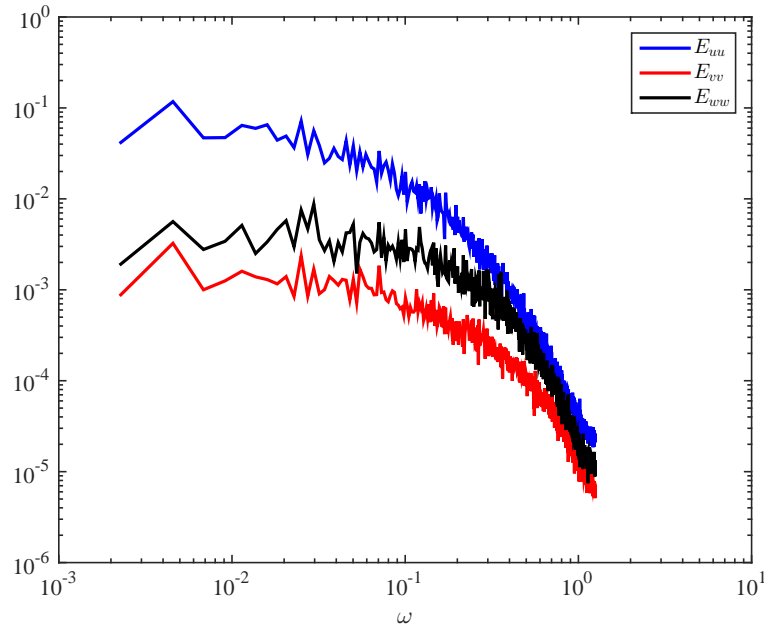


Figure 5.8: Energy spectra of Case S for the streamwise E_{uu} , wall-normal E_{vv} , and spanwise E_{wv} velocity components at $x^+ = 628$ and $y^+ = 21.2$

is identified and is marked on an instantaneous “burst plane” (figure 5.9).

It is apparent from this figure that the structure of near-wall turbulence is captured quite well when using the current criterion, where these burst events have a streamwise length of approximately $1000\nu/u_\tau$ and a spanwise spacing of approximately $100\nu/u_\tau$ which is consistent with previous measurements (Kim and Spalart, 1987). Measurement of the streamwise (x) distance between burst events in these instantaneous burst planes are carried out at each spanwise (z) location and averaged in that direction. Therefore, for every instantaneous burst plane, an average streamwise distance between bursts l_{bw}^+ is measured. Averaging is then carried out in time over approximately 224 eddy turnover cycles and 140 instantaneous data sets. Using this averaging technique, the average streamwise stance between bursts $l_b^+ \approx 604$. This is in excellent agreement with the measurements of Kim and Spalart (1987) who reported $l_{bw}^+ \approx 600$ for three Reynolds numbers $Re_\theta = 300, 670, \text{ and } 1410$ in a flat-plate boundary layer simulation, where l_b^+ was found to be invariant with respect to Re_θ . It appears that in a periodic model for both turbulent channel

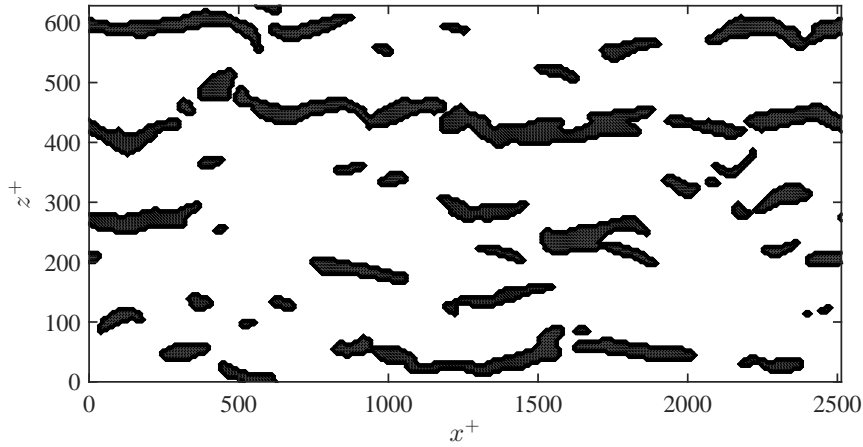


Figure 5.9: Instantaneous burst plane for Case P at $t = 1864$ and $y^+ \approx 15$; black segments represent a bursting event satisfying Eq. 5.5.

flows and flat-plate boundary layers, the average distance between bursts l_{bw}^+ is the same and is roughly half the total length of the streamwise streaky structures.

5.3.2 Identification of Bursts in the Spatial Channel

The identification of spatiotemporal bursting events is carried out for Case S. Here, the second-quadrant technique is employed to identify bursts (Eq. 5.5) where the threshold parameter $H = 1$, which is identical to the burst detection method used for the streamwise-periodic channel (section 5.3.1). Therefore, a direct comparison between the spatial and periodic channel flow models can be made. Previous experimental studies (Luchik and Tiederman, 1987; Alfredsson and Johansson, 1984; Bogard and Tiederman, 1986) used single-point velocity measurements at specific streamwise, spanwise, and wall-normal coordinates in their measurements. An advantage of DNS, then, is that high-fidelity measurements in all principle directions and time can be made for all

components of the velocity field. Therefore, the detection of bursting events and corresponding visualizations can be made in full (x, y) planes. In this case, instantaneous (x, y) planes at various spanwise (z) locations are used to detect the bursting events, in which both Eq. 5.5 and visualizations using LCS are used to identify both the coherent structures associated with the bursting phenomena, as well as measurement of the mean bursting period T_b^+ , the mean period between bursts T_{bw}^+ and convection velocity U_b^+ of the bursts, all scaled with the wall variables. An example

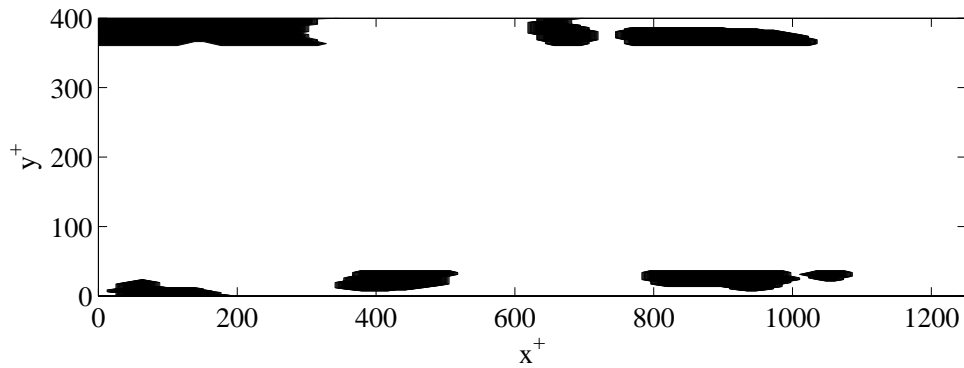


Figure 5.10: Instantaneous burst plane for Case P at $t = 1864$ and $y^+ \approx 20$; black segments represent a bursting event satisfying Eq. 5.5.

of a bursting event detected using Eq. 5.5 in an $(x^+ - y^+)$ plane at $z^+ = 311$ is presented in figure 5.10. Here, a bursting event is denoted by shaded black areas, and are detected on both the top and bottom walls. In previous studies, Eq. 5.5 has been used to identify bursting events near the plane of peak production $15 \leq y^+ \leq 23$. For visualization, an upper boundary for y^+ in which a burst can be detected is set which is apparent in figure 5.10 where no bursts are detected when $y^+ \geq 30$. However, when computing T_b^+ , T_{bw}^+ , and U_b^+ , a burst may only be counted if and only if it occurs between $15 \leq y^+ \leq 26$ on the lower wall.

Figure 5.11 shows how T_b^+ and T_{bw}^+ change as a function of detection point in the y^+ direction. Here, as the detection location moves further from the wall, the mean bursting period and time between bursts decrease monotonically. This shows the dependence of the bursting frequency on the detection plane, which would explain the variances in this bursting frequency reported in various

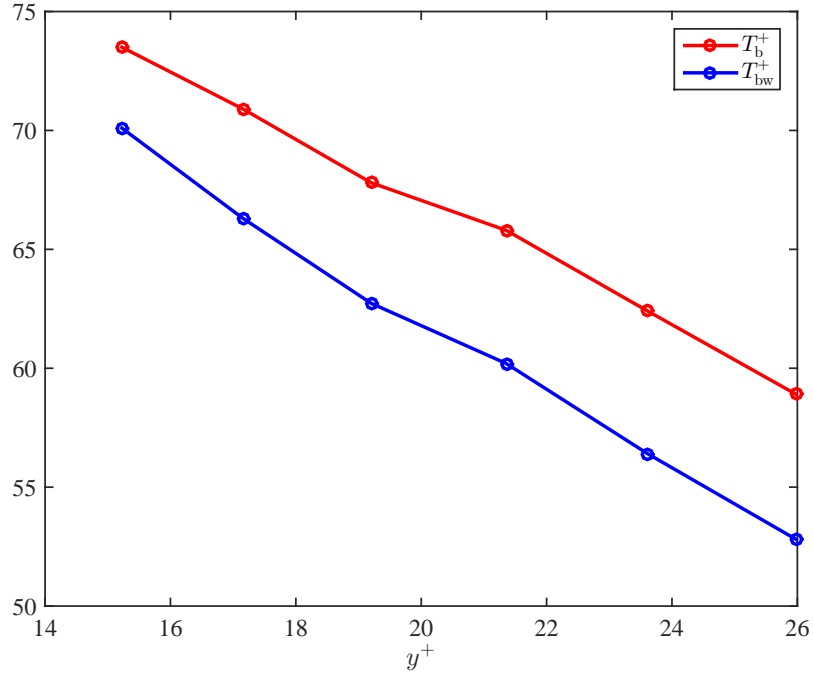


Figure 5.11: Bursting period T_b^+ and time between bursts T_{bw}^+ as a function of detection location

sources. In a majority of the studies conducted previously (Kim and Spalart, 1987; Luchik and Tiederman, 1987; Bogard and Tiederman, 1986; Blackwelder and Haritonidis, 1983), the goal was to determine the Reynolds number dependency on the bursting frequency, and not on the absolute bursting period. Therefore, their results are independent of the burst detection technique, flow field, or sensing plane location as long as these remain constant between flows.

We estimate the average bursting period and time between bursts is $T_b^+ \approx 63$ and $T_{bw}^+ \approx 57$, respectively, when averaged at points in the streamwise, spanwise, and wall-normal directions when $15 \leq y^+ \leq 23$. These values are somewhat lower than the values reported in Luchik and Tiederman (1987) where $T_{bw}^+ \approx 90$, although they grouped ejection events from the same “burst”. Here, we are counting ejection events as separate bursting events which would increase the number of bursts over a given time, and necessarily decrease the bursting period. However, the agreement with Kim and

Spalart (1987) is quite good, where they report a value of $T_{bw}^+ \approx 60$ by using Taylor's hypothesis

$$T_{bw}^+ = \frac{l_{bw}^+}{U_b^+} \quad (5.6)$$

to convert the average streamwise distance between bursts l_{bw}^+ using $U_b^+ \approx 10$. However, we calculate the convection velocity of the bursting event to be $U_b^+ \approx 15$ in our spatial case, which is higher than the value reported by Kim and Spalart (1987). Transforming our average streamwise spacing between bursts $l_b^+ \approx 600$ through Eq. 5.6 using $U_b^+ \approx 15$, we then expect a value of $T_{bw}^+ \approx 40$ when transforming from a periodic to a spatial turbulent channel. This is somewhat lower than the value of T_{bw}^+ directly measured in the spatial channel, which can be attributed to the discrepancy in the measured values of U_b^+ . The value of $U_b^+ \approx 10$ reported in Kim and Spalart (1987) was for a boundary layer flow, where we report $U_b^+ \approx 15$ in a channel flow. This discrepancy may be attributed to the intermittency in the boundary layer as opposed to a channel flow, and may have an effect on the convection speed of these bursting events.

Because bursting events are responsible for the production of turbulence (Kim et al., 1971; Lu and Willmarth, 1973), one would expect that these frequencies should fall in the inertial subrange of the energy spectra. Here, the upper and lower range of T_b^+ in figure 5.11 is superimposed on the energy spectra for the spatial channel and is shown in figure 5.12, where the dashed lines indicate the upper and lower boundaries of T_b^+ . Here, it is apparent that the range of turbulent bursting frequency falls in the inertial range of the energy spectra, where the turbulent production is balanced by turbulent dissipation (Pope, 2008). This confirms the fact that the bursting phenomena operates on the inertial scales, and in future studies the range of bursting frequency can be predicted using the energy spectra of a specific flow.

5.3.3 Visualization of turbulent flow structures using LCS

Lagrangian Coherent Structures (LCS) are defined as ridges in forward finite time Lyapunov exponent (FTLE) fields. LCS represent barriers to transport (Shadden, Lekien, and Marsden, 2005) and can be used to identify vortex boundaries for a visual characterization of the flow field. LCS

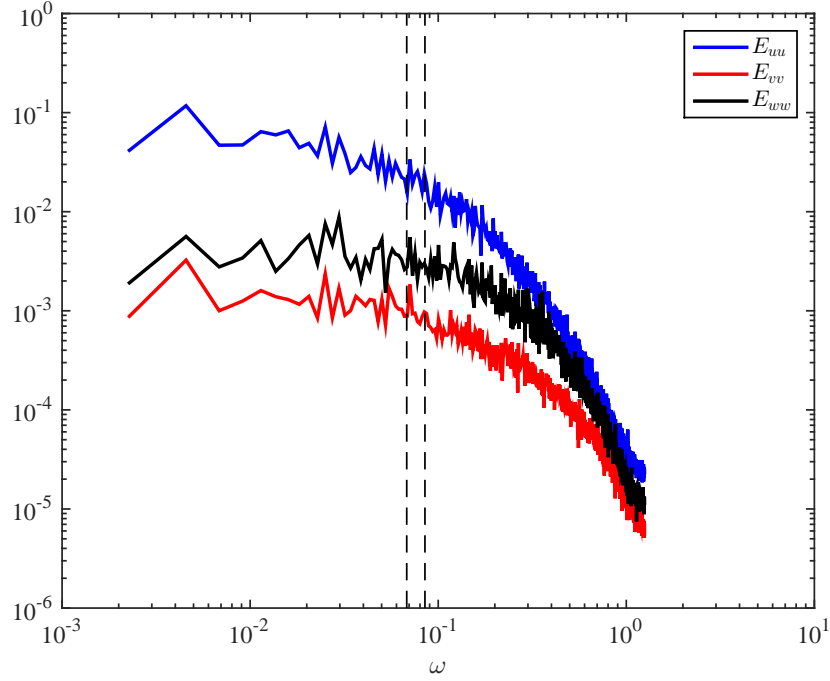


Figure 5.12: Energy spectra of Case S for the streamwise E_{uu} , wall-normal E_{vv} , and spanwise E_{wv} velocity components at $x^+ = 628$ and $y^+ = 21.2$ superimposed with the range of bursting frequency T_b^+ reported in figure 5.11.

have been used as a visualization tool in a variety of flow fields (Voth, Haller, and Gollub, 2002; Shadden, Lekien, Paduan, Chave, and Marsden, 2009; Lipinski and Mohseni, 2010). To accomplish this, we take an existing set of Eulerian discrete velocity fields from our simulation data (in both time and space) and advect particles in a Lagrangian fashion to generate the FTLE. The FTLE is rather insensitive to the accuracy of the velocity field data (Haller, 2002) which is an advantage for this particular simulation. However, the FTLE is sensitive to the integration time τ , and with proper adjustment, coherent structures may be observed. The FTLE is defined as

$$\Phi_T^{T+\tau}(\mathbf{x}) = \mathbf{x}(T) + \int_T^{T+\tau} \mathbf{v}(\mathbf{x}(t))dt \quad (5.7a)$$

$$\Delta = \left(\frac{d\Phi}{d\mathbf{x}} \right) * \left(\frac{d\Phi}{d\mathbf{x}} \right) \quad (5.7b)$$

$$\sigma_T^\tau(\mathbf{x}) = \frac{1}{\tau} \ln \sqrt{\gamma_{max}(\Delta)} \quad (5.7c)$$

where σ is the FTLE and $\gamma_{max}(\Delta)$ is the maximum eigenvalue of the Cauchy-Green deformation tensor Δ , which is calculated for each point based on the deformation of the tracer mesh Φ (Lipinski and Mohseni, 2010). Also, T represents the initial time the tracer particles are advected. Note that the direction of integration depends on the sign of τ and represents either a forward or backward FTLE when τ is positive or negative, respectively.

It is important to note that the generation of LCS can be a rather computationally demanding process, however recent developments in ridge-tracking algorithms (Lipinski and Mohseni, 2010) can alleviate this cost. Because FTLE fields define vortex boundaries (Shadden, Dabiri, and Marsden, 2006), they are ideally suited for use in the observation of bursting events due to the large vortical nature of these flow structures. To this end, the integration time τ for the following LCS has been chosen such that coherent structures can be delineated with sharp boundaries. Here, we demonstrate the applicability of forward FTLE contours to detect bursting events, shown in a time sequence of instantaneous forward FTLE contours in the (x^+, y^+) plane at $z^+ = 311$ shown in figure 5.13. The contour levels are somewhat trivial, and instead are chosen to highlight packets of particles which have high FTLE magnitudes and thus represent vortical boundaries. The structure of the bursting event is captured remarkably well where the streamwise streaky-structures first begin to lift away from the wall and tilt in the wall-normal direction. These streamwise streaks are then ejected from the wall and into the outer layer which can be identified as a burst. We also capture part of a “sweep” event as well, where the ejected structure begins to tilt down towards the wall, where it will be recirculated into the wall layer to replace the fluid lost to the ejection event. This time-sequence visualization is a remarkable demonstration of the bursting event and correlates well with the second quadrant detection method $(\overline{u'v'})_2$ used to detect bursts, as shown in figure 5.14. The agreement between the second quadrant bursting event detection technique (Eq. 5.5) with the LCS visualization is in agreement with the experimental studies of Luchik and Tiederman (1987). In this figure, each bursting event detected correlates well with the tilting and ejections observed in the visualizations. In addition, the downstream propagation of these events match very well with the visualizations where tracking both the second quadrant events (figure 5.14(b))

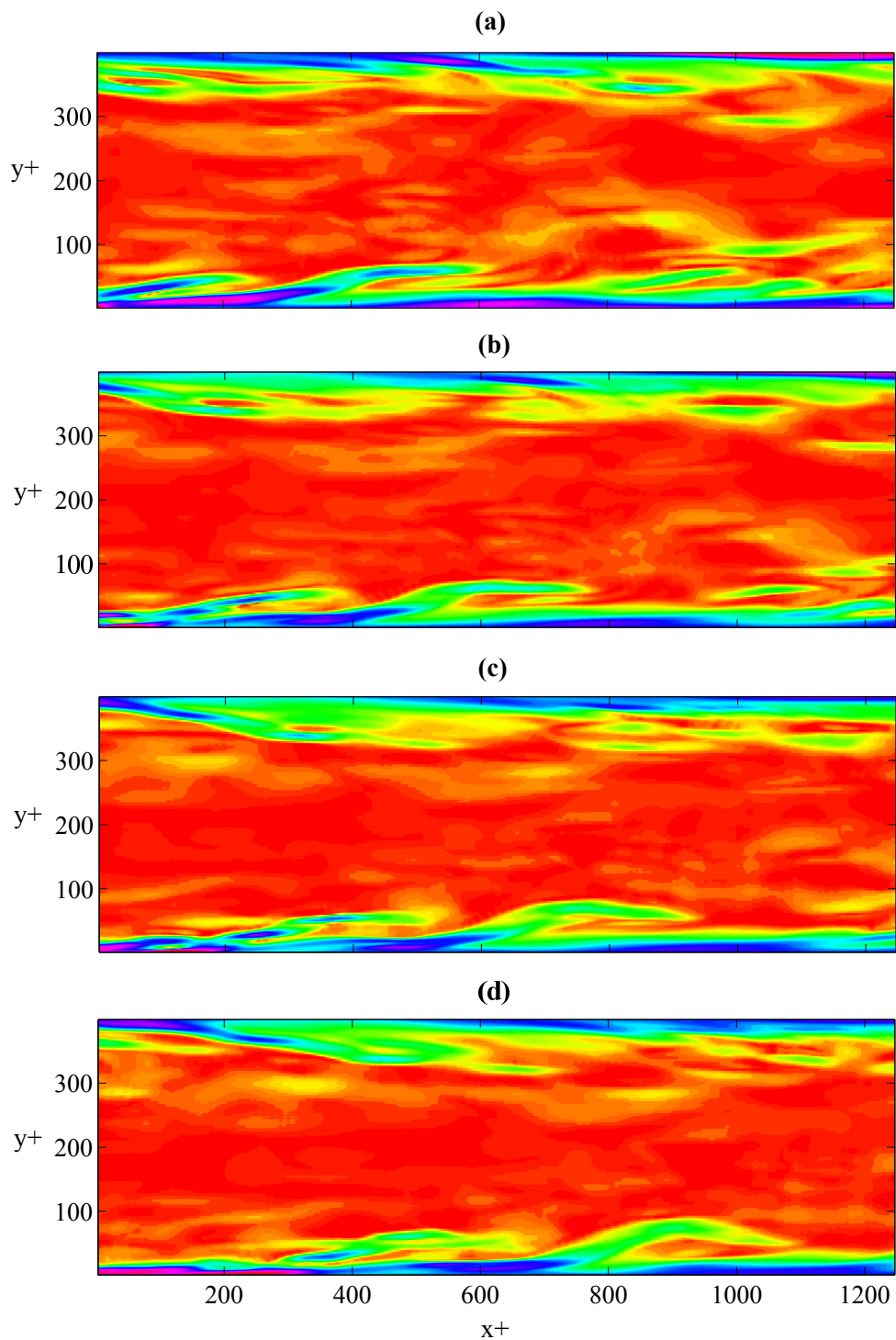


Figure 5.13: Time-sequence of instantaneous forward FTLE contours in the (x^+, y^+) plane at $z^+ = 311$ (a) $t^+ = 8000$; (b) $t^+ = 8010$; (c) $t^+ = 8020$; (d) $t^+ = 8030$.

and the structures detected through LCS (figure 5.14(a)) yield the same convection velocity of the

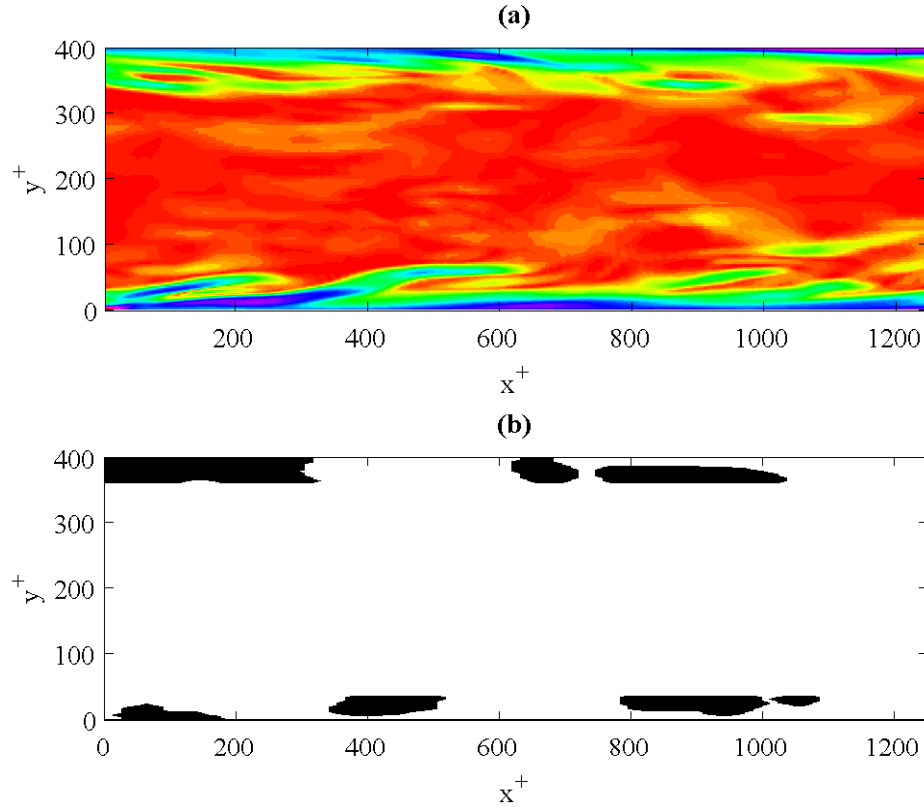


Figure 5.14: Demonstration of LCS and bursting detection technique in the (x^+, y^+) plane at $z^+ = 311$ and $t^+ = 8000$ (a) forward FTLE contours; (b) second quadrant technique.

bursts U_b^+ .

LCS visualizations using forward FTLEs for the spatial turbulence case is presented in figure 5.15(a) in the (x^+, z^+) plane and figure 5.15(b) in the (z^+, y^+) plane. In the (x^+, z^+) plane, the visualizations show the streaky structures elongated in the streamwise direction. Here, the spacing of these streaky-structures in the spanwise z^+ direction is approximately $100\nu/u_\tau$ and the streamwise extent of the structures are approximately $1000\nu/u_\tau$, which is in agreement with previous experimental visualizations (Kline et al., 1967; Kim et al., 1971). In figure 5.15(b), counter-rotating vortical structures are observed on the top and bottom walls and their location correspond with the elongated streamwise structures observed in figure 5.15(a). That is, the observed pairs of streamwise vortices are responsible for both the transfer of low-speed fluid near the wall (ejection

events) to the outer layer and the transport of high speed fluid from the outer layer towards the wall (sweep events). This demonstrates the highly vortical nature of the flow structures near the wall. Thus, we have shown the ability of LCS to capture and identify the coherent structures in turbulent channel flows that are responsible for the production of turbulent energy.

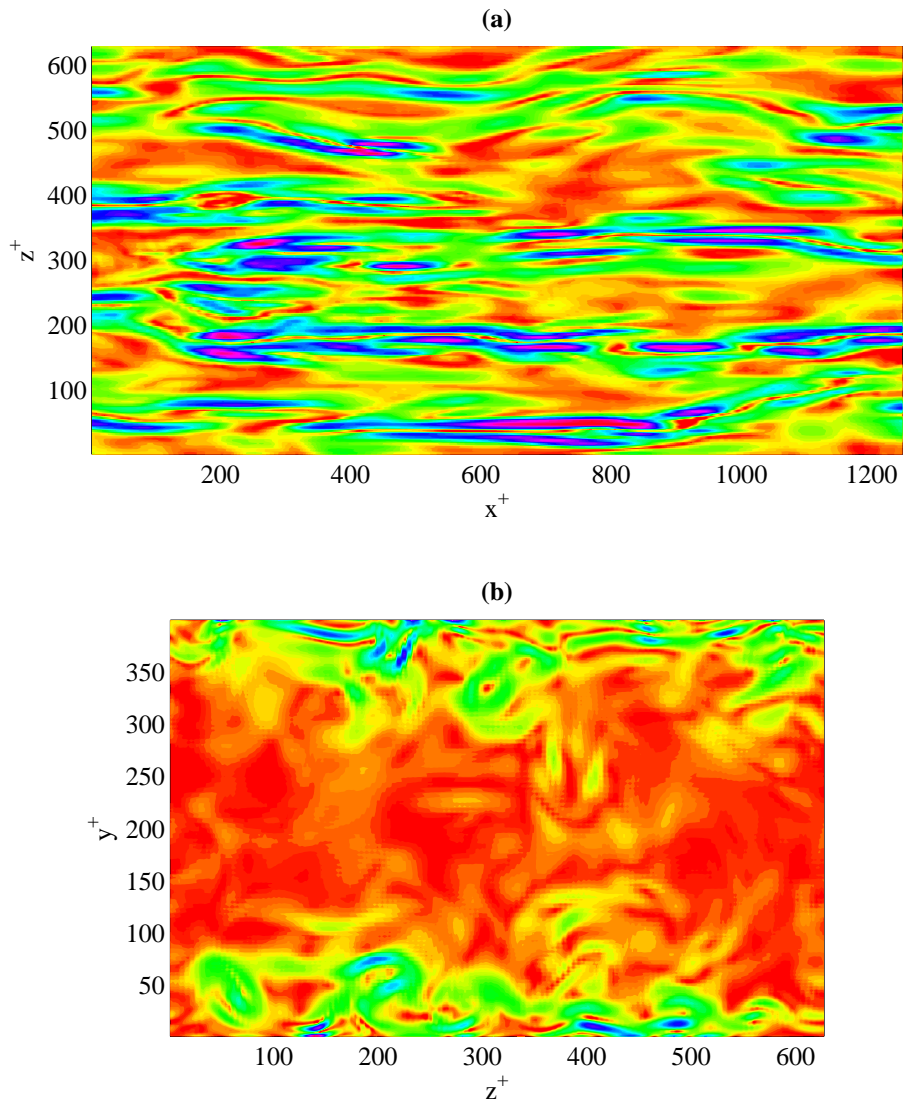


Figure 5.15: Forward FTLEs at $t^+ = 8000$ for (a) (x^+, z^+) plane at $y^+ = 21.2$; (b) (z^+, y^+) plane at $x^+ = 618$

5.4 Summary and Conclusions

Here, we have presented a DNS of a turbulent flow for both temporally (Case P) and spatially (Case S) developing channels at a Reynolds number $Re_\tau = 200$. Once Case P converged to a statistical steady state, a method whereby (z, y) planes from this simulation were sampled at high fidelity over 240 eddy turnover cycles and used as inflow conditions for Case S. In general, good agreement between the periodic and spatial mean and perturbation statistics was found and verified the inflow sampling technique employed here to simulate a spatially evolving turbulent channel.

Once Case S was verified, a burst detection method based on a second quadrant $(\overline{u'v'})_2$ technique was used to detect bursts in both the periodic and spatial channel near the location of peak production. For the periodic channel, there was excellent agreement with a previous DNS of parallel boundary layer flow (Kim and Spalart, 1987) where the average spacing between bursts was $l_b^+ \approx 600$ for both simulations. For the spatial channel, both the bursting period and time between bursts were calculated using the same technique, where the average bursting time and time between bursts was $T_b^+ \approx 63$ and $T_{bw}^+ \approx 57$, respectively. The convection velocity of the structures associated with the bursting events was measured in the spatial channel and found to be approximately $U_b^+ \approx 15$ which is higher than the value reported in the turbulent boundary layer computations by Kim and Spalart (1987) and experiments by Lu and Willmarth (1973) where $U_b^+ \approx 10$. This discrepancy might stem from the intermittency in the boundary layer compared to a channel flow due to the fact that these structures are violently ejected into the outer layer, however further studies need to be conducted to cast further light on this discrepancy.

Finally, forward FTLEs were used to visualize Lagrangian Coherent Structures in the turbulent flow for Case S. There was a rather strong correlation between the visualized ejection events and ejections that were detected using the second quadrant technique, validating both the detection method as well as the visualization. Overall, the FTLEs were able to capture the structure of turbulence in the channel reasonably well, where long streamwise streaky-structures were detected along with pairs of counter-rotating vortices which are responsible for the mixing of low-

and high-speed fluid to and from the outer layer, respectively.

Chapter 6

Conclusions and Recommendations

The focus of this thesis was on the control of instabilities in channel flow utilizing both active and passive methods utilizing direct numerical simulation. For passive flow control, a fluid/structure interaction problem was solved between a channel flow and a phononic structure. Both methods of flow control were found to induce a substantial reduction in the perturbations in the channel, which in general consisted mostly of Tollmien-Schlichting (TS) waves. In addition, flow visualization using Lagrangian Coherent Structures was carried out for various scenarios, elucidating the structure of both nonlinear transition and turbulent flows in the near-wall region.

6.1 Overview

A channel flow in transition was modeled using direct numerical simulation, where disturbances were introduced at the inflow and allowed to propagate downstream as a spatial model for transition. The shape of the disturbances introduced at the inflow were obtained by an auxiliary program which solved the complex, fourth-order eigenvalue problem known as the Orr-Sommerfeld equation for spatially evolving disturbances and are known as Tollmien-Schlichting (TS) waves. The propagation of these waves were accurately captured using our numerical model, and served as a basis for both the active and passive control cases presented in this thesis.

A natural transition scenario was investigated where random disturbances were superimposed on the TS wave at the inflow and allowed to propagate downstream. A strong dependence on the amplitude of the TS wave was found on the growth rates of the three-dimensional disturbances in

the channel. For this scenario we employed an active control strategy to reduce the growth of the TS wave, whereby a portion of the wall was replaced with a suction/blowing slot tuned to the frequency of the disturbance wave. It was shown that the correlations between the streamwise and wall-normal velocity components were altered, thereby destroying the shear stress and, consequently, the turbulent production term in the energy balance. These changes caused a whole-scale reduction in the total perturbation energy in the channel, thereby delaying transition.

A natural extension of this active control method was to utilize a passive control method, whereby a phononic subsurface would replace a portion of the bottom wall and institute changes in the perturbation energy production term by altering the phase relationship between the interface pressure and velocity, thereby delaying transition with no energy cost. We have demonstrated that a properly designed phononic subsurface can be used to reduce the perturbation energy in a channel flow locally, where the disturbances can be linear or three-dimensional and no spurious modes are excited to destabilize the flow. In addition, common materials were used (plastic and aluminum) and the displacements at the interface remained small in order to avoid the spurious wall modes found in other passive control methods (namely compliant surfaces). The uncoupled design methodology developed in this collaborative research allowed for the accurate and repeatable prediction of phononic subsurface performance in the presence of unstable disturbance waves in the fluid.

Finally, a spatially evolving turbulent channel flow model was also developed, and was utilized to detect bursting events in the turbulent flow. The bursting events have been found to be responsible for the majority of the turbulent production in wall-bounded shear flows. Therefore, accurate detection of these bursting events is paramount in realizing effective passive flow control techniques for turbulent flows to reduce the overall skin-friction on the wall. The structure of turbulence was elucidated through the use of a flow visualization technique known as Lagrangian Coherent Structures (LCS), whereby turbulent bursting events could be detected and correlated with a more traditional quadrant-based method to detect turbulent bursts. These simulations and burst detection methods for turbulent flows can be used as a testbed for testing phononic subsur-

faces specifically designed to disrupt the bursting process and, in turn, lower the turbulent drag in a turbulent wall-bounded shear flow.

6.2 Contributions

- A fully parallelized direct numerical simulation code was developed for spatially evolving flows, where specification of the inflow and outflow boundary conditions was of paramount importance in realizing accurate and efficient simulations of channel flow undergoing linear and nonlinear transition. Here, we utilized fourth order finite-differences in all principle directions with a “sponge” layer used in the outflow region to prevent reflection of spurious modes back into the physical domain. This code was parallelized using the PETSc MPI libraries exhibiting excellent strong scaling with up to 10,000 unknowns per processor.
- Developed methods of active flow control using a suction/blowing slot whereby the phase and amplitude tuning of the slot via the pressure signal on the wall coerced a drastic reduction in the perturbation kinetic energy in a flow undergoing rapid three-dimensional transition, mimicking a natural laboratory experiment. In addition, this method was found to be efficient whereby the energy reduced in the channel exceeds the cost of actuating the control slot.
- Coupled, for the first time, a channel flow to a phononic structure whereby a serial-staggered algorithm was employed to ensure the continuity of shear stress and velocity at the fluid/structure interface. This coupling method was parallelized using the standard MPI libraries, maintaining high-efficiency in both codes allowing for rapid parametric studies to be undertaken in pursuit of consistent and repeatable phononic subsurface design methodologies for both transitional and turbulent flows.
- Developed, in collaboration with Prof. Hussein’s team, a theory of phononic subsurfaces to locally reduce the perturbation energy in a channel flow undergoing both linear and nonlinear transition. The subsurface was precisely tuned to affect the pressure/velocity

phase relations at the interface which permeates into the flow, causing changes in the local energy production that, on average, leads to a drastic reduction in the perturbation energy localized at the fluid/structure interface. Here, we were able to control a single TS wave, a flow with multiple excitation frequencies, and flows with three-dimensional instabilities, where the uncoupled design methodology was accurate, consistent, and repeatable allowing for rapid generation of effective phononic subsurface designs.

- Implemented the flow visualization method of Lagrangian Coherent Structures which utilize finite-time Lyapunov exponents to observe the characteristic structures in both nonlinear transition and fully-developed turbulent flows. In addition, this visualization method was found to correlate well with the more traditional quadrant based technique used to identify the bursting events in a turbulent channel flow, which are responsible for a majority of the turbulent energy production in the near-wall region.
- A fully-developed spatially evolving turbulent channel flow model was developed to identify the bursting events characteristic of wall-bounded shear flows. Here, we utilized crossflow planes sampled at high-fidelity in an auxiliary periodic channel flow simulation as inflow conditions in the spatial model, where excellent agreement in the mean and lower order momentum statistics was observed. Using these flow fields, we were able to identify a range of bursting frequencies in the channel which can be used in the design of a phononic subsurface to control these events, and perhaps lower the overall skin-friction in the channel.

6.3 Recommendations

- Extend the capabilities of the spatial DNS code to handle flows with rotation on arbitrary axes as well as support for flat-plate and accelerating/decelerating boundary layer flows. Also, include support for three-dimensional boundary layers to more accurately represent real flows over swept airplane wings as well as accounting for compressibility effects at transitional Mach numbers in which commercial airlines operate at. This will greatly

enhance the capabilities of the solver as well as introducing new base flows to study the influence of a phononic subsurface on these relatively complex flow fields.

- Introduce more advanced coupling schemes between the fluid and phononic surface to account for large surface deformations. Perhaps using more advanced methods such as immersed boundary methods, sharp-interface methods, or coordinate transformations to account for large amplitude disturbances at the fluid/structure interface. As of now, the coupling scheme relies on utilizing first-order Taylor approximations and are only accurate when the deformations are small. In general, small motion is sufficient because the control concept is based on phase control and not large interface motion. However, these deformations may not remain small in some cases, for example in certain flight conditions or when compressibility effects are introduced such as shock waves or expansion fans.
- Explore the effect of a phononic subsurface in more advanced stages of transition, especially when considering bypass transition and secondary instability mechanisms (for instance, the Klebanoff mode) when the disturbances in the freestream are high-amplitude and contain large amounts of rotation. That is, explore transition scenarios in which the TS mode is not the main path of transition in the boundary layer, or when there is a competition of other modes through receptivity processes.
- Study the effect of subgrid scaling and closure modeling either using RANS or Large-Eddy Simulation (LES) and how these models interact with the basic physics of the phononic subsurface. This is important in realizing more realistic flows at high Reynolds numbers which become unfeasible for direct numerical simulation, especially when concerning turbulent flows over complex geometries.
- Use the phononic subsurface to reduce the turbulent drag on the wall. This can be realized utilizing two distinct control methods. The first method would be to allow for the surface deformations to become finite in an attempt to reduce pressure drag by controlling the

shape of the deformation at the fluid/structure interface. The second method would be to keep the deformations small and control the overall turbulent skin-friction drag at the fluid/structure interface by designing a subsurface to affect the most dangerous frequencies in the turbulent flow. It is the opinion of the author that the most dangerous frequency in the flow, as elucidated in this thesis as well in other studies, is the bursting frequency which has a large contribution to the production of turbulent energy. It may be possible to design a phononic subsurface to attack this frequency and disrupt the bursting process, thereby relaminarizing the mean flow and reducing the skin friction.

Bibliography

- Albrecht, T., Aetzkes, H., Grundmann, R., Mutschke, G., Gerbeth, G.: Tollmien-Schlichting Wave Damping by a Streamwise Oscillating Lorentz Force. *Magneto hydrodynamics* **44**, 205–222 (2008)
- Alfredsson, P.H., Johansson, A.V.: Time scales in turbulent channel flow. *Physics of Fluids* **27** (1984)
- Aljallis, E., Sarshar, M.A., Datla, R., Sikka, V., Jones, A., Choi, C.H.: Experimental study of skin friction drag reduction on superhydrophobic flat plates in high Reynolds number boundary layer flow. *Physics of Fluids (1994-present)* **25**(2), 025,103 (2013)
- Anderson, D.A., Tannehill, J.C., Pletcher, R.H.: *Computational Fluid Mechanics and Heat Transfer*. Hemisphere Publishing Corporation, New York, New York (1984)
- Andersson, P., Berggren, M., Henningson, D.S.: Optimal disturbances and bypass transition in boundary layers. *Physics of Fluids (1994-present)* **11**(1), 134–150 (1999)
- Ashpis, D., Reshotko, E.: The Vibrating Ribbon Problem Revisited. *J. Fluid Mech.* **213**, 531–547 (1990)
- Barkley, D.: Theory and predictions of finite-amplitude waves in two-dimensional plane Poiseuille flow. *Phys. Fluids A* **6**, 955–970 (1990)
- Baumann, M., Nitsche, W.: Investigation of active control of Tollmien-Schlichting waves on a wing. *Transitional boundary layers in aeronautics* **46**, 89–98 (1996)
- Benjamin, T.B.: Effects of a flexible boundary on hydrodynamic stability. *J. Fluid Mech.* **9**(04), 513–532 (1960)
- Benjamin, T.B.: The threefold classification of unstable disturbances in flexible surfaces bounding inviscid flows. *J. Fluid Mech.* **16**(03), 436–450 (1963)
- Berger, T.W., Kim, J., Lee, C., Lim, J.: Turbulent boundary layer control utilizing the Lorentz force. *Physics of Fluids (1994-present)* **12**(3), 631–649 (2000)
- Bewley, T.R., Moin, P., Teman, R.: DNS-based predictive control of turbulence: An optimal target for feedback algorithms. *J. Fluid Mech.* **447**, 179 (2001)
- Bilal, O.R., Hussein, M.I.: Ultrawide phononic band gap for combined in-plane and out-of-plane waves. *Physical Review E* **84**(6), 065,701 (2011)

- Biringen, S.: Active control of transition by periodic suction-blowing. *Physics of Fluids* **27**(6), 1345–1347 (1984)
- Biringen, S., Nutt, W.E., Caruso, M.J.: Numerical Study of Transition Control by Periodic Suction Blowing. *AIAA Journal* **25**(2), 239–244 (1987)
- Blackwelder, R.: The bursting process in turbulent boundary layers. *Coherent Structure of Turbulent Boundary Layers*. Edited by CR Smith and DE Abbott. AFOSR/Lehigh University, Bethlehem, Penn (1978)
- Blackwelder, R., Haritonidis, J.: Scaling of the bursting frequency in turbulent boundary layers. *J. Fluid Mech.* **132**, 87–103 (1983)
- Blackwelder, R.F., Kaplan, R.E.: On the bursting phenomenon near the wall in bounded turbulent shear flows. *J. Fluid Mech.* **76**, 89 (1976)
- Bogard, D.G., Tiederman, W.G.: Burst detection with single-point velocity measurements. *J. Fluid Mech.* **162**, 389 (1986)
- Borodulin, V.I., Kachanov, Y.S., Koptsev, D.B.: Experimental study of resonant interactions of instability waves in a self-similar boundary layer with an adverse pressure gradient: I. Tuned resonances. *Journal of Turbulence* p. N62 (2002)
- Brillouin, L.: Wave propagation in periodic structures. electric filters and crystal lattices, ser. international series in pure and applied physics (1946)
- Carpenter, P., Garrad, A.: The hydrodynamic stability of flow over Kramer-type compliant surfaces. part 1. Tollmien-Schlichting instabilities. *J. Fluid Mech.* **155**, 465–510 (1985)
- Carpenter, P., Garrad, A.: The hydrodynamic stability of flow over Kramer-type compliant surfaces. part 2. Flow-induced surface instabilities. *J. Fluid Mech.* **170**, 199–232 (1986)
- Carpenter, P.W., Lucey, A.D., Davies, C.: Progress on the use of compliant walls for laminar-flow control. *Journal of Aircraft* **38**(3), 504–512 (2001)
- Chang, Y., Collis, S., Ramakrishnan, S.: Viscous effects in control of near-wall turbulence. *Physics of Fluids* **14**, 4069–4080 (2002)
- Choi, H., Moin, P., Kim, J.: Active turbulence control for drag reduction in wall-bounded flows. *J. Fluid Mech.* **262**, 75 (1994)
- Choi, J.I., Xu, C.X., Sung, H.J.: Drag reduction by spanwise wall oscillation in wall-bounded turbulent flows. *AIAA journal* **40**(5), 842–850 (2002)
- Choi, K.S., Yang, X., Clayton, B., Glover, E., Atlar, M., Semenov, B., Kulik, V.: Turbulent drag reduction using compliant surfaces. *Proceedings of the Royal Society of London. Series A: Mathematical, Physical and Engineering Sciences* **453**(1965), 2229–2240 (1997)
- Chung, Y., Sung, H.: Comparative Study of Inflow Conditions for Spatially Evolving Simulation. *AIAA Journal* **35-2**, 269–274 (1997)
- Corino, E., Brodkey, R.S.: A visual study of turbulent shear flow. *J. Fluid Mech.* **37**, 1 (1969)

- Danabasoglu, G., Biringen, S., Streett, C.L.: Spatial simulation of instability control by periodic suction blowing. *Physics of Fluids A* **3**(9), 2138–2147 (1991)
- Davies, C., Carpenter, P.W.: Numerical simulation of the evolution of Tollmien–Schlichting waves over finite compliant panels. *J. Fluid Mech.* **335**, 361–392 (1997)
- Deymier, P.A.: Introduction to Phononic Crystals and Acoustic Metamaterials. In: *Acoustic Metamaterials and Phononic Crystals*, pp. 1–12. Springer (2013)
- DiPrima, R., Swinney, H.: Instabilities and Transition in Flow Between Concentric Rotating Cylinders. In: Swinney, H.L., Gollub, J.P. (eds.) *Hydrodynamic Instabilities and the Transition to Turbulence*, pp. 139–180. SpringerVerlag, Berlin (1985)
- Du, Y., Karniadakis, G.E.: Suppressing wall turbulence by means of a transverse traveling wave. *Science* **288**(5469), 1230–1234 (2000)
- Erdmann, R., Patzold, A., Engert, M., Peltzer, I., Nitsche, W.: On active control of laminar-turbulent transition on two-dimensional wings. *Phil. Trans. R. Soc. A* **369**, 1382–1395 (2011)
- Falco, R.: Some comments on turbulent boundary layer structure inferred from the movements of a passive contaminant. *AIAA paper* **74**, 99 (1974)
- Farhat, C., Lesoinne, M.: Two efficient staggered algorithms for the serial and parallel solution of three-dimensional nonlinear transient aeroelastic problems. *Computer methods in applied mechanics and engineering* **182**(3), 499–515 (2000)
- Förster, C., Wall, W., Ramm, E.: The artificial added mass effect in sequential staggered fluid-structure interaction algorithms. In: *Proceedings European Conference on Computational Fluid Dynamics ECCOMAS CFD* (2006)
- García-Mayoral, R., Jiménez, J.: Drag reduction by riblets. *Philosophical Transactions of the Royal Society A: Mathematical, Physical and Engineering Sciences* **369**(1940), 1412–1427 (2011)
- Gedney, C.J.: The Cancellation of a Sound-Excited Tollmien-Schlichting Wave with Plate Vibration. *Phys. Fluids*. **26**, 1158–1160 (1983)
- Gad-el Hak, M.: Compliant coatings for drag reduction. *Progress in Aerospace Sciences* **38**(1), 77–99 (2002)
- Gad-el Hak, M., Pollard, A., Bonnet, J.: *Flow Control: Fundamentals and Practices*. Springer (1998)
- Gad-el Hak, M., Tsai, H.M.: *Transition and Turbulence Control*. World Scientific (2006)
- Haller, G.: Lagrangian Coherent Structures from approximate velocity data. *Physics of Fluids* **14**, 1851–1861 (2002)
- Herbert, T.: Secondary instability of plane channel flow to subharmonic 3-dimensional disturbances. *Physics of Fluids* **26**, 871–874 (1983)
- Herbert, T.: Secondary instability of boundary layers. *Ann. Rev. of Fluid Mechanics* **20**, 487–526 (1988)

- Hosseini, S.M., Hanifi, A., Henningson, D.: Effect of low freestream turbulence on crossflow instability. *Bulletin of the American Physical Society* **58** (2013)
- Hsieh, A., Biringen, S., Kucala, A., Waggy, S.: Use of DNS Data for the Evaluation of Closure Models in Spanwise-Rotating Turbulent Channel Flow. In Preparation (2014)
- Hussein, M.I.: Theory of damped bloch waves in elastic media. *Physical Review B* **80**(21), 212,301 (2009)
- Hussein, M.I., Biringen, S., Bilal, O.R., Kucala, A.: Flow stabilization by subsurface phonons. *Proc. R. Soc. A* (2015)
- Hussein, M.I., Hamza, K., Hulbert, G.M., Scott, R.A., Saitou, K.: Multiobjective evolutionary optimization of periodic layered materials for desired wave dispersion characteristics. *Structural and Multidisciplinary Optimization* **31**(1), 60–75 (2006a)
- Hussein, M.I., Hulbert, G.M., Scott, R.A.: Dispersive elastodynamics of 1d banded materials and structures: analysis. *Journal of Sound and Vibration* **289**(4), 779–806 (2006b)
- Hussein, M.I., Hulbert, G.M., Scott, R.A.: Dispersive elastodynamics of 1d banded materials and structures: design. *Journal of Sound and Vibration* **307**(3), 865–893 (2007)
- Hussein, M.I., Leamy, M.J., Ruzzene, M.: Dynamics of phononic materials and structures: Historical origins, recent progress, and future outlook. *Applied Mechanics Reviews* **66**(4), 040,802 (2014)
- Jimenez, J., Parvis, M.: The minimal flow unit in near-wall turbulence. *J. Fluid Mech.* **225**, 213 (1990)
- Jung, W., Mangiavacchi, N., Akhavan, R.: Suppression of turbulence in wall-bounded flows by high-frequency spanwise oscillations. *Physics of Fluids A: Fluid Dynamics (1989-1993)* **4**(8), 1605–1607 (1992)
- Kachanov, Y.S.: Three-dimensional receptivity of boundary layers. *Eur. J. Mech. B. Fluids* **19**, 723–744 (2000)
- Kachanov, Y.S., Kozlov, V.V., Levchenko, V.Y.: Nonlinear development of a wave in a boundary layer. *Fluid Dynamics* **12**, 383–390 (1978)
- Kachanov, Y.S., Levchenko, V.Y.: The resonant interaction of disturbances at laminar-turbulent transition in a boundary layer. *J. Fluid Mech.* **138**, 209–247 (1984)
- von Karman, T.: Mechanische hnlichkeit und Turbulenz. In: *Proc. Third Int. Long. Applied Mechanics*, pp. 85–105 (1930)
- Karniadakis, G., Choi, K.S.: Mechanisms on transverse motions in turbulent wall flows. *Annual Review of Fluid Mechanics* **35**(1), 45–62 (2003)
- Kendall, J.M.: Experiments on boundary layer receptivity to freestream turbulence. *AIAA Paper* 98-0530 (1998)
- Kim, H.T., Kline, S.J., Reynolds, W.C.: The production of turbulence near a smooth wall in a turbulent boundary layer. *J. Fluid Mech.* **50**, 133 (1971)

- Kim, J.: Physics and control of wall turbulence for drag reduction. *Philosophical Transactions of the Royal Society A: Mathematical, Physical and Engineering Sciences* **369**(1940), 1396–1411 (2011)
- Kim, J., Moin, P., Moser, R.: Turbulence statistics in fully developed channel flow at low Reynolds number. *J. Fluid Mech.* **177**, 133–166 (1987)
- Kim, J., Moser, R.D.: On the secondary instability in plane Poiseuille flow. *Physics of Fluids A* **1**(5), 775–777 (1989)
- Kim, J., Spalart, P.R.: Scaling of bursting frequency in turbulent boundary layers at low Reynolds numbers. *Physics of Fluids* **30**, 3326 (1987)
- Klebanoff, P.S., Tidstrom, K.D., Sargent, L.M.: The three-dimensional nature of boundary-layer instability. *J. Fluid Mech.* **12**, 1–34 (1962)
- Kline, S.J., Schraub, F.A., Runstadler, P.W.: The structure of the turbulent boundary layer. *J. Fluid Mech.* **30**, 741 (1967)
- Kosorygin, V.S., H., R.R., Saric, W.S.: Laminar boundary layer sound receptivity and control. See Kobayashi 1995 pp. 517–524 (1995)
- Kovasznyai, L.S., Kibens, V., Blackwelder, R.F.: Large-scale motion in the intermittent region of a turbulent boundary layer. *J. Fluid Mech.* **41**(02), 283–325 (1970)
- Kozlov, V.V., Ramazanov, M.P.: Development of finite-amplitude disturbances in Poiseuille flow. *J. Fluid Mech.* **147**, 149–157 (1983)
- Kramer, M.O.: Boundary layer stabilization by distributed damping. *Journal of the American Society for Naval Engineers* **72**(1), 25–34 (1960)
- Kramer, M.O.: Boundary layer stabilization by distributed damping. *Naval Engineers Journal* **74**(2), 341–348 (1962)
- Kruse, M., Wagner, S.: Visualization and laser Doppler measurements of the development of Lambda vortices in laminar-turbulent transition. *Meas. Sci. Technol.* **9**, 659–669 (1998)
- Kucala, A., Biringen, S.: Spatial simulation of channel flow instability and control. *J. Fluid Mech.* **738**, 105–123 (2014)
- Laadhari, F., Skandaji, L., Morel, R.: Turbulence reduction in a boundary layer by a local spanwise oscillating surface. *Physics of Fluids (1994-present)* **6**(10), 3218–3220 (1994)
- Landahl, M.T.: On the stability of a laminar incompressible boundary layer over a flexible surface. *J. Fluid Mech.* **13**(04), 609–632 (1962)
- Lee, S.J., Jang, Y.G.: Control of flow around a naca 0012 airfoil with a micro-riblet film. *Journal of fluids and structures* **20**(5), 659–672 (2005)
- Liepmann, H., Nosenchuck, D.M.: Active Control of Laminar Turbulent Transition. *J. Fluid Mech.* **118**, 201–204 (1982)

- Lipinski, D., Mohseni, K.: A ridge tracking algorithm and error estimate for efficient computation of Lagrangian Coherent Structures. *Chaos* **20**, 017,504–1 – 017,504–9 (2010)
- Lu, S.S., Willmarth, W.W.: A measurement of structure of the Reynolds stress in a turbulent boundary layer. *J. Fluid Mech.* **60**, 481 (1973)
- Lucey, A., Carpenter, P.: Boundary layer instability over compliant walls: Comparison between theory and experiment. *Physics of Fluids (1994-present)* **7**(10), 2355–2363 (1995)
- Luchik, T.S., Tiederman, W.G.: Timescale and structure of ejections and bursts in turbulent channel flows. *J. Fluid Mech.* **174**, 529 (1987)
- Maldovan, M.: Sound and heat revolutions in phononics. *Nature* **503**(7475), 209–217 (2013)
- Martinezsala, R., Sancho, J., Sanchez, J., Gómez, V., Llinares, J., Meseguer, F.: Sound-attenuation by sculpture. *nature* **378**(6554), 241–241 (1995)
- Marusic, I., Hutchins, N.: Experimental study of wall turbulence: implications for control. *Transition and turbulence control* pp. 207–246 (2005)
- May, C.L., Kleiser, L.: Numerical simulation of subharmonic transition in plane Poiseuille flow. *Bull. Amer. Phys. Soc.* **30**, 1748 (1985)
- Morkovin, M.V.: On the many faces of transition. *Viscous Drag Reduction* pp. 1–31 (1969)
- Morkovin, M.V.: On Roughness Induced Transition: Facts, Views, and Speculations. In: *Instability and Transition*, pp. 281–295. Springer (1990)
- Nishioka, M., Asai, M., Iida, S.: An experimental investigation of the secondary instability. In: *Laminar-Turbulent Transition*, pp. 37–46 (1980)
- Nishioka, M., Iida, S., Ichikawa, Y.: An experimental investigation of the stability of plane Poiseuille flow. *J. Fluid Mech.* **72**, 731–751 (1975)
- Onorato, M., Di Cicca, G.M., Iuso, G., Spazzini, P.G., Malvano, R.: Turbulent boundary layers and their control: Quantitative flow visualization results. *Lecture Notes Series Institute for Mathematical Sciences, National University of Singapore* **8**, 247–282 (2006)
- Pope, S.: *Turbulent Flows*. Cambridge University Press (2008)
- Prandtl, L.: Über flüssigkeitsbewegung bei sehr kleiner reibung. *Proc. Third Int. Math. Congr.* pp. 484–491 (1904)
- Ramazanov, M.P.: Development of finite-amplitude disturbances in Poiseuille flow. In: *Laminar-Turbulent Transition*, pp. 183–190 (1985)
- Reshotko, E.: Boundary-Layer Stability and Transition. *Ann. Rev. Fluid Mech.* **8**, 311–349 (1976)
- Reshotko, E.: Stability and transition - how much do we know? *Proc. 10th U.S. National Cong. of App. Mech.* pp. 421–434 (1987)
- Reynolds, W.C.: Orrsom: A Fortran-IV program for solution of the Orr–Sommerfeld equation. *Tech. rep.*, Stanford University (1969)

- Saiki, E.M., Biringen, S., Danabasoglu, G., Streett, C.L.: Spatial simulation of secondary instability in plane channel flow: comparison of K- and H-type disturbances. *J. Fluid Mech.* **253**, 485–507 (1993)
- Saric, W.S., Kozlov, V.V., Levchenko, V.Y.: Forced and unforced subharmonic resonance in boundary layer transition. AIAA paper **84(0007)** (1984)
- Saric, W.S., Reed, H.L., Kerschen, E.J.: Boundary-Layer Receptivity to Freestream Disturbances. *Ann. Rev. Fluid Mech.* **34**, 291–319 (2002)
- Saric, W.S., Reed, H.L., White, E.B.: Stability and Transition of Three-Dimensional Boundary Layers. *Ann. Rev. Fluid Mech.* **35**, 413–440 (2003)
- Schlichting, H.: *Boundary-layer theory* (1968)
- Schubauer, G.B., Skramstad, H.K.: Laminar-boundary-layer oscillations and transition on a flat plate (1948)
- Sen, P., Arora, D.: On the stability of laminar boundary-layer flow over a flat plate with a compliant surface. *J. Fluid Mech.* **197**, 201–240 (1988)
- Shadden, S.C., Dabiri, J.O., Marsden, J.E.: Lagrangian analysis of fluid transport in empirical vortex ring flows. *Phys. Fluids* **18**, 047105 (2006)
- Shadden, S.C., Lekien, F., Marsden, J.E.: Definition and properties of Lagrangian coherent structures from finite-time Lyapunov exponents in two-dimensional aperiodic flows. *Physica D* **212**, 271–304 (2005)
- Shadden, S.C., Lekien, F., Paduan, J.D., Chave, F., Marsden, J.E.: The correlation between surface drifters and coherent structures based on hf radar in Monterey Bay. *Deep-Sea Res. Part II* **56**, 161172 (2009)
- Singer, B.A.: Numerical simulation studies of laminar-turbulent transition in the plane channel. Stanford University (1987)
- Singer, B.A., Reed, H.L., Ferziger, J.H.: The effects of streamwise vortices on transition in the plane channel. *Physics of Fluids* **1**, 1960–1971 (1989)
- Spalart, P.R., Yang, K.S.: Numerical study of ribbon-induced transition in Blasius flow. *J. Fluid Mech.* **178**, 345–365 (1987)
- Viswanath, P.: Aircraft viscous drag reduction using riblets. *Progress in Aerospace Sciences* **38(6)**, 571–600 (2002)
- Voth, G., Haller, G., Gollub, J.: Experimental measurements of stretching fields in fluid mixing. *Phys. Rev. Lett.* **88**, 254,501 (2002)
- Waggy, S., Biringen, S., Sullivan, P.P.: Direct numerical simulation of top-down and bottom-up diffusion in the convective boundary layer. *J. Fluid Mech.* **724**, 581–606 (2013a)
- Waggy, S.B., Kucala, A., Biringen, S.: Parallel Implementation of a Navier–Stokes Solver: Turbulent Ekman Layer Direct Simulation. *International Journal of Computational Methods* (2013b)

- Walsh, M., Lindemann, A.: Optimization and application of riblets for turbulent drag reduction. American Institute of Aeronautics and Astronautics (1984)
- Watmuff, J., Pook, D., Sayadi, T., Wu, X.: Fundamental physical processes associated with bypass transition. In: Center for Turbulence Research, Proceedings of the Summer Program, p. 97 (2010)
- White, F.M.: Viscous Fluid Flow. McGraw Hill: New York (1974)
- Xu, C., Deng, B., Huang, W., Cui, G.: Coherent structures in wall turbulence and mechanism for drag reduction control. Science China Physics, Mechanics and Astronomy **56**(6), 1053–1061 (2013)
- Xu, S., Rempfer, D., Lumley, J.: Turbulence over a compliant surface: numerical simulation and analysis. J. Fluid Mech. **478**, 11–34 (2003)
- Zang, T.A., Krist, S.E.: Numerical Experiments on Stability and Transition in Plane Channel Flow. Theoret. Comput. Fluid Dynamics **1**, 41–64 (1989)